

**COLLECTED PAPERS on
Dressed Photon Science and Technology**

Vol. 31

September 2015 – December 2016

**Prof. Emeritus
Motoichi OHTSU**

MEMBERS

(From April 1, 2016)

Professor Emeritus

Motoichi OHTSU^(a-c) (Dr. Eng.)

Post-doctoral Researcher

Jun Hyoung KIM (Dr. Eng.)

Graduate Students (Master Course)

Teruo MURAKAMI

Secretaries

Chikako UEOKA

Mamiko ITABASHI

- a) Also, a project researcher *
- b) Also a director, Dressed Photon Research Origin**
- c) Also a director, NPO- Nanophotonics Engineering Organization ***

(*)

Institute of Engineering Innovation, School of Engineering, the University of Tokyo
(Room 219, Bldg. Eng. 9)

2-11-16 Yayoi, Bunkyo-ku, Tokyo 113-8656, Japan

Phone: +81-3-5841-6758

E-mail: ohtsu@nanophotonics.t.u-tokyo.ac.jp

URL:rodrep.jp /

東京大学大学院 工学系研究科 総合研究機構

〒113-8656 東京都文京区弥生 2-11-16 工学部 9 号館 219 号室

電話: 03-5841-6758

E-mail: ohtsu@nanophotonics.t.u-tokyo.ac.jp

URL:rodrep.jp /

(**)

Dressed Photon Research Origin

c/o Yokohama Technology Center, NICHIA Corp.

3-13-19 Moriya-cho, Kanagawa-ku, Yokohama-shi, Kanagawa 221-0022, Japan

E-mail: ohtsu@nanophotonics.t.u-tokyo.ac.jp

URL:rodrep.jp /

任意団体 ドレスト光子研究起点

〒221-0022 神奈川県横浜市神奈川区守屋町 3-13-19

日亜化学工業（株） 横浜技術センター 1階

E-mail: ohtsu@nanophotonics.t.u-tokyo.ac.jp

URL:rodrep.jp /

(***)

Nanophotonics Engineering Organization,

Specified Nonprofit Corporation

1-20-10 Sekiguchi, Bunkyo-ku, Tokyo 112-0014, Japan

Phone: +81-3-3267-6790. Fax: +81-3-5261-9788

特定非営利法人 ナノフォトンクス工学推進機構

〒112-0014 東京都文京区関口 1-20-10

電話: 03-3267-6790, ファックス: 03-5261-9788

LIST OF PAPERS

[(pp. XX-XX); pages in this issue of the COLLECTED PAPERS]

[I] ORIGINAL PAPERS

- [1] J. Lee, F. Peper, S.D. Cotofana, M. Naruse, M. Ohtsu, T. Kawazoe, Y. Takahashi, T. Simokawa, L.B. Kish, and T. Kubota, "Brownian Circuits: Designs," Int. Journ. of Unconventional Computing, Vol.12, No.5-6, 2016, pp.341-362.
(pp. 1-22)
- [2] T. Ishii, T. Kawazoe, Y. Hashimoto, H. Terada, I. Muneta, M. Ohtsu, M. Tanaka, and S. Ohya, "Electric structure near the Fermi level in the ferromagnetic semiconductor GaMnAs studied by ultrafast time-resolved light-induced reflectivity measurements," Phys. Rev. B **93**, June 2016, 241303(R).
(pp. 23-26)
- [3] H. Tanaka, T. Kawazoe, M. Ohtsu, K. Akahane, and N.Yamamoto, "Evaluation of optical amplification properties using dressed photons in a silicon waveguide," Applied Physics A, Vol.121, Issue 4, December 2015, pp.1377-1381.
[Invited Paper] (printed version of [1] in C.P.Vol.30)
(pp. 27-31)
- [4] N. Tate, M. Naruse, T. Matsumoto, M. Hoga, Y. Ohyagi, S. Nishio, W. Nomura, and M. Ohtsu, "Non-scanning optical near-field microscopy for nanophotonic security," Applied Physics A, Vol.121, Issue 4, December 2015, pp.1383-1387.
[Invited Paper] (printed version of [3] in C.P.Vol.30)
(pp. 33-37)
- [5] M. Yamaguchi, T. Kawazoe, T. Yatsui, and M. Ohtsu, "Spectral properties of a lateral p-n homojunction-structured visible silicon light-emitting diode fabricated by dressed-photon—phonon-assisted annealing," Applied Physics A, Vol.121, Issue 4, December 2015, pp.1389-1394.
[Invited Paper]
(pp. 39-44)
- [6] J.H. Kim, T. Kawazoe, and M. Ohtsu, "Optimization of dressed-photon—phonon-assisted annealing for fabricating GaP light-emitting diodes," Applied Physics A,

Vol.121, Issue 4, December 2015, pp.1395-1401.

[Invited Paper]

(pp. 45-51)

- [7] W. Nomura, T. Yatsui, T. Kawazoe, N. Tate, and M. Ohtsu, “High-speed flattening of crystalized glass substrates by dressed-photon—phonon etching,” Applied Physics A, Vol.121, Issue 4, December 2015, pp.1403-1407.

[Invited Paper]

(pp. 53-57)

- [8] T. Kawazoe, K. Nishioka, and M. Ohtsu, “Polarization control of an infrared silicon light-emitting diode by dressed photons and analyses of the spatial distribution of doped boron atoms,” Applied Physics A, Vol.121, Issue 4, December 2015, pp.1409-1415.

[Invited Paper] (printed version of [4] in C.P.Vol.30)

(pp. 59-65)

[II] PRESENTATIONS IN INTERNATIONAL CONFERENCES

- [1] M. Ohtsu, “Dressed Photon ---Concepts of off-shell photon and applications to light-matter fusion technology---,” Abstracts of the Conf. on Mathematical quantum field theory and related topics, June 6-8, 2016, Fukuoka, Japan, paper number 4.

[Invited Presentation]

(pp. 67-68)

- [2] N. Tate, T. Kawazoe, S. Nakashima, W. Nomura, and M. Ohtsu, “Speckle reduction by using transmissive ZnO device based on dressed-photon-assisted optical modulation,” Abstracts of the 22nd International Display Workshops, December 9-11, 2015, Otsu, Japan, PRJ3-1.

[Invited Presentation]

(pp. 69-72)

- [3] T. Kawazoe, N. Tate, and M. Ohtsu, “SiC magneto-optical current-transformer applicable to a polarization rotator using dressed photons,” Abstracts of the 22nd International Display Workshops, December 9-11, 2015, Otsu, Japan, PRJ3-5L.

(pp. 73-74)

- [4] N. Tate, T. Kawazoe, S. Nakashima, W. Nomura, and M. Ohtsu, “Recent progress in dressed-photon-assisted electro-optical modulation,” Abstract of the 5th Korea-Japan Workshop on Digital Holography and Information Photonics, September 17-19, 2015, Gangneung, Korea, p.72.

[Invited Presentation]

(p. 75)

[III] REVIEW PAPERS

- [1] M. Ohtsu, “Dressed photons and their applications,” A Monthly Publication of the Japan Soc. Appl. Phys., Vol.85, No.12, December 2016, pp.1023-1027 (in Japanese).

【大津元一、「ドレスト光子とその応用」、応用物理、第85巻、第12号、2016年12月、pp. 1023-1027】

(pp. 77-81)

- [2] M. Ohtsu, “Introduction: What are dressed photons and their applications?”, the 1st issue in the series of “Revolutional optical technology by dressed photons”, Optronics, Vol.412, No.4, April 2016, pp.135-138 (in Japanese).

【大津元一、「総論：ドレスト光子とは何か？その応用展開は？」、ドレスト光子が切り拓く革新的光技術 第1回、オプトロニクス、第412巻、第4号、2016年4月、pp. 135-138】

(pp. 83-86)

- [3] M. Ohtsu, “International Center for Nano Electron and Photon Technology: At the Forefront for Global R&D and International Collaboration,” AAPPS Bulletin, Vol. 25, No. 5, October 2015, pp.36-39.

(pp. 87-90)

[IV] PUBLISHED BOOKS

- [1] T. Tadokoro, “Experiment of Light,” (Supervised by M. Ohtsu), Asakura Publishing Co, Tokyo, October 2016 (128 pages) (in Japanese).

【大津元一（監修）、田所利康（著）「イラストレイテッド 光の実験」、朝倉書店、東京、2016年10月、（128ページ）】

(pp. 91-92)

- [2] M. Ohtsu, “Silicon Light-Emitting Diodes and Lasers: Photon Breeding Devices using Dressed Photons”, Springer, Heidelberg, August 2016 (192pages).

(pp. 93-96)

[V] AWARDS

[1] M. Ohtsu, the Okawa Publication Prize, “Dressed Photons (published by Asakura Publishing Co., in Japanese),” the Okawa Foundation, March 2016.

【大津元一、大川出版賞、「ドレスト光子（朝倉書店）」、(財)大川情報基金（大川財団）、2016年3月】

[2] M. Ikegawa, the Excellent Presentation Award for Young Scientists, “Evaluation of the sensitivity of Si blue-ultraviolet photodetector with optical amplification by dressed photons,” The 63th Annual Meeting of Japan Society of Applied Physics, March 2016. (in Japanese).

【池川昌貴、第63回応用物理学会春季学術講演会「講演奨励賞」
受賞対象題目「ドレスト光子を用いた光増幅型のシリコン青・紫外光検出器の感度評価」（2016年3月）講演番号19a-S622-9.】

[VI] APPENDIX

Publications and Presentations by NPO Nanophotonics Eng. Org.

[1] T. Kawazoe, K. Hashimoto, and S. Sugiura, "High-power current-injection type Silicon laser using nanophotonics," Abstract of the EMN Nanocrystals Meeting, October 17-21, 2016, Xi'an, China, pp.9-11 (paper number 03).

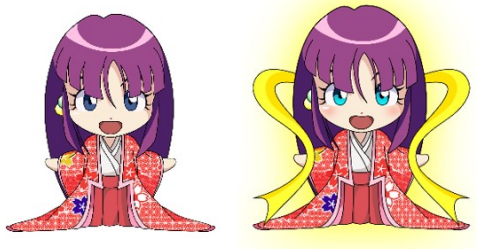
(pp. 97-99)

[2] T. Kawazoe, "Light emitting devices by dressed photons," the 3rd issue in the series of "Revolutional optical technology by dressed photons", Optronics, Vol.412, No.6, June 2016, pp.118-122 (in Japanese).

【川添忠、「ドレスト光子発光デバイス」、ドレスト光子が切り拓く革新的光技術 第3回、オプトロニクス、第412巻、第4号、2016年6月、pp. 118-122】

(pp. 101-106)

[I] ORIGINAL PAPERS



Brownian Circuits: Designs

JIA LEE¹, FERDINAND PEPPER^{2,3,4,5,*}, SORIN D. COTOFANA⁶,
MAKOTO NARUSE², MOTOICHI OHTSU⁷, TADASHI KAWAZOE⁸,
YASUO TAKAHASHI⁹, TETSUYA SHIMOKAWA^{2,3,5}, LASZLO B. KISH¹⁰
AND TOHRU KUBOTA²

¹*College of Computer Science, ChongChing University, China*

²*National Institute of Information and Communications Technology, Japan*

³*Osaka University, Japan*

⁴*The University of Hyogo, Japan*

⁵*Kobe University, Japan*

⁶*Delft University of Technology, the Netherlands*

⁷*The University of Tokyo, Japan*

⁸*Nanophotonics Engineering Organization, Japan*

⁹*Graduate School of Information Science and Technology,
Hokkaido University, Japan*

¹⁰*Department of Electrical and Computer Engineering,
Texas A&M University, College Station, USA.*

Received: May 2, 2016. Accepted: May 26, 2016.

The ongoing miniaturization of electronic circuits will eventually lead to signals consisting of only a few particles or molecules, but fluctuations will be a major interference in the operation of such circuits. Brownian circuits have been shown to exploit fluctuations by finding computational paths in circuits through a random search mechanism. This paper discusses Brownian circuits with decreased complexity, and shows designs of circuits with functionalities like counting, testing of conditional statements, memory, and arbitration of shared resources. We also discuss the potential of Brownian circuits for implementations by Single Electron Tunneling technology.

Keywords: Fluctuation-driven computation, Brownian motion, circuit designs, nanocomputing

1 INTRODUCTION

Brownian circuits employ fluctuating tokens as signals to search randomly for computational paths in the state space defined by the circuit topology.

* Contact author: E-mail: pepper@nict.go.jp

Fluctuations are not just a nuisance factor in such circuits, rather they are actively exploited in assisting circuit operations. Brownian circuits provide an alternative to more conventional strategies to deal with noise, which usually amounts to suppressing noise or employing error correction. While such methods work when signal levels are well above noise by a large factor, they fall short in a regime near the thermal limit [15], where the energy to operate a switch barely exceeds that of thermal noise. This issue has become more serious with the increased integration densities of microelectronics, which will eventually lead to circuits employing signals that consist of only a small number of particles. Fluctuations in such circuits will be difficult to avoid [18].

One of the first proposals to use Brownian motion of signals in computation originates with Bennett [4]. It takes the form of a miniature mechanical Turing machine, in which signals move around randomly, driven by thermal noise, and searching their way through the machine's circuit topology. Later proposals have employed fluctuations with the eye of making a trade-off between energy use and reliability [8, 19], but these approaches tend to require extensive error correction, and may thus fall in the realm of more-or-less traditional methods. Noise and fluctuations have also been used in the simulated annealing process of a Boltzmann machine [26]. Based on Single Electron Tunneling devices, this architecture has been shown by computer simulations to be able to exploit signal fluctuations to search in an energy landscape. This proposal revolves around a neural network that conducts optimization, but it is not suitable for arithmetic computation.

In biological systems, noise and fluctuations play an important role in facilitating transitions between energy states that are separated by a high energy barrier. Whereas designers of engineered systems usually aim to achieve high S/N ratios, biological systems differ in that they have evolved to take advantage of noise and fluctuations, allowing high energy efficiencies, like in rotary protein motors, which work at efficiencies close to 100 percent [7]. Fluctuations are also used in a biological system to exert effective control on molecular scales through a trial-and-error mechanism that employs stochastic search to make the system converge to a desirable state. This phenomenon is called *Brownian search*.

Brownian circuits use a similar mechanism to conduct their operations in a controlled way. This is formalized in [23] through the definition of a circuit element—the *T-element*—that has been proven to be universal for a class of circuits called *Token-Pass circuits*, under the necessary and sufficient condition that tokens undergo fluctuations. Key to the power of token fluctuations is their ability to backtrack out of deadlocks, which are a common problem in token-based circuits [23]. Token-Pass circuits, along with the T-element, form a suitable framework to formally prove the capability of fluctuations, but they have a somewhat rigid structure, being basically a set of lines that can interact

with each other at certain locations in very restricted ways. This poses the question whether more efficient—in terms of hardware and time resources—constructions are possible if more flexibility is allowed in the definition of circuits.

The pay-off of such simplified constructions lies in the potential for efficient designs in physical implementations. The omnipresence of fluctuations at nanometer scales, combined with the trend in microelectronics of signals consisting of less and less particles, underlines the importance of the formulation of such abstract circuit models.

This paper describes circuits that are based on elements that are less complex than the T-element, yet can be used as primitives of a universal class of Brownian circuits. Called *Hub*, *Conservative Join (CJoin)*, and *Ratchet* (see Section 2), these elements have three, four, and two input and output lines, respectively, which is less than the six lines of the T-element [23]. Token fluctuations are fundamental to operations of circuits based on the Hub, the CJoin, and the Ratchet, but compared to the Brownian circuits in [23], circuits tend to become more straightforward in their designs. We introduce designs of some standard circuits, such as a 1-bit memory cell and a Half-Adder (Section 3), and an arbitration operator for shared resources (Section 4), and combine these into more complex functionalities (Section 5). We also discuss six conditions that are important for the realization of Brownian circuits in terms of physical implementations (Section 6). This is followed by a brief review of Single Electron Tunneling technology designs based on Brownian circuits (Section 7). The discreteness of single electrons, as well as the stochastic nature of electron tunneling, both fit well in the framework of Brownian circuits. Other technologies based on different mechanisms [16], however, may also be suitable for physical implementations, provided they employ signals that have a discrete character and the tendency to undergo fluctuations. This paper finishes with conclusions and a discussion in Section 8.

2 BROWNIAN CIRCUITS

A Brownian circuit is a token-based circuit, in which tokens are allowed to fluctuate forwards and backwards on lines and across operators. Notwithstanding their ability to fluctuate, tokens are bound by the transition rules governing circuits. An operator that requires a particular combination of inputs will not produce outputs unless that combination is available on the operator's input lines at a certain time instant. For every other combination the tokens will remain fluctuating on the input lines, where they may again serve as input to the operator at some future time. The use of fluctuations has an important merit: it allows Brownian circuits to backtrack out of states

in which no forward computational path exists [23]. *Deadlocks* are the usual term for such situations, and they are likely to arise in conventional (non-Brownian) token-based circuits when a circuit element—or, *module* in our terminology—requires at least two tokens as input. Absent the full number of input tokens, the input to a module will stay pending, waiting for the remaining input tokens to arrive, and when that does not happen, a deadlock results. The usual way out of a deadlock is to reroute pending tokens to alternative locations in the circuit, where they can be processed without deadlocks. Given that tokens can only move forward in conventional token-based circuits, however, this requires additional pathways and additional control mechanisms, which increases the complexities of modules and inter-module connection patterns. Brownian circuits do not require these additional resources, since they use fluctuations to make tokens backtrack their way out of deadlocks, and in the process reach other modules that can accept them.

The Brownian circuits in [23] are very useful for the formal analysis of fluctuations in a computational framework, but they have some overhead in terms of interconnection lines, making them less suitable for efficient implementations. This motivates the definition of a class of circuits facing less restrictions, the so-called *Conservative Delay-Insensitive (CDI) circuits* [22]. Promising for their physical plausibility, these circuits are robust to delays of tokens, and they conserve tokens in operations, i.e., the number of input tokens to a module equals the number of output tokens.

A universal set of primitive modules for CDI circuits consists of the *Merge* and the 2×2 -*CJoin*. Figure 1 shows these modules, together with their functionalities, expressed in terms of Petri nets (see also [23]). The universality of this set of primitive modules can be shown by constructing a so-called $n \times m$ -*CJoin* from it according to the design in [22]. The $n \times m$ -*CJoin* is a generalization of a 2×2 -*CJoin* and it is possible to construct a Finite State Machine (FSM) from it with n states and m inputs (e.g. see [11, 21]). Since any logic circuit can be expressed in terms of an FSM, the universality of the set consisting of the Merge and the 2×2 -*CJoin* follows (see also [6]).

When CDI circuits have fluctuating tokens, they are Brownian. They can be constructed from a set of three primitive modules. The first module is the *Hub*, which has three lines that are bidirectional (Figure 2). There is at most one token at a time on any of the Hub's lines, and this token can move to any of the lines due to its fluctuations.

The second module is the *Conservative Join (CJoin)*, which has two input lines and two output lines (Figure 3). The two tokens on its input lines (one token on each line) pass through the CJoin in a pairwise manner, so the CJoin in fact behaves like a synchronizer. Tokens may fluctuate on the input lines, and when processed by the CJoin, they move to the output lines where they may also fluctuate. The operation of the CJoin may also be reversed, and the

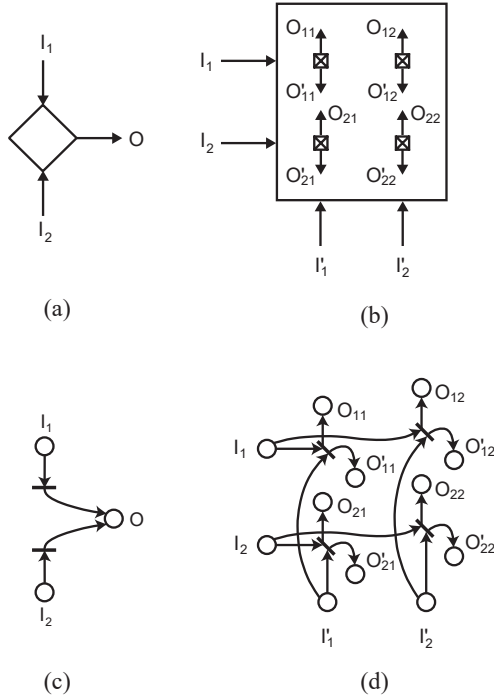


FIGURE 1
 Primitive elements for Conservative Delay-Insensitive (CDI) circuits, and the corresponding Petri nets. (a) Merge merges two streams of input tokens I_1 and I_2 into one output stream O . (b) 2×2 -CJoin joins two input tokens resulting in two output tokens as follows. Upon receiving one token from line I_i and one token from line I'_j ($i, j \in \{1, 2\}$), the module outputs one token to each of the lines O_{ij} and O'_{ij} . If there is only one token input to the module, it remains pending until a second token is input to the module. (c) Petri net of the Merge, and (d) of the 2×2 -CJoin.

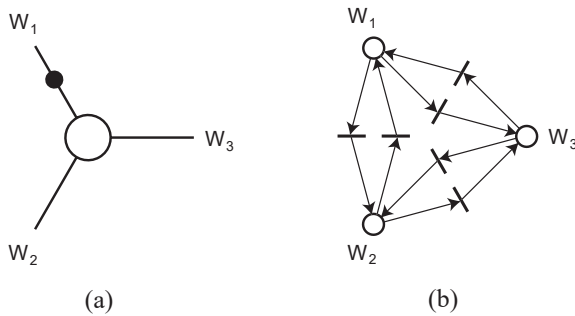


FIGURE 2
 (a) The Hub, with a token on one of its lines (W_1), denoted by a black blob. All lines are bidirectional and are indicated without arrow heads. The token can be on any of the three lines W_1 , W_2 , and W_3 , and it can fluctuate between the lines in any order. (b) Petri net of the Hub.

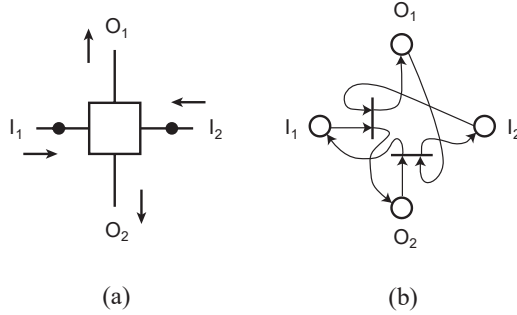


FIGURE 3

(a) The CJoin, with one token on each of its two input lines I_1 and I_2 . A transition moves the tokens from the input lines to the two output lines O_1 and O_2 , or in the reverse direction if both tokens are on the output lines. If there is a token on only one input line (I_1 or I_2), this token remains pending (and fluctuating) until a token arrives on the other input line. All lines are bidirectional and lack arrow heads, but since there is a bias from input to output, there are small arrows to indicate the preferred direction of token flow. (b) Petri net of the CJoin.

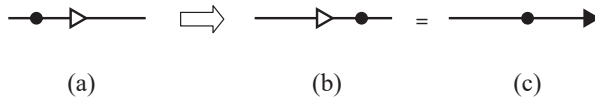


FIGURE 4

Ratchet and its possible transition. (a) The token on the line may fluctuate before the Ratchet as well as after the Ratchet, but (b) once it is at the right side of the Ratchet it cannot return. The Ratchet thus imposes a direction on an (originally bidirectional) line. (c) The resulting unidirectional line is denoted by an arrow.

forward / backward movement of the two tokens through it may be repeated an unlimited number of times. Due to this bidirectionality, there is strictly spoken no difference between input and output lines of the CJoin, though we still use the terminology of input and output, since the direction of the process is eventually biased forward. We call this the *preferred* direction of the CJoin or of the associated lines.

The third module is the *Ratchet*, which allows a token to freely pass through in one direction, but blocks it in the opposite direction (Figure 4). Thus, a bidirectional line with a Ratchet on it effectively becomes unidirectional. Ratchets can be used to limit the searching behavior of a circuit at selected points, as a result of which the circuit is sped up. However, the placement of Ratchets should be carefully considered to avoid the creation of deadlocks at locations where Brownian search is required.

To show that the set consisting of the Hub, CJoin, and Ratchet is universal for the class of CDI circuits, we construct a Merge and a 2×2 -CJoin from

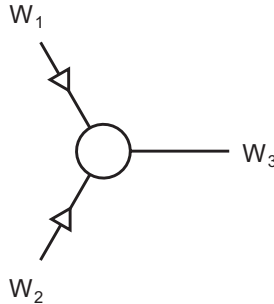


FIGURE 5

The Merge constructed from a Hub and two Ratchets. The Ratchets are used to guarantee that any token input to the Merge will always be output to line W_3 , and never to either of the input lines W_1 and W_2 .

them. Since the Merge and the 2×2 -CJoin have only unidirectional input and output lines, Ratchets are used to mimic this characteristic. The Merge is constructed from a Hub and two Ratchets, whereby two of the Hub's bidirectional lines are equipped with Ratchets to act as input lines for the Merge, and the remaining bidirectional line of the Hub is used for output of the Merge (Figure 5). The construction of the 2×2 -CJoin requires four Hubs, four CJoins, and twelve Ratchets. The more general construction of the $n \times m$ -CJoin is given in Figure 6. Brownian search in this construction takes place at the trees forming the input lines of the individual CJoin modules.

Universality of the set consisting of the Hub, CJoin, and Ratchet can also be shown in a different way, i.e., by constructing a so-called Conservative Tria (CTria) from these modules [12], but we employ the construction based on the $n \times m$ -CJoin, because it results in more straightforward and efficient designs.

3 CIRCUIT DESIGNS

The universality of the Hub, CJoin, and Ratchet set opens the way for constructions of circuits like a Half-Adder and a 1-bit memory. The basic idea behind these constructions is to use the CJoins in an $n \times m$ -CJoin as minterms in a canonical form of a Boolean expression, and to use the Hubs for summing the minterms into the desired results, following similar ideas as in [23]. A Half-Adder, for example, is constructed from one 2×2 -CJoin and four Hubs (Figure 7). The inputs of the Half-Adder—represented by the 0-line and the 1-line at the top and a similar pair of lines at the right according to a dual-rail encoding scheme ([13], Chapter 7)—are fed to the four CJoins,

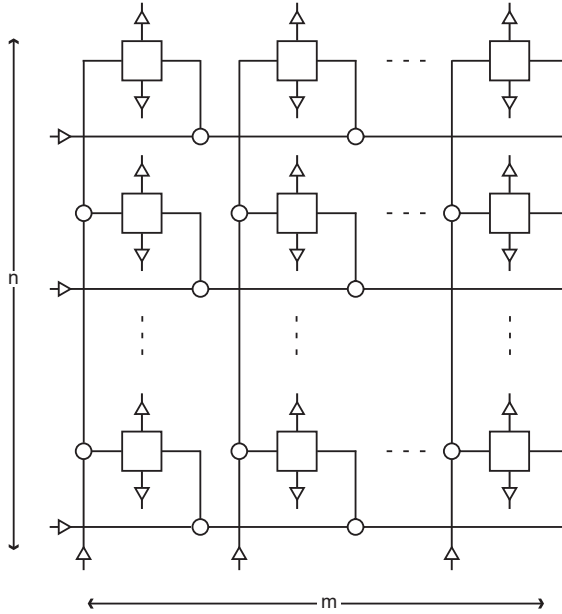


FIGURE 6

The $n \times m$ -CJoin constructed as an array of CJoin modules with n rows and m columns. Each row contains—apart from CJoin modules—a total of $m - 1$ Hubs that allow a token to conduct a Brownian search in the row of m CJoins. Similarly, each column contains $n - 1$ Hubs for searching in the column of n CJoins. This gives a total of $n(m - 1) + (n - 1)m = 2nm - n - m$ Hubs. When one token is received from the input line at row i and one token from the input line at column j , the tokens find their way through Brownian search to the CJoin in row i and column j . After accepting these tokens, this CJoin produces one token at each of its two corresponding output lines. Ratchets are placed at locations where Brownian search is not necessary, which in this case is at the output sides of the CJoins. A total of $2mn + m + n$ Ratchets is used.

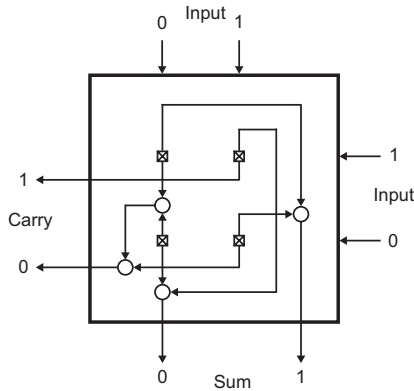


FIGURE 7

Half-Adder constructed from a 2×2 -CJoin and four Hubs.

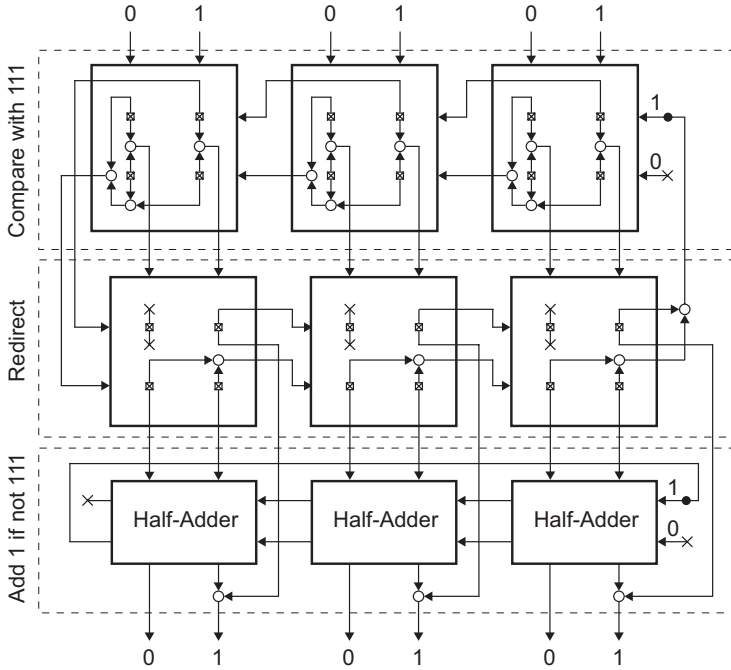


FIGURE 8

3-bit Conditional Counter. The 3-bit input received by the Counter is compared with the bit-string ‘111’ in the top stage. Depending on the outcome of the comparison, the second stage either redirects the input to the output (when the input equals ‘111’), or to the third stage to increase it by one before being output. Due to the comparator in the first stage, there will never be overflow in the third stage, so the carry bit 1 in the most-significant Half-Adder is not connected to other modules.

and the resulting four min-terms are combined through the Hubs to produce the Half-Adder’s sum at the bottom and the carry at the left.

Figure 8 combines three Half-Adders into a 3-bit Conditional Counter that adds 1 to its input in an operation, provided the input is less than the maximal value ‘111’. The first stage of this counter compares the input with the bit string ‘111’ and if the input equals this string, it is redirected toward the output; otherwise it is increased by one by the Half-Adders in the bottom stage before the results are output.

Another useful circuit is a 1-bit memory, which requires a 2×3 -CJoin, as shown in Figure 9(a). The construction principle is similar to that of the Half-Adder, with minterms produced by the six CJoins in the 2×3 -CJoin being summed by six Hubs. This construction involves feedback connections to store the memory state, and Ratchets are used to retain the state. A 1-bit memory can also be constructed from two 2×2 -CJoins, like in Figure 9(b).

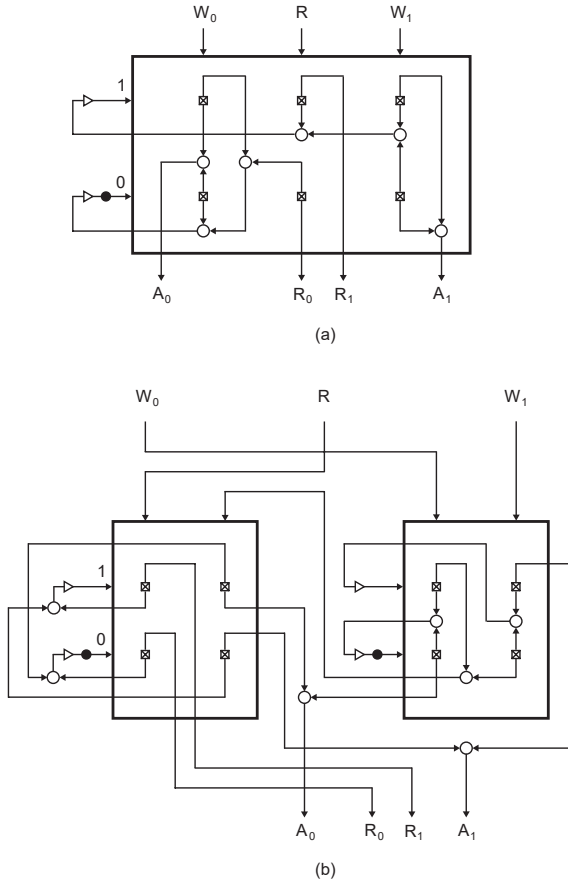


FIGURE 9

(a) One-bit memory constructed from a 2×3 -CJoin and six Hubs. The state of the memory is stored by one token residing on one of the input lines at the left, whereby a token on the lower line (like in the figure) denotes the state 0 and a token on the upper line denotes the state 1. The value 0 resp. 1 is written into the memory by putting a token on the line W_0 resp. W_1 . After the required value is written, a token is output to the corresponding acknowledge line A_0 or A_1 . Reading from the memory is done by inputting a token to line R , which results in a token output to line R_0 or line R_1 , depending on the memory's state. (b) One-bit memory constructed from two 2×2 -CJoins and seven Hubs. For technical reasons, the memory's state is stored by two tokens in parallel.

4 ARBITRATION

When there are parallel processes competing for a shared resource, the assignment of that resource is accomplished through *arbitration*. The circuits in the previous section all work fine in the absence of arbitration, since

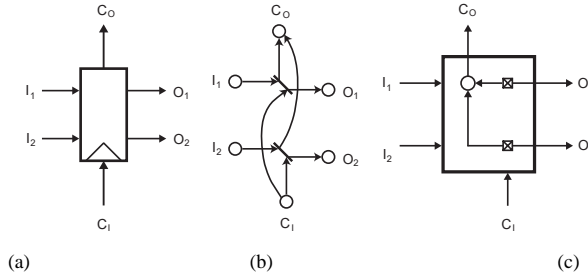


FIGURE 10

(a) CSequencer facilitates arbitration of shared resources between parallel processes. An input token on line I_1 (resp. I_2) together with an input token on line C_I but without an input token on line I_2 (resp. I_1) results in one output token on line O_1 (resp. O_2) and one on line C_O . If there are input tokens on both I_1 and I_2 at the same time as well as an input token on C_I , then only one of the tokens on I_1 and I_2 (possibly chosen arbitrarily) is taken together with the token on C_I , resulting in an output token on the corresponding O_1 or O_2 line and on line C_O . The remaining input token may be processed at a later time, when a new token is available on line C_I . (b) Petri net of the CSequencer. (c) CSequencer constructed from a 2×1 -CJoin.

no resource sharing is needed. A module capable of arbitration behavior is the *Conservative Sequencer (CSequencer)* in Figure 10(a), with functionality as defined by the Petri-net in Figure 10(b). This module is basically a 2×1 -CJoin (Figure 10(c)) in which simultaneous input tokens to the two lines I_1 and I_2 are allowed, one of which passes to the corresponding output line either O_1 or O_2 respectively, if a token is input to line C_I . This behavior is a direct consequence of the searching process in the underlying Brownian circuit. The fluctuations of the token input to C_I drive a search inside the module to match it with a second token input from either line I_1 or line I_2 . As long as the token from C_I fails to find a token to match with, no operations take place in the 2×1 -CJoin, and the C_I token continues its search. This circuit is capable of arbitration as a result of the tokens being subject to fluctuations. Absent those, the circuit may end up in a deadlock.

The CSequencer comes in various formats. The version that arbitrates n processes is called the n -CSequencer. When $n = 2$, like above, the prefix is left out. The n -CSequencer can be implemented by an $n \times 1$ -CJoin.

5 ARBITRATION-BASED CIRCUITS

When the Conditional Counter in Figure 8 is extended with memories to store the counted value, we obtain a circuit like in Figure 11. This circuit, which we call *Counting Memory*, includes functionality to count up or down by one, or read out the memory value. An attempt to conduct these operations at the

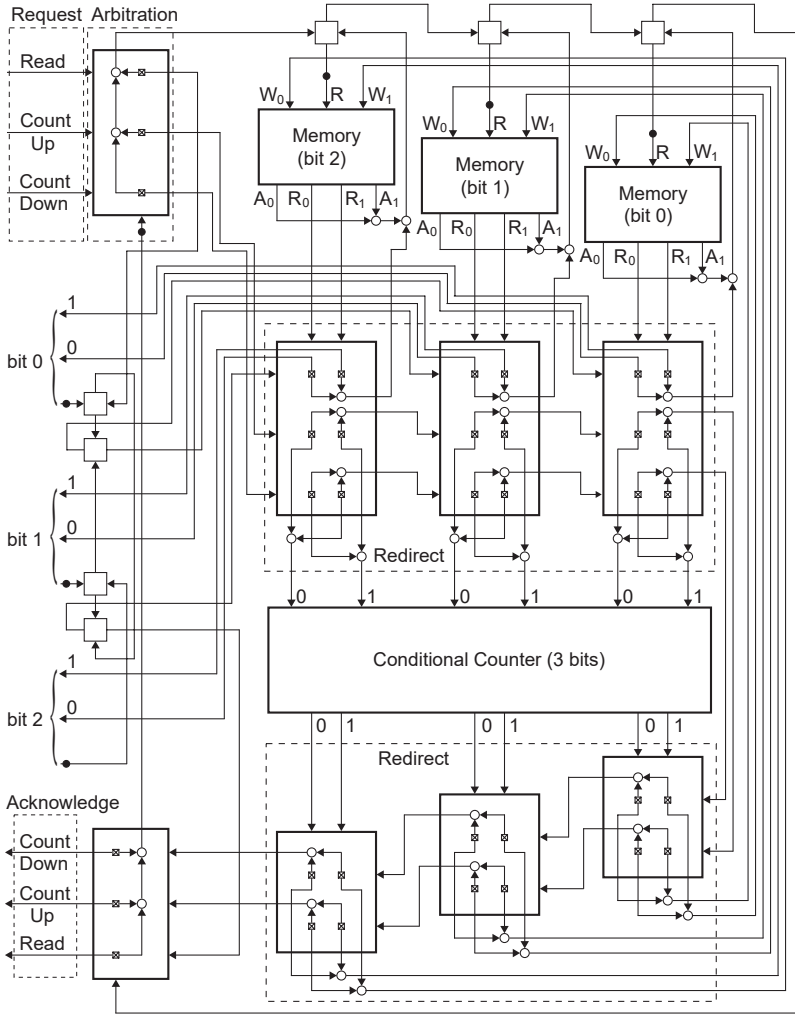


FIGURE 11

Counting Memory storing three bits, the value of which can be read out, or, alternatively, be increased by one up to a maximum of '111' or decreased by one down to a minimum of '000'. A token input to the Read line at the top left results in the memory's value being output to the pairs of 0- or 1-lines of bits 0, 1, and 2 at the center left. This operation requires one token to be input for each bit to ensure that the number of tokens is conserved (lowest line of each bit). A token input to the Count-Up line resp. Count-Down line results in the Counting Memory's value being increased resp. decreased by one. All three operations generate an acknowledge-token at the lower left.

same time in a non-arbitrating circuit would give unpredictable results, but this is prevented by arbitrating simultaneous calls to the circuit through a 3-CSequencer (top left), which is implemented as a 3×1 -CJoin.

The Counting Memory output is given in dual-rail encoded form through three pairs of 0- and 1-lines (bits 0, 1, and 2 at the center left of Figure 11). As a result of a reading operation, tokens are output to these lines so that they reflect the values stored in the 1-bit memories at the top of the figure. Since the circuit conserves tokens, any number of tokens it outputs should be compensated by input of the same number of tokens. This is the reason why each of the output bits has a single token accompanying it on the line below the bit's two output lines. These input tokens are absorbed by the circuit when a Read signal passes the arbitrator at the top left.

Increasing or decreasing the number stored in the memory is accomplished through the 3-bit Conditional Counter just below the center. While an increase in value is straightforward, a decrease is done by first redirecting the number's bits via the three modules directly above the Conditional Counter. These modules include functionality to convert the number represented by the bits into its negative equivalent in two's complement representation. This is followed by an operation of the Conditional Counter to increase the number by one, and then convert the result back by the three Redirect modules at the bottom. No output signals are generated by a counting operation, except for a token at an output line at the bottom left in the figure to acknowledge the end of the operation. Such an acknowledge signal is also generated at the end of a reading operation.

Figure 12 shows a circuit that calls the Counting Memory from three parallel threads. Though the Counting Memory in itself is able to arbitrate Read, Count-Up, and Count-Down calls, the three threads may coincidentally call one and the same operation at the same time, which may give undesirable results. Thread 1 and thread 3, for example, both have calls to read out the value of the Counting Memory, but only one such call can be handled at a time, requiring an additional level of arbitration. The modules at the bottom center of Figure 12 provide this arbitration functionality. For each type of operation—Read, Count-Up, or Count-Down—it allows only one call to be made at a time. Any other calls are delayed until the Counting Memory is available again.

The Read operation is the most complex since it requires input and output tokens of the bits to be routed from and to the thread that made the Read call. The part of the circuit in Figure 12 located just left of the Counting Memory is responsible for this. It collects a Read operation's tokens from threads, and decides from which thread it redirects tokens to the Counting Memory in accordance with the decision of the arbitration part at the bottom of the

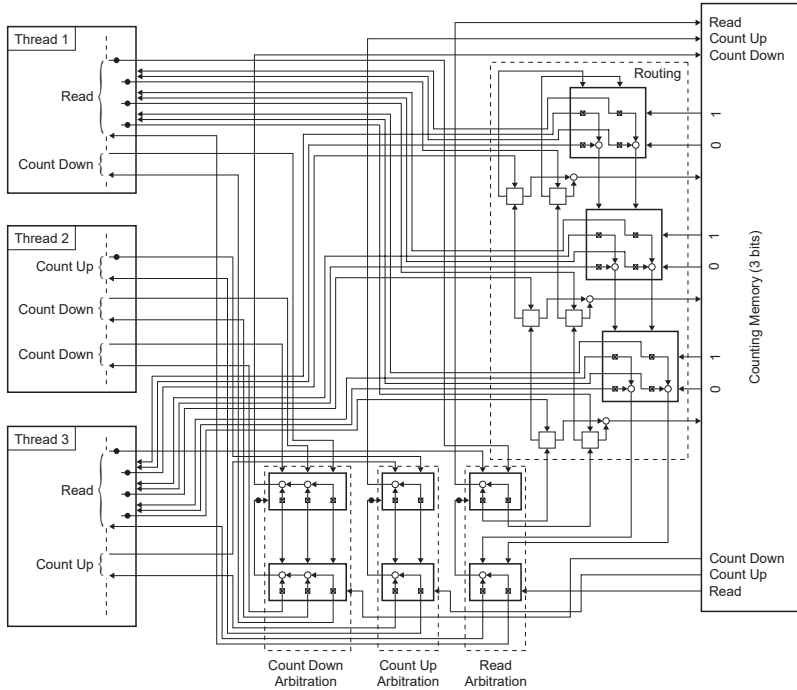


FIGURE 12

Arbitration of calls by three parallel threads to a 3-bit Counting Memory. Each thread is executed from top to bottom and when a call to the Counting Memory is made, the corresponding tokens are submitted to the Counting Memory, but not before they pass arbitration circuitry at the bottom center. The part of the circuitry located just left of the Counting Memory is an extension of this arbitration circuitry, and it takes care for routing bits associated with the Read operation between the Counting Memory and the thread requesting the operation.

figure. Similarly, the output bits of the Read operation are routed back to the corresponding thread that made the call.

The lines in Figures 11 and 12 are all unidirectional, which allows Ratchets to be placed on them. The presence of Ratchets on these lines causes no problem, since no Brownian search needs to take place on them. All Brownian searching behavior is restricted to a local level within $n \times m$ -CJoin modules. Ratchets placed outside these modules do not affect the Brownian search process inside modules. Consequently, the only penalties in time complexity likely to be incurred are those due to Brownian searching within $n \times m$ -CJoin modules, but since the dimensions of these modules are small in our case, this overhead is limited.

Sections 3 to 5 have presented designs of elementary circuits, like counters and memories, as well as examples combining these circuits into more

complex circuits. In principle, circuits for every computable function can be constructed, since the basis set, consisting of the Hub, the CJoin, and the Ratchet, is universal for the class of CDI circuits. Arbitration in circuits is facilitated by Brownian search in the underlying Brownian circuits.

6 REALIZATIONS OF BROWNIAN CIRCUITS

For Brownian circuits to be realized by a technology or a model certain conditions must be met. This section discusses such conditions for circuits based on the Hub, CJoin, and Ratchet.

Token-Based Condition. Signals are represented as tokens: it is impossible to divide a signal into more signals, or to fuse multiple signals into one signal when on a line, i.e. outside a module. In practice this condition implies that signals behave like particles.

Line-Search Condition. A signal is able to explore the state space of a line by Brownian search based on fluctuations.

Hub-Search Condition. A signal is able to explore the state space of a Hub by Brownian search based on fluctuations. This condition is similar to the Line-Search condition, but then extended to three lines coming together in the Hub.

CJoin-Pair Condition. Two signals input to the CJoin (at two different lines), pass through the CJoin in a pairwise manner. If the two signals go back through the CJoin they do so in a pairwise manner too. This condition does not require signals to pass through the CJoin at the same time: it just means that when one signal passes through the CJoin, the other will also pass. Figure 13 shows a sequence of events in which signals pass pairwise, but not simultaneously.

In this case the CJoin has six states that are assumed in certain orders to ensure that the correct sequences from input to output are followed. After both signals have passed, the CJoin's state reverts to the initial state S_0 , i.e., to the state before the signals were input. If the CJoin passes its two signals simultaneously, only one state is required.

Modularity Condition. The functionalities of the circuit elements (Hub, CJoin, or Ratchet) do not change when they are connected to each other. In other words, there should be no interference on the behavior inside a module from processes at the outside.

Ratchet Condition. Ratchets are to be placed at positions where no Brownian search is required. Feasible positions to place Ratchets are at output sides

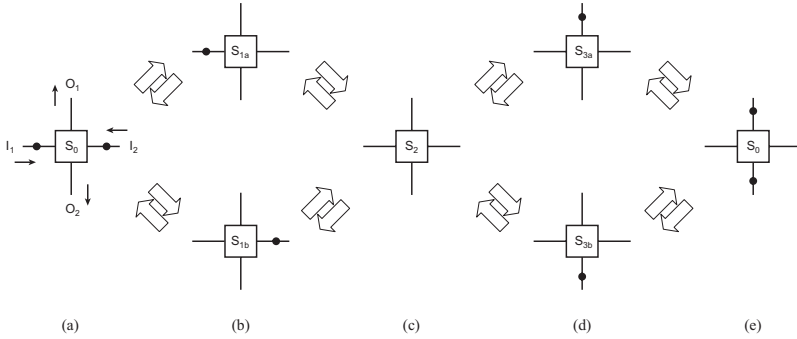


FIGURE 13

Sequences of states assumed by a CJoin when two signals are passed through it pairwise but not necessarily simultaneously. Transitions may take place both forward or in reverse. (a) CJoin is initially in state S_0 , which indicates that no signals are being processed. The presence or absence of signals on the input and output lines is irrelevant to the state here. (b) Depending on which input signal is absorbed first, the CJoin will assume the state S_{1a} or S_{1b} . (c) After both input signals are accepted by the CJoin, the state S_2 is assumed. (d) Depending on which signal is output first, the CJoin will assume the state S_{3a} or S_{3b} . (e) After outputting both signals, the CJoin returns to its initial state S_0 .

of CJoins. This tends to block signals from going backwards through CJoins, making their functionality forward-only. For the designs in this paper this does not impede the Brownian search process. In a search tree constructed from Hubs, Ratchets are usually placed at the root of the search tree to confine tokens to a minimal search space, like in the $n \times m$ -CJoin in Figure 6.

7 SINGLE ELECTRON TUNNELING CIRCUITS

Single Electron Tunneling (SET) circuits use tunneling of electrons as the underlying operating mechanism. The fundamental element in a SET circuit is a *tunneling junction*, which is a thin layer with high electrical resistance separating two Coulomb islands. Tunneling through a junction becomes possible when the voltage V_j over the junction exceeds a critical voltage V_c that depends on the capacitance of the junction and of the remainder of the circuit. Tunneling is a stochastic phenomenon: the transport of an electron over the junction experiences a delay of

$$t_d = \frac{-\log P_{\text{err}} R_j q_e}{|V_j| - V_c},$$

where R_j is the junction resistance and P_{err} is the probability that no transport has occurred after t_d seconds. Though tunneling is extremely fast (in the order

of picoseconds), it is unpredictable, making it less suitable for synchronously timed architectures. For this reason, research has been initiated on how SET could be used in the framework of token-based delay-insensitive circuits [24]. SET technology is especially suited to the token-based nature of such circuits, with tokens representing electrons or vacancies of electrons.

Can Brownian circuits be implemented with SET technology? We will first examine the assumptions made in more conventional SET circuits, before addressing their potential to implement Brownian circuits. In order to be used as tokens in Brownian circuits, electrons need to have a token-based character, but their wave-particle duality implies that this only holds under certain conditions. An electron's wave function extends through a potential barrier, thus spreading the electron over the Coulomb islands at both sides of the barrier. If this effect was to prevail there would be no localized charges of electrons, rendering token-based computations impossible. The quantized nature of an electron can be made more prominent by making the tunneling resistance sufficiently high. This ensures that the charging energy dominates over the quantum charge fluctuations. In other words:

$$\frac{q_e^2}{2 \cdot C_j} \cdot R_j \cdot C_j \gg h \implies R_j \gg h/q_e^2 = 25.8k\Omega$$

where h is Planck's constant, C_j is the tunnel capacitance and R_j is the tunneling resistance. The resistance of tunneling junctions in designs is usually chosen as $100k\Omega$ [2, 5, 9, 10, 14]. The token-based nature is fundamental to Brownian circuits, so the above requirement is important for them.

Another requirement for SET circuits concerns the thermal energy. If the thermal energy dominates over the charging energy E_c , tunneling is very likely to take place spontaneously, rather than controlled. The condition to avoid this is $E_c = \frac{q_e^2}{2 \cdot C} \gg k_B \cdot T$, where k_B is Boltzmann's constant and T is the absolute temperature. For a temperature of $1K$, for example, this equation implies that the capacitance of a Coulomb island should not exceed $926aF$. For higher temperatures, this capacitance is lower, which imposes a strict upper bound to the size of a quantum dot: For room temperature the capacitance should be less than $1aF$, which corresponds to an approximate diameter of $1nm$ in silicon. In the context of Brownian circuits, the above limitation is less strict, since spontaneous tunneling behavior has the potential to be employed for Brownian search. Implementations of SET circuits in terms of Brownian circuits may thus allow higher operating temperatures or larger feature sizes.

A preliminary study on implementations of Brownian circuits by SET technology has been conducted in [1, 25] (see Figures 14 and 15). This study focuses on a design of the Hub, as well as of a CJoin that is one-way, i.e., that

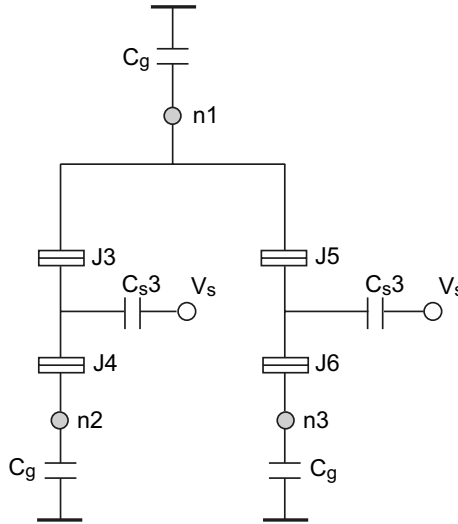


FIGURE 14

SET circuit of the Hub based on the design in [25]. The three wire terminals of the Hub are modeled by the Coulomb islands n_1 , n_2 , and n_3 . When there is an electron vacancy on n_1 , an electron is supplied from either n_2 or n_3 via junctions J_4 and J_3 , or J_6 and J_5 . Capacitance C_{s3} is chosen to be sufficiently low such that the thermal energy of the electron allows it to tunnel between n_1 and n_2 , or between n_1 and n_3 in a random fashion.

cannot reverse its tokens once they have been output. Though the CJoin in this study is different from the (two-way) CJoin in Figure 3, it can be considered as having ratchets attached to its output lines. Strictly spoken, the CJoin does not need Brownian search at its output sides (see Ratchet Condition in Section 6). Therefore, incorporating ratchets in a CJoin does not compromise the correctness of circuit designs. The one-way CJoin in combination with the Hub can thus be used as the basis of a universal set of primitives. The one-way design of the CJoin implies that fluctuations do not play an active role in its operation, unlike in the design of the Hub. The Hub and the CJoin thus work under somewhat different (but compatible) regimes of circuit parameters, the parameter settings of the Hub facilitating Brownian search, and the settings of the CJoin being more in line with deterministic behavior. Fluctuations in the Hub arise when the voltages over its tunneling junctions are brought close enough to their critical voltages such that electrons will tunnel forward and backwards through the junctions due to thermal energy. The thermal energy is thus effectively used as a random control voltage. The CJoin on the other hand is designed with buffering techniques in mind [10], such that the thermal energy has little or no effect on its behavior. In [1] a Half-Adder based on these SET-designs is simulated, confirming its correct behavior.

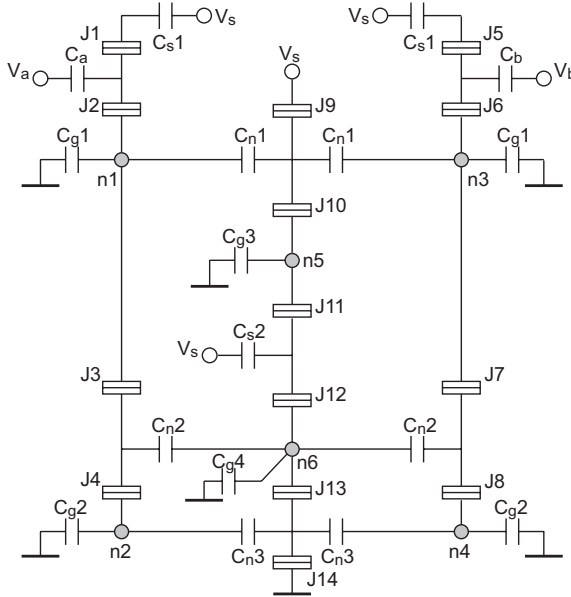


FIGURE 15

SET circuit of the CJoin [1]. Signals are input to the terminals V_a and V_b and the output terminals are modeled by the Coulomb islands n_2 and n_4 . When input V_a (resp. V_b) goes high, an electron will tunnel through J_2 and J_1 (resp. J_6 and J_5), resulting in a positive charge on n_1 (resp. n_3). When both V_a and V_b are high and thus n_1 and n_3 containing a positive charge, an electron will tunnel from n_5 through J_{10} and J_9 to the source V_s . This triggers the tunneling of an electron from n_6 to n_5 . The resulting positive charge at n_6 will cause tunneling of an electron from n_2 to n_1 through J_4 and J_3 and an electron from n_4 to n_3 through J_8 and J_7 . The resulting positive charges at n_2 and n_4 will then cause the charge in n_6 to flow to ground after an electron tunnels through J_{14} and J_{13} . This restores the circuit to its initial state.

8 CONCLUSIONS AND DISCUSSION

The trend towards nanocircuits that are switched by ever-decreasing numbers of particles will eventually lead to a regime where the law of large numbers ceases to hold. Fluctuations of signals will play a major role, requiring new ways to deal with the inherent decrease in reliability. Brownian circuits offer a new perspective in this context: they actively exploit fluctuations by searching through the state space of a circuit. This strategy allows decreased complexity of circuit primitives and circuit topologies, because it obviates the use of added circuitry to avoid the deadlocks common in conventional token-based circuits. The Brownian circuits in this paper are based on three primitives—the Hub, CJoin, and Ratchet—that are less complex than the primitives in [23], and that allow more straightforward circuit designs.

Simplicity of primitives and circuits are important factors contributing to the efficiency by which the circuits can be implemented physically.

Though Brownian circuits depend on fluctuations in their operation, they also need to restrict fluctuations to bias Brownian search away from directions not leading to output states. This is accomplished through the controlled use of Ratchets, which are placed so that they do not interfere with Brownian search, while also speeding up computations. When placed at the very beginning of the input lines of a circuit, Ratchets will lock in the input tokens, thus preventing the tokens from backing out from the circuit through the input lines. In general, Ratchets are placed so that they limit the Brownian search space to the bare minimum, yet do not block Brownian search where it is needed. At locations where Brownian search is indispensable Ratchets are left out. In [23] it is pointed out that the expected time for a token with unbiased fluctuations to move from one end of a line with length L to the other end scales with L^2 . When Ratchets are placed at constant distances D from each other, the token will be sped up by a factor of L/D on that line. Placement of Ratchets on output lines of circuits allows us to fix output of a circuit, so that signals cannot reenter it. Ratchets thus serve as buffers that isolate output of a circuit from the random fluctuations inside the circuit.

Single Electron Tunneling (SET) circuits, discussed in Section 7, are promising candidates for implementing Brownian circuits, because of the discreteness of their signals, which are represented as individual electrons, and because of the stochastic nature of tunneling, which fits well with the asynchronous nature of Brownian circuits. Discreteness in SET circuits manifests itself not only in the physical representation of a signal, but also in the position of a signal when it is physically represented by electrons held in Quantum dots. Quantum dots can be implemented in silicon [17], but molecular implementations are also possible, like in [20], where a single Co-ion bonded to a polypyridyl ligand behaves like a Coulomb island. In [3] tokens are represented by electrons in the bonds of molecules that are organized on a discrete grid.

Brownian circuits, unconventional as they may be, are no different from traditional circuits with respect to the range of functionalities they can realize. The logic design style for the Brownian circuits in this paper is based on Canonical Disjunctive Normal Forms, with CJoins encoding minterms and Hubs summing them. This implies that the complexity of designs is of the same order as in traditional logic, apart from a constant factor. There are differences too: whereas traditional electronic circuits employ voltage-encoded signals, Brownian circuits use tokens and they work without a clock. Due to this different framework, Brownian circuits need dual-rail encoding to represent logical values of signals, which requires a larger number of lines. Arbitration, on the other hand, is implemented more efficiently in Brownian

circuits, since it is inherent in the stochastic nature of Brownian search. Since Brownian circuits have the potential for implementations at integration densities exceeding conventional technology, the area required to implement a circuit may be significantly decreased, even when taking into account the overhead of dual-rail encoded lines.

Physical implementations of Brownian circuits are within the realm of possibilities, as simulations of designs based on Single Electron Tunneling technologies confirm. Other technologies may also be suitable for implementations, like spintronics, in which information is encoded by the spins of electrons. Though spintronics devices are less sensitive to quantum fluctuations as compared to SET, they are still subject to thermal fluctuations [18]. Another candidate is nanophotonics [16], where a token would represent an exciton—a quasi-particle consisting of an electron and electron hole, which results from the absorption of a photon in a semiconductor. In general, for a technology to be suitable for implementations of Brownian circuits, it is necessary that it supports a representation of signals that is token-based and that are subject to fluctuations.

REFERENCES

- [1] I. Agbo, S. Safruddin, and S.D. Cotozana. (2009). Implementable building blocks for fluctuation based calculation in single electron tunneling technology. In *Proc. 9th IEEE Int. Conf. on Nanotechnology (IEEE NANO)*, pages 450–453.
- [2] N. Asahi, M. Akazawa, and Y. Amemiya. (January 1998). Single-electron logic systems based on the binary decision diagram. *IEICE Transactions on Electronics*, E81-C(1):49–56.
- [3] A. Bandyopadhyay, R. Pati, S. Sahu, F. Peper, and D. Fujita. (April 2010). Massively parallel computing on an organic molecular layer. *Nature Physics*, 6(5):369–375.
- [4] C.H. Bennett. (1982). The thermodynamics of computation—a review. *International Journal of Theoretical Physics*, 21(12):905–940.
- [5] S. Cotozana, C. Lageweg, and S. Vassiliadis. (March 2005). Addition related arithmetic operations via controlled transport of charge. *IEEE Transactions of Computers*, 54(3):243–256.
- [6] R.M. Keller. (1974). Towards a theory of universal speed-independent modules. *IEEE Trans. Comput.*, C-23(1):21–33.
- [7] K. Kinoshita, R. Yasuda, H. Noji, and K. Adachi. (April 2000). A rotary molecular motor that can work at near 100% efficiency. *Philosophical Transactions of the Royal Society of London*, 355(1396):473–489.
- [8] L.B. Kish. (2006). Thermal noise driven computing. *Applied Physics Letters*, 89(14):144104–1–3.
- [9] C. Lageweg, S. Cotozana, and S. Vassiliadis. (2001). A linear threshold gate implementation in single electron technology. In *WVLSI '01: Proceedings of the IEEE Computer Society Workshop on VLSI 2001*, pages 93–98, Washington, DC, USA. IEEE Computer Society.

- [10] C. Lageweg, S. Cotofana, and S. Vassiliadis. (2002). Static buffered set based logic gates. In *Proceedings of the 2nd IEEE International Conference on Nanotechnology (IEEE Nano)*, pages 491–494, Arlington, USA.
- [11] J. Lee, S. Adachi, and F. Peper. (2011). A partitioned cellular automaton approach for efficient implementation of asynchronous circuits. *The Computer Journal*, 54(7):1211–1220.
- [12] J. Lee and F. Peper. (2008). On brownian cellular automata. In *Proc. of Automata 2008*, pages 278–291, UK. Luniver Press.
- [13] C. Mead and L. Conway. (1980). *Introduction to VLSI Systems*. Addison-Wesley Longman Publishing Co., Inc., Boston, MA, USA.
- [14] C. Meenderinck and S. Cotofana. (July 2007). Computing Division Using Single-Electron Tunneling Technology. *IEEE Transactions on Nanotechnology*, 6(4):451–457.
- [15] J.D. Meindl, Q. Chen, and J.A. Davis. (2001). Limits on Silicon Nanoelectronics for Terascale Integration. *Science*, 293(5537):2044–2049.
- [16] M. Ohtsu, K. Kobayashi, T. Kawazoe, T. Yatsui, and M. Naruse. (2008). *Principles of Nanophotonics*. Taylor & Francis.
- [17] Y. Ono, Y. Takahashi, K. Yamazaki, M. Nagase, H. Namatsu, K. Kurihara, and K. Murase. (2000). Fabrication method for IC-oriented Si single-electron transistors. *IEEE Trans. Electron Devices*, 47(1):147–153.
- [18] I.V. Ovchinnikov and K.L. Wang. (2008). Variability of electronics and spintronics nanoscale devices. *Applied Physics Letters*, 92(9):093503–1–3.
- [19] K.V. Palem. (2005). Energy aware computing through probabilistic switching: a study of limits. *IEEE Trans. Computers*, 54(9):1123–1137.
- [20] J. Park, A.N. Pasupathy, J.I. Goldsmith, C. Chang, Y. Yaish, J.R. Petta, M. Rinkoski, J.P. Sethna, H.D. Abruña, P.L. McEuen, and D.C. Ralph. (2002). Coulomb blockade and the Kondo effect in single-atom transistors. *Nature*, 417(6890):722–725.
- [21] P. Patra and D.S. Fussell. (1994). Efficient building blocks for delay insensitive circuits. In *Proceedings of the International Symposium on Advanced Research in Asynchronous Circuits and Systems (ASYNC)*, pages 196–205.
- [22] P. Patra and D.S. Fussell. (1996). Conservative delay-insensitive circuits. In *Workshop on Physics and Computation*, pages 248–259.
- [23] F. Peper, J. Lee, J. Carmona, J. Cortadella, and K. Morita. (2013). Brownian circuits: Fundamentals. *ACM Journal on Emerging Technologies in Computing Systems*, 9(1):3:1–24.
- [24] S. Safiruddin and S.D. Cotofana. (2007). Building blocks for delay-insensitive circuits using single electron tunneling devices. In *Proc. 7th IEEE Int. Conf. on Nanotechnology (IEEE NANO)*, pages 704–708.
- [25] S. Safiruddin, S.D. Cotofana, F. Peper, and J. Lee. (2008). Building blocks for fluctuation based calculation in single electron tunneling technology. In *Proc. 8th IEEE Int. Conf. on Nanotechnology (IEEE NANO)*, pages 358–361.
- [26] T. Yamada, M. Akazawa, T. Asai, and Y. Amemiya. (2001). Boltzmann machine neural network devices using single-electron tunnelling. *Nanotechnology*, 12(1):60–67.

Electronic structure near the Fermi level in the ferromagnetic semiconductor GaMnAs studied by ultrafast time-resolved light-induced reflectivity measurements

Tomoaki Ishii,¹ Tadashi Kawazoe,¹ Yusuke Hashimoto,² Hiroshi Terada,¹ Iriya Muneta,¹ Motoichi Ohtsu,¹ Masaaki Tanaka,^{1,3} and Shinobu Ohya^{1,3}

¹Department of Electrical Engineering and Information Systems, The University of Tokyo, 7-3-1 Hongo, Bunkyo-ku, Tokyo 113-8656, Japan

²WPI Advanced Institute for Materials Research, Tohoku University, 2-1-1 Katahira, Aoba-ku, Sendai 980-8577, Japan

³Center for Spintronics Research Network, Graduate School of Engineering, The University of Tokyo, 7-3-1 Hongo, Bunkyo-ku, Tokyo 113-8656, Japan

(Received 15 December 2015; revised manuscript received 3 May 2016; published 14 June 2016)

Clarification of the electronic structure near the Fermi level is important in understanding the origin of ferromagnetism in the prototypical ferromagnetic semiconductor GaMnAs. Here, we perform ultrafast transient reflectivity spectra measurement, which is a powerful tool for selective detection of absorption edges in GaMnAs. The results show that the Fermi level of GaMnAs exists in the band gap. By using the Kramers-Kronig relation, we find the Mn-induced electronic states around the Fermi level, confirming that the ferromagnetism is stabilized by spin-polarized impurity-band holes.

DOI: [10.1103/PhysRevB.93.241303](https://doi.org/10.1103/PhysRevB.93.241303)

GaMnAs is a prototypical ferromagnetic semiconductor that exhibits intriguing features originating from the interplay between ferromagnetic and semiconducting properties [1,2]. Although GaMnAs is the most investigated ferromagnetic semiconductor, its band structure and the origin of its ferromagnetism are still under debate. Over the past few years, the nature of the ferromagnetism of GaMnAs has been widely studied, with significant focus on the position of the Fermi level [3–16]. Recent experimental studies, including resonant tunneling [3,4], magnetic circular dichroism [5,6], and angle-resolved photoemission [7] experiments, concluded that the Fermi level of GaMnAs exists in the Mn-induced impurity band (IB) inside the band gap [8–12]. In this case, the ferromagnetism of GaMnAs is thought to be stabilized by spin-polarized IB holes [3,4,10]. There are also reports claiming that the Fermi level exists in the valence band (VB) [1,13–16]. In this case, the ferromagnetism would be induced by the itinerant spin-polarized VB holes; this spin polarization is due to p - d exchange interactions with localized d electrons [1]. Linear optical spectroscopy (LOS), which observes the absorption or transmission spectrum, has been widely used to investigate the band structure of semiconductors. However, in the case of GaMnAs, the LOS spectrum shows a broad peak at a photon energy close to the band gap, due to the overlap of the IB and the VB. Thus, it is difficult to determine the position of the Fermi level using LOS [11,17].

Here, we investigate the electronic structure near the Fermi level in GaMnAs through measurement of the transient reflectivity spectrum (TRS). We suggest that the TRS provides the effective means to determine the energy of the absorption edges as explained below [18]. The band structure of GaAs is schematically shown in Fig. 1(a). There is an absorption edge E_g corresponding to the optical transition from the top of the VB to the bottom of the conduction band (CB) [Fig. 1(a)]. In GaMnAs, due to the Mn-induced IB, there is another absorption edge E_F corresponding to the optical transition from the Fermi level to the bottom of the CB [Fig. 1(b)]. We note that this band picture is supported by recent studies of resonant tunneling spectroscopy and the angle-resolved photoemission spectroscopy, in which researchers observed a

sharp VB overlapped with the disordered and energetically broad IB [3,4,7,19–23]. In TRS experiments on GaMnAs, photocarriers are generated in the CB, VB, and IB by the illumination of a pump pulse, and the excited carriers relax to the band edges and to the Fermi level in the time scale of tens of picoseconds [24]. Thus, the transient reflectivity signal after 100 ps directly represents the photocarriers that are placed at the band edges and the Fermi level. The TRS measurement is thus sensitive to the absorption edges. Here, we analyze the signals using a model considering a combination of band-gap renormalization (BGR) and band filling (BF) [25,26]. Although a similar study was reported in Ref. [16], the excitation fluence, and thus the accumulation of photocarriers, was rather high; this can change the band structure because the BGR and/or BF [27] are too strong.

In this Rapid Communication, we demonstrate TRS measurements on a series of $\text{Ga}_{1-x}\text{Mn}_x\text{As}$ samples, in which the Mn concentration x is systematically varied from 0.1% to 6%. The pump pulse fluence was carefully chosen to avoid the aforementioned high-excitation effect. Our measurements show that the Fermi level is located in the band gap for all $\text{Ga}_{1-x}\text{Mn}_x\text{As}$ films examined in our study, and that there are Mn-induced electronic states around the Fermi level. Thus, our results support the IB conduction picture.

Time-resolved reflectivity measurements were performed using a degenerate (single-color) pump-probe technique. An 80-MHz picosecond pulsed laser, with a time duration of 3 ps, was chosen as the light source. Using the picosecond laser, a high energy resolution of 0.5 meV, which is much higher than in the previous studies using femtosecond pulses (~ 10 meV) [9,16], was achieved with a photodiode and a simple lock-in technique [see Sec. A of the Supplemental Material (SM) [28]]. The TRS was measured by changing the wavelength of the source laser. In our measurements, the fluences of the pump and probe pulses were 160 and 1 nJ/cm², respectively. The density of photocarriers in the GaMnAs film was estimated to be 8×10^{15} cm⁻³ by assuming that light penetrates into the sample at a distance of 800 nm from the surface. This photocarrier density is three orders of magnitude smaller than that in the previous study ($\sim 10^{19}$ cm⁻³) [16], thus

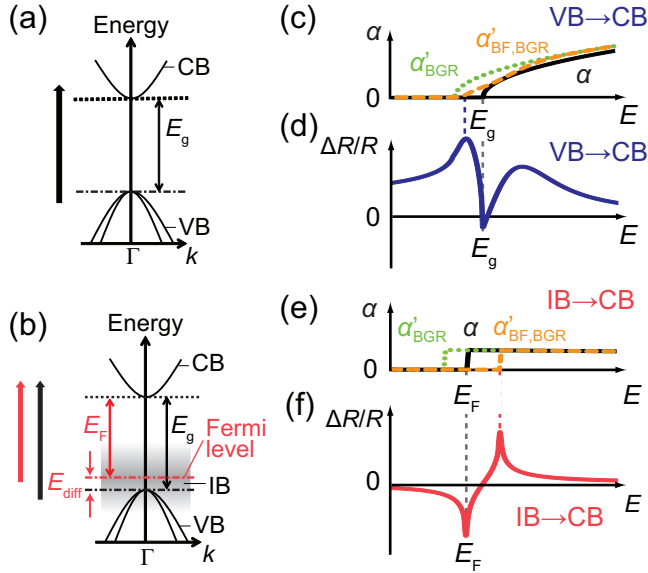


FIG. 1. (a), (b) Schematic illustration of the band structures of (a) GaAs and (b) GaMnAs with the optical transitions from the VB to the CB (black arrows) and from the IB to the CB (red arrow). The black dashed, red dashed-dotted, and black dashed-dotted horizontal lines represent the energy of the bottom of the CB, Fermi level, and the top of the VB, respectively. The gray region represents the IB region. (c), (e) Schematic absorption spectra; energy spectra of α (black solid curve), α'_{BGR} (green dotted curve), and $\alpha'_{\text{BF,BGR}}$ (orange dashed curve) associated with the optical transitions (c) from the VB to the CB and (e) from the IB to the CB. (d), (f) Calculated $\Delta R/R$ spectrum associated with the optical transitions (d) from the VB to the CB and (f) from the IB to the CB.

allowing accurate analysis and estimations (see Sec. D of the SM [28]). The photoinduced change in the reflectivity (ΔR) divided by static reflectivity R , ($\Delta R/R$), was detected with an accuracy of $\sim 10^{-4}$, using a lock-in technique as a function of the delay time t between the pump and probe pulses. Both the pump and probe pulses were linearly polarized.

For the pump-probe measurements, we used four $\text{Ga}_{1-x}\text{Mn}_x\text{As}$ films ($x = 0.1\%$, 1% , 3% , and 6%) with thicknesses of 20 nm. The GaMnAs layer was grown on a 100-nm-thick GaAs buffer layer on a semi-insulating (SI) GaAs (001) substrate by low-temperature molecular-beam epitaxy. The $\text{Ga}_{0.999}\text{Mn}_{0.001}\text{As}$ film was paramagnetic; all other GaMnAs samples were ferromagnetic. The Curie temperatures of the ferromagnetic $\text{Ga}_{0.99}\text{Mn}_{0.01}\text{As}$, $\text{Ga}_{0.97}\text{Mn}_{0.03}\text{As}$, and $\text{Ga}_{0.94}\text{Mn}_{0.06}\text{As}$ films were 13, 38, and 110 K, respectively.

In this study, we investigated the electronic structure near the Fermi level of GaMnAs in the following scenario. In GaMnAs, there are absorption edges E_g and E_F , as shown in Fig. 1(b). Reflecting the photon energy (E) dependence of the density of states of the VB and IB, the intrinsic absorption (α) spectrum associated with the transition from the VB to the CB is parabolic [black curve in Fig. 1(c)], while that associated with the transition from the IB to the CB is step-like near $E = E_F$ [black curve in Fig. 1(e)] (more details can be found in Sec. B in the SM [28]). The photogenerated holes excited by pump-pulse illumination gradually relax to the top of the VB or to the Fermi level by emitting optical and acoustic

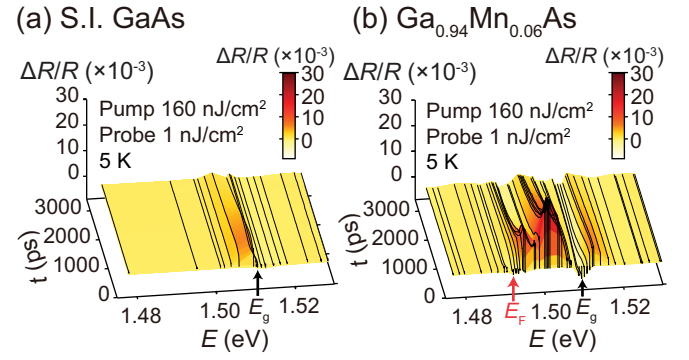


FIG. 2. (a), (b) Time evolution of $\Delta R/R$ (solid curves) as a function of the photon energy E measured at 5 K (a) for SI GaAs and (b) for $\text{Ga}_{0.94}\text{Mn}_{0.06}\text{As}$. The estimated E_g and E_F positions are indicated by the black and red arrows.

phonons on a time scale within ~ 100 ps [24]. Then, the photogenerated carriers induce two effects on the intrinsic absorption spectrum $\alpha-E$; one is the reduction of E_g via BGR [see $\alpha'_{\text{BGR}} - E$ in Figs. 1(c) and 1(e)], and the other is the suppression of absorption due to state filling, i.e., BF. These two effects change the absorption [see $\alpha'_{\text{BF,BGR}} - E$ in Figs. 1(c) and 1(e)] [25,27] and ΔR (see Sec. B of the SM [28]). Here, we define $\Delta\alpha$ as $\alpha - \alpha'_{\text{BF,BGR}}$. The $\Delta R/R$ spectrum can be derived from the $\Delta\alpha$ spectrum using the Kramers-Kronig relationship given by

$$\frac{\Delta R}{R} \propto \frac{c\hbar}{\pi} \text{P} \int_0^\infty \frac{\Delta\alpha}{E'^2 - E^2} dE', \quad (1)$$

where c is the speed of light in vacuum, and P denotes the Cauchy principal value of the integral. The calculated $\Delta R/R$ spectra from Figs. 1(c) and 1(e) are shown in Figs. 1(d) and 1(f), respectively. We see that the $\Delta R/R$ spectra have a dip at the intrinsic absorption edge (E_g or E_F). By comparing the model calculation with the experimental results, we determined E_g and E_F for all samples used in this study, as described later. Note that we can neglect the diffusion effect of holes in our measurement time scale (~ 150 ps) due to the low mobility of holes in GaMnAs (see Sec. E of the SM [28]).

To confirm that the $\Delta R/R$ signals are enhanced near the absorption edges due to transient photocarriers, we first measured the time evolution of the light-induced reflectivity for the SI GaAs substrate [Fig. 2(a)] and the $\text{Ga}_{0.94}\text{Mn}_{0.06}\text{As}$ sample [Fig. 2(b)] as a function of E at 5 K. We see that $\Delta R/R$ signals appear near the absorption edges E_g (black arrows) and E_F (red arrow) just after pump-pulse illumination, and that the $\Delta R/R$ signals disappear over a nanosecond time scale. These features can be attributed to the generation and recombination dynamics of photocarriers trapped at As_{Ga} antisites and holes at the VB edge and/or Fermi level [29].

To determine E_F and E_g from the experimental $\Delta R/R$ spectra measured at 5 K and at $t = 166$ ps [plotted data in Fig. 3(c)], we analyzed these $\Delta R/R$ spectra with Eq. (1) [solid curves in Fig. 3(c)]. As a result of the fitting, we derived the absorption spectra shown in Fig. 3(a) and $\Delta\alpha = \alpha'_{\text{BF,BGR}} - \alpha$ shown in Fig. 3(b) for $x = 6\%$. We clearly see absorption at E ranging from E_F to E_g [see the black solid curve in Fig. 3(a) and Sec. C in the SM [28] for other samples]. This is evidence

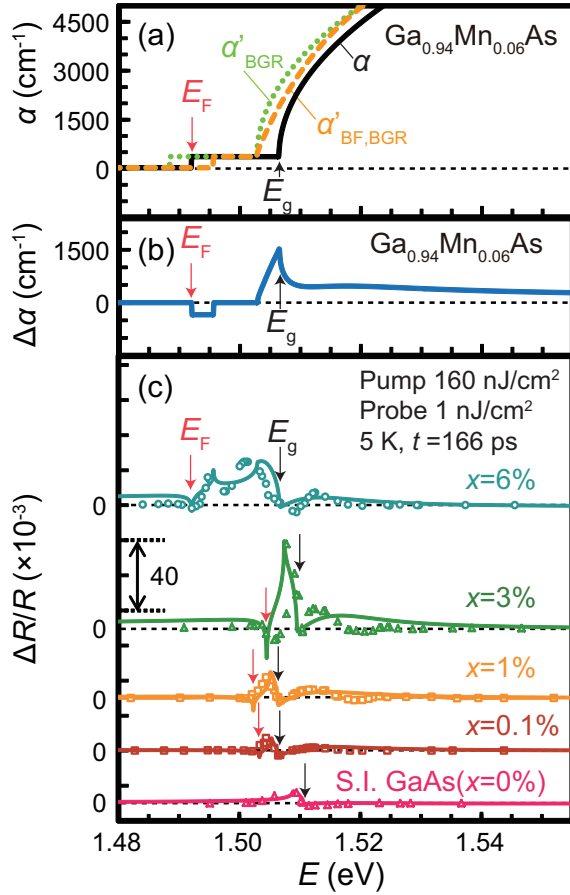


FIG. 3. (a) Absorption (α) spectra derived from the analysis of the TRS for Ga_{0.94}Mn_{0.06}As (black curve). This is composed of the optical transitions from the IB to the CB ($E > E_F$) and from the VB to the CB ($E > E_g$). The absorption spectrum when assuming that only the BGR occurs is shown by the (green) dotted curve. It is changed to the one shown by the (orange) dashed curve due to the BF in addition to the BGR. (b) $\Delta\alpha$ spectrum obtained for the Ga_{0.94}Mn_{0.06}As film. (c) $\Delta R/R$ spectra measured at 5 K for the SI GaAs substrate and for the Ga_{1-x}Mn_xAs films ($x = 0.1\%$, 1% , 3% , and 6%) at $t = 166$ ps (plotted data). The solid curves are the fitting curves.

of the presence of the IB inside the band gap in GaMnAs. In Fig. 3(c), E_F (red arrows) has a lower energy than E_g (black arrows) for all x . This indicates that the Fermi level exists in the band gap for all x .

Figure 4 shows the x dependence of the energy difference E_{diff} between the Fermi level and the top of the VB [see Fig. 1(b)] obtained from the data shown in Fig. 3(c). We found that E_{diff} increases with increasing x , as shown by the red diamonds in Fig. 4. These results are consistent with the data obtained by the resonant tunneling study in the region of $x > 1\%$ (blue circles in Fig. 4) [4] that revealed anomalous

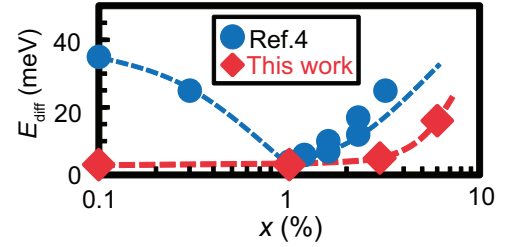


FIG. 4. x dependence of E_{diff} (red diamonds). The blue solid circles are the values reported in Ref. [4].

behavior of the Fermi level around $x = 1\%$; E_{diff} decreases in the region of $x < 1\%$, while E_{diff} increases in the region of $x > 1\%$ [4]. The reason for the difference in E_{diff} when $x < 1\%$ between this work and Ref. [4] may be explained by the following scenario. When $x < 1\%$, GaMnAs is insulating, and holes are localized near the Mn atoms. Thus, the optical transition probability from the localized impurity states to the CB is small, due to the small wave-function overlap between the localized photoholes and the photoelectrons. This leads to the small signal for $x = 0.1\%$ [Fig. 3(c)] and may make the correct derivation of the fitting parameters difficult. In the region of $x > 1\%$, the values of E_{diff} obtained in our study are slightly smaller than those obtained in previous reports [3,4]. This difference may be caused by the screening effect of the potential of the Mn atoms on photoexcited carriers or the small overestimation of E_{diff} in the resonant tunneling study due to series resistance. The most important feature of our results is that our TRS measurements successfully reproduced the anomalous behavior of the Fermi level when $x > 1\%$.

In summary, we studied the electronic structure near the Fermi level in GaMnAs by measuring the TRS using a low pump power (160 nJ/cm²) at a high energy resolution (~ 0.5 meV). The data show light-induced changes in the reflectivity spectra, attributed to BGR and BF. We reproduced the observed $\Delta R/R$ spectra in a calculation based on our band structure model, and found that the Fermi level is located in the band gap. We found Mn-induced electronic states near the Fermi level inside the band gap in all GaMnAs films studied here. This confirms that spin-polarized IB holes stabilize the ferromagnetism in GaMnAs.

This work was partially supported by Grants-in-Aid for Scientific Research including Specially Promoted Research, Project for Developing Innovation Systems of Ministry of Education, Culture, Sports, Science and Technology, Japan, and Spintronics Research Network of Japan. T.I. was supported by the Japan Society for the Promotion of Science through the Program for Leading Graduate Schools (MERIT). T.I. thanks the Japan Society for the Promotion of Science Research Fellowship Program for Young Scientists for support.

- [1] T. Dietl, H. Ohno, F. Matsukura, J. Cibert, and D. Ferrand, *Science* **287**, 1019 (2000).
 [2] M. Tanaka, S. Ohya, and P. N. Hai, *Appl. Phys. Rev.* **1**, 011102 (2014).

- [3] S. Ohya, K. Takata, and M. Tanaka, *Nat. Phys.* **7**, 342 (2011).
 [4] I. Muneta, H. Terada, S. Ohya, and M. Tanaka, *Appl. Phys. Lett.* **103**, 032411 (2013).

- [5] K. Ando, H. Saito, K. C. Agarwal, M. C. Debnath, and V. Zayets, *Phys. Rev. Lett.* **100**, 067204 (2008).
- [6] H. Terada, S. Ohya, and M. Tanaka, *Appl. Phys. Lett.* **106**, 222406 (2015).
- [7] M. Kobayashi, I. Muneta, Y. Takeda, Y. Harada, A. Fujimori, J. Krempaský, T. Schmitt, S. Ohya, M. Tanaka, M. Oshima, and V. N. Strocov, *Phys. Rev. B* **89**, 205204 (2014).
- [8] T. Matsuda and H. Munekata, *Phys. Rev. B* **93**, 075202 (2016).
- [9] S. Kim, E. Oh, J. U. Lee, D. M. Kim, S. Lee, and J. K. Furdyna, *Appl. Phys. Lett.* **88**, 262101 (2006).
- [10] M. Dobrowolska, K. Tivakornsasithorn, X. Liu, J. K. Furdyna, M. Berciu, K. M. Yu, and W. Walukiewicz, *Nat. Mater.* **11**, 444 (2012).
- [11] M. Yildirim, S. March, R. Mathew, A. Gamouras, X. Liu, M. Dobrowolska, J. K. Furdyna, and K. C. Hall, *Phys. Rev. B* **84**, 121202(R) (2011).
- [12] A. Patz, T. Li, X. Liu, J. K. Furdyna, I. E. Perakis, and J. Wang, *Phys. Rev. B* **91**, 155108 (2015).
- [13] T. Jungwirth, P. Horodyská, N. Tesařová, P. Němec, J. Šubrt, P. Malý, P. Kužel, C. Kadlec, J. Mašek, I. Němec, M. Orlita, V. Novák, K. Olejník, Z. Šobáň, P. Vašek, P. Svoboda, and J. Sinova, *Phys. Rev. Lett.* **105**, 227201 (2010).
- [14] T. Jungwirth, J. Sinova, A. H. MacDonald, B. L. Gallagher, V. Novák, K. W. Edmonds, A. W. Rushforth, R. P. Champion, C. T. Foxon, L. Eaves, E. Olejník, J. Mašek, S.-R. E. Yang, J. Wunderlich, C. Gould, L. W. Molenkamp, T. Dietl, and H. Ohno, *Phys. Rev. B* **76**, 125206 (2007).
- [15] O. Yastrubchak, J. Žuk, H. Krzyżanowska, J. Z. Domagala, T. Andrearczyk, J. Sadowski, and T. Wosinski, *Phys. Rev. B* **83**, 245201 (2011).
- [16] T. de Boer, A. Gamouras, S. March, V. Novák, and K. C. Hall, *Phys. Rev. B* **85**, 033202 (2012).
- [17] C.-H. Liu, N. M. Dissanayake, S. Lee, K. Lee, and Z. Zhong, *ACS Nano* **6**, 7172 (2012).
- [18] R. S. Joshya, A. J. Ptak, R. France, A. Mascarenhas, and R. N. Kini, *Phys. Rev. B* **90**, 165203 (2014).
- [19] R. Bouzerar and G. Bouzerar, *Europhys. Lett.* **92**, 47006 (2010).
- [20] A. X. Gray, J. Minár, S. Ueda, P. R. Stone, Y. Yamashita, J. Fujii, J. Braun, L. Plucinski, C. M. Schneider, G. Panaccione, H. Ebert, O. D. Dubon, K. Kobayashi, and C. S. Fadley, *Nat. Mater.* **11**, 957 (2012).
- [21] J. Okabayashi, A. Kimura, O. Rader, T. Mizokawa, A. Fujimori, T. Hayashi, and M. Tanaka, *Phys. Rev. B* **64**, 125304 (2001).
- [22] S. Ohya, I. Muneta, P. N. Hai, and M. Tanaka, *Phys. Rev. Lett.* **104**, 167204 (2010).
- [23] I. Muneta, S. Ohya, H. Terada, and M. Tanaka, *Nat. Commun.* (to be published).
- [24] J. Shah, *Ultrafast Spectroscopy of Semiconductors and Semiconductor Nanostructures*, Springer Series in Solid-State Sciences Vol. 115 (Springer, Berlin, 1999).
- [25] S. S. Prabhu and A. S. Vengurlekar, *J. Appl. Phys.* **95**, 7803 (2004).
- [26] C. V. Shank, R. L. Fork, R. F. Leheny, and J. Shah, *Phys. Rev. Lett.* **42**, 112 (1979).
- [27] B. R. Bennett, R. A. Soref, and J. A. D. Alamo, *IEEE J. Quantum Electron.* **26**, 113 (1990).
- [28] See Supplemental Material at <http://link.aps.org/supplemental/10.1103/PhysRevB.93.241303> for energy resolution (Sec. A), derivation of the fitting curves and fitting parameters (Sec. B), fitting results (Sec. C), pump-power dependence (Sec. D), and diffusion effect of holes (Sec. E).
- [29] M. Haiml, U. Siegner, F. Morier-Genoud, U. Keller, M. Luysberg, P. Specht, and E. R. Weber, *Appl. Phys. Lett.* **74**, 1269 (1999).

Evaluation of optical amplification properties using dressed photons in a silicon waveguide

H. Tanaka¹ · T. Kawazoe^{1,2} · M. Ohtsu^{1,2,3} · K. Akahane⁴ · N. Yamamoto⁴

Received: 22 June 2015 / Accepted: 7 August 2015 / Published online: 12 August 2015
© Springer-Verlag Berlin Heidelberg 2015

Abstract We fabricated an optical waveguide having a high optical confinement effect using a silicon-on-insulator substrate, and we eliminated the difficulty involved with optical alignment for making laser light pass through a p–n homojunction that is transparent to infrared light. Laser light was introduced via one of the cleaved edges of the optical waveguide and was guided to the transparent p–n homojunction, and the power of the light emitted from the other edge was measured. As a result, we successfully evaluated the optical amplification properties with high precision. For light with a wavelength of 1.31 μm , we obtained a differential gain coefficient of $g = 2.6 \times 10^{-2} \text{ cm/A}$, a transparency current density of $J_{\text{tr}} = 1 \text{ mA/cm}^2$, and a saturation optical power density of $P_{\text{sat}} = 30 \text{ kW/cm}^2$. The observation of gain saturation due to the incident optical power shows that this measurement method was suitable for evaluating the optical amplification properties.

1 Introduction

Silicon (Si) is an indirect transition-type semiconductor and has therefore been considered unsuitable as a material for light-emitting devices. However, if an infrared laser could be fabricated using Si bulk crystal as the lasing material, the transparency current density, J_{tr} , would become extremely small, and consequently, there would be a possibility of achieving an extremely small threshold current density, J_{th} . The main reason for this is that light absorption loss is small because the photon energy of infrared light is smaller than the bandgap energy, E_{g} , of Si. Other advantages include the natural abundance of Si as a raw material, the ease of integration with electronic circuits, and the ability to make use of the wealth of existing processing technologies that have already been developed for Si electronic devices [1].

Stimulated Raman scattering [2–5], crystal defects [6], Si nanocrystals [7], B-doped SiGe/Si quantum wells [8], etc. have recently been used to realize Si lasers; however, researchers have encountered problems that prevent the realization of practical devices, such as the difficulty of achieving room-temperature operation via current injection and insufficient quantum efficiency. To solve these problems, we have proposed a light emission principle based on dressed photons (DPs) [9], as well as a novel fabrication technique called dressed photon–phonon (DPP)-assisted annealing. A DP is a quasiparticle that represents a coupled state between a photon and an electron–hole pair in a nanoscale region [9]. DPs also couple with multimode coherent phonons [9], and the quasiparticle representing this coupled state is a DPP. By using this technique, we fabricated the world’s first infrared Si laser having a p–n homojunction structure and achieved continuous oscillation at room temperature (oscillation wavelength approximately

✉ H. Tanaka
tanaka@nanophotonics.t.u-tokyo.ac.jp

¹ Department of Electrical Engineering and Information Systems, Graduate School of Engineering, The University of Tokyo, 2-11-16 Yayoi, Bunkyo-ku, Tokyo 113-8656, Japan

² Specified Nonprofit Corporation Nanophotonics Engineering Organization, 1-20-10, Sekiguchi, Bunkyo-ku, Tokyo 112-0014, Japan

³ International Center for Nano Electron and Photon Technology, Graduate School of Engineering, The University of Tokyo, 2-11-16 Yayoi, Bunkyo-ku, Tokyo 113-8656, Japan

⁴ The National Institute of Information and Communications Technology, 4-2-1, Nukui-Kitamachi, Koganei, Tokyo 184-8795, Japan

1.3 μm ; threshold current density 1.2 kA/cm^2) [10]. More recently, we fabricated a laser having an optical waveguide with a large optical confinement factor and achieved a remarkably low threshold current density of 40 A/cm^2 [11].

In order to design a high-performance infrared Si laser, it is important to evaluate the optical amplification properties with high precision. In a conventional infrared laser using a direct-transition-type semiconductor, the optical amplification properties are evaluated by introducing light into the optical waveguide from the outside and measuring the power ratio relative to that of the emitted light [12]. In contrast to this approach, until now we have evaluated the optical amplification properties by using the photocurrent density generated in a Si photodetector (Si-PD) with optical gain [13]. By using this method, we can evaluate the features of Si as the laser medium, such as the optical gain and transparency current density, even though the device has a very small optical confinement factor, like a PD [11].

In the present research, we solved these technical problems and evaluated the optical amplification properties with high precision by using the evaluation method employed for conventional semiconductor lasers. To do so, we fabricated a wide optical waveguide using a silicon-on-insulator (SOI) substrate, and by increasing the optical confinement factor, we improved the alignment precision of the light incident on one cleaved edge of the optical waveguide and the measurement precision of the intensity of light emitted from the other edge. This enabled us to evaluate the saturation optical power density with high precision. This paper reports the results of this evaluation.

2 Device structure and DPP-assisted annealing conditions

The light emission principle, the structure of the SOI substrate used, the ion implantation profile for introducing boron (B) atoms, which are p-type dopants, and so forth were the same as those for the case of the infrared Si laser reported in our previous paper [11]. However, as shown in Fig. 1a, the width of the optical waveguide was increased to 750 μm (compared with 8 μm in the previous paper [11]). An overview of the SOI substrate is as follows. The device layer in the SOI substrate was P-doped n-type Si (resistivity 0.020–0.034 Ωcm) with a thickness of 15 μm . The thickness of the SiO_2 insulation layer was 2 μm , and the thickness of the Si support substrate was 575 μm . The concentration of B atoms doped in the device layer was $1 \times 10^{19}/\text{cm}^3$ (the maximum acceleration voltage for ion injection was 700 keV). From simulation calculations, the p–n homojunction interface was found to be at a depth of 1.5–2.5 μm from the surface of the SOI substrate.

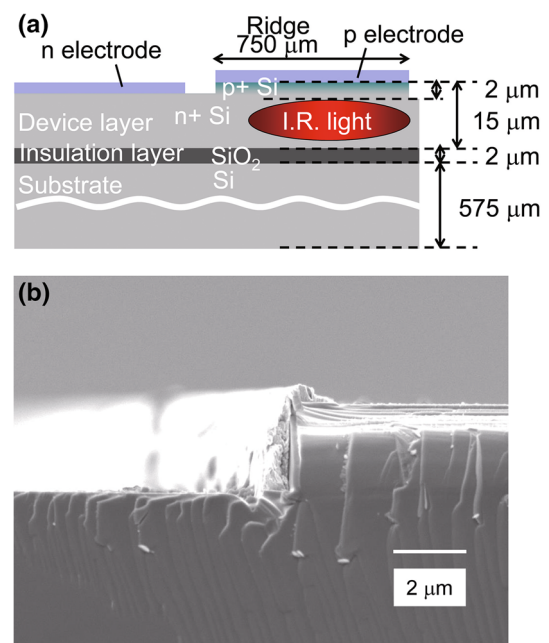


Fig. 1 **a** Schematic diagram of optical waveguide and **b** SEM image of edge of waveguide

After ion implantation, the substrate was cleaned by SPM (a 1:1 by volume solution of sulfuric acid/hydrogen peroxide) at 150 $^{\circ}\text{C}$ for 30 min and was washed with hydrofluoric acid. Next, we performed the following processes.

1. Chromium/platinum films (5-nm Cr/670-nm Pt) were deposited on the entire surface of the SOI substrate by RF sputtering.
2. The Cr/Pt films on the SOI substrate were coated with electron beam (EB) resist (OEBR-CAP112) by spin-coating. Then, the EB resist was patterned by EB lithography to leave a 750- μm -wide stripe.
3. The Cr/Pt films were etched by ICP-RIE using argon (Ar) gas.
4. Using the 750- μm -wide Cr/Pt stripe formed in Step 3 as a mask, the SOI substrate was etched with CF_4 gas to form a ridge-type optical waveguide (thickness 2 μm ; width 750 μm).
5. For use as current injection electrodes, Cr/Pt/Au films (with thicknesses of 5 nm/400 nm/400 nm) were deposited by RF sputtering.
6. To form positive (p) and negative (n) electrodes, the SOI substrate was again coated with an EB resist film, and EB lithography was performed.
7. The Cr/Pt/Au films were etched by ICP-RIE using Ar gas so as to form two separate electrodes, serving as positive and negative electrodes on the p layer and the n layer, respectively. Multiple optical waveguides were fabricated on the SOI substrate via the above processes.

8. The SOI substrate was diced by using stealth dicing to separate adjacent optical waveguides. The two edges of the optical waveguides were also cut by stealth dicing. The ridge-type optical waveguides had a width of 750 μm , a length of 2000 μm , and overall dimensions of 1.5 mm \times 2.0 mm.

Figure 1b is an SEM image of the edge of one of the waveguides after completing the processing. We confirmed that vertical etching was performed and that the ridge height was 2 μm , as designed.

DPP-assisted annealing was performed for 1 h by introducing laser light with a photon energy of $h\nu_{\text{anneal}} = 0.95$ eV (wavelength 1.31 μm) and a power of 40 mW via one of the cleaved edges of the optical waveguide while simultaneously injecting a triangular-wave current (current density 0–40 A/cm^2 , voltage 0–3 V, frequency 1 Hz) to bring about Joule heating. With this procedure, we fabricated an infrared Si light amplification device which was suitable for evaluating the optical amplification properties with high precision.

3 Measurement of differential gain coefficient, transparency current density, and saturation optical power

It is known that an infrared Si laser [10, 11] and an infrared Si LED [14] fabricated by DPP-assisted annealing emit light having the same energy as the photon energy, $h\nu_{\text{anneal}}$, of the light radiated during annealing. Therefore, we measured the optical amplification properties for light having a photon energy of $h\nu_{\text{anneal}} = 0.95$ eV (corresponding to a wavelength of 1.31 μm). Laser light was made to enter one of the cleaved edges of the optical waveguide (optical power, P_{in}), and after being guided through the optical waveguide, the power, P_{out} , of the light emitted from the other edge was measured. To take the measurement, we used an infrared camera having an InGaAs detector array (Xeva-1.7-320 manufactured by Xenics, wavelength range 0.9–1.7 μm). A triangular-wave current identical to that injected during annealing (current density 0–40 A/cm^2 , voltage 0–3 V, frequency 1 Hz) was injected into the device in order to amplify the incident optical power.

The measured dependency of the emitted optical power, P_{out} , on the injected current is shown in Fig. 2. The incident optical power, P_{in} , was 11 mW. We confirmed that the emitted optical power increased with increasing injected current. The relationship between the differential gain coefficient, g , and the injected current density, J , was determined from the expression $P_{\text{out}}/P_{\text{out}}(J = 0) = \exp(gJd)$, with reference to the value of P_{out} when the

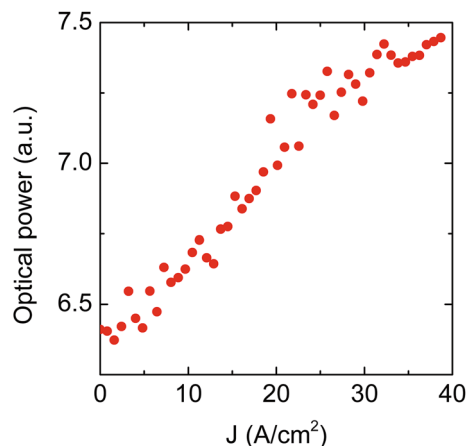


Fig. 2 Dependency of emitted optical power on injected current density at wavelength of 1.31 μm ($P_{\text{in}} = 11$ mW)

injected current density was 0. Here, d is the length of the waveguide ($\approx 2,000$ μm). The value of the optical gain G can be obtained from $G = gJ - \alpha$, based on the absorption loss of Si ($\alpha = 2.7 \times 10^{-5}/\text{cm}$) at the wavelength of 1.31 μm [15].

Figure 3 shows the measurement results for the dependency of G on J and the incident optical power, P_{in} . G was measured at 36 points in the range of incident optical powers $P_{\text{in}} = 0.6$ –140 mW. Figure 4 shows the dependency of G on J at $P_{\text{in}} = 11$ mW. The inset is a magnified view at $J = 0$. From these figures, since G was proportional to J at $J < 25$ A/cm^2 , these measurement results were fitted with a straight line. From the intersection of this straight line with the horizontal axis, the value of the transparency current density, J_{tr} , was determined to be 1 mA/cm^2 . In this measurement, the length of the gain layer through which the laser light passed was 1×10^3 times larger than that of the previous measurement using a

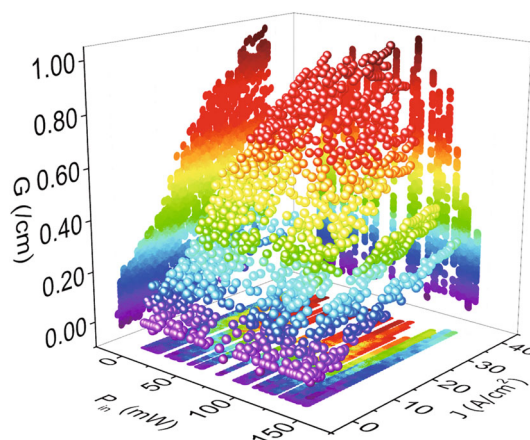


Fig. 3 Dependency of optical gain on incident optical power and injected current density at wavelength of 1.31 μm

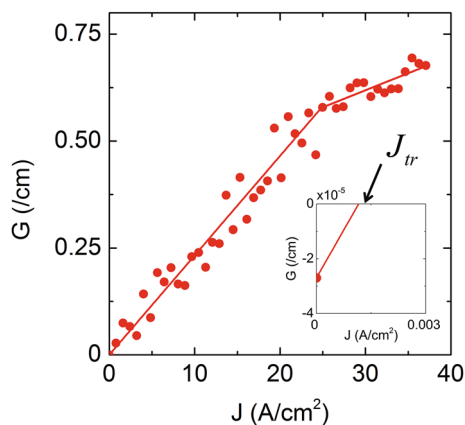


Fig. 4 Dependency of optical gain on injected current density at wavelength of 1.31 μm ($P_{\text{in}} = 11 \text{ mW}$)

Si-PD, and we could measure the amplified light precisely by making the spot size of the laser light ten times larger than that of the previous measurement. Thus, the volume involved with the optical gain was 1×10^4 times larger than the previous measurement. Therefore, the value of J_{tr} measured this time is different. Since we could estimate the value with higher precision in this measurement, we conclude that this value should be used in the design of future devices. In the region $J > 25 \text{ A/cm}^2$ in Fig. 4, the slope of the gain coefficient decreased slightly. In other words, slight gain saturation was observed. This is considered to be due to leakage current.

Figure 5 shows the dependency of the differential gain coefficient, g , on P_{in} . From this figure, at $P_{\text{in}} < 40 \text{ mW}$, g does not take a constant value but decreases as P_{in} decreases. This is because, when P_{in} is small, most of the electroluminescence (EL) is spontaneously emitted light, which spatially diverges, and therefore, it was not possible to collect and measure all of the emitted light. However, as

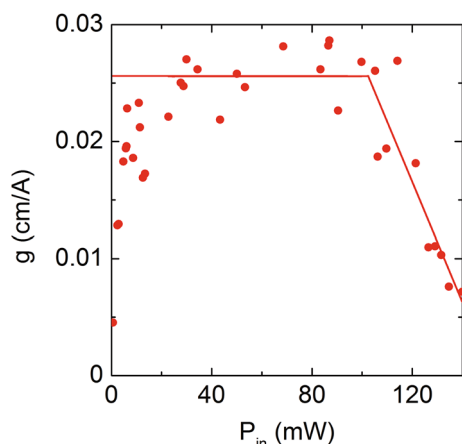


Fig. 5 Dependency of differential gain coefficient on incident optical power at wavelength of 1.31 μm

P_{in} increases, the EL power due to stimulated emission increases, and the directionality of the emitted light also increases, and therefore, the measurement precision for measuring P_{out} is improved. As a result, at $P_{\text{in}} > 40 \text{ mW}$, the measured value of g reaches a constant value of $2.6 \times 10^{-2} \text{ cm/A}$. On the other hand, at $P_{\text{in}} > 100 \text{ mW}$, g decreases as P_{in} increases. This indicates saturation of the optical gain. The above measurement results were fitted by the two straight lines in Fig. 5. This gain saturation has also been observed in conventional optical amplifiers using compound semiconductors [16], and therefore, we can conclude that this measurement method is suitable for evaluating the optical amplification properties. Although g takes a constant value of $2.6 \times 10^{-2} \text{ cm/A}$ in the center part of this figure, as described above, by estimating the value of P_{in} at which g is reduced by 3 dB from that value using the fitted straight line, a saturation power density of $P_{\text{sat}} = 30 \text{ kW/cm}^2$ was obtained.

4 Summary

We fabricated an optical waveguide having a high optical confinement effect using an SOI substrate, and the waveguide was endowed with gain by subjecting it to DPP-assisted annealing. Infrared laser light was introduced into the waveguide from one of the cleaved edges and was guided to the gain layer, which was formed of a p-n homojunction that was transparent to infrared light, and the power of light emitted from the other edge was measured. As a result, we were able to evaluate the optical amplification properties with high precision. For light with a wavelength of 1.31 μm , we obtained a differential gain coefficient of $g = 2.6 \times 10^{-2} \text{ cm/A}$, a transparency current density of $J_{\text{tr}} = 1 \text{ mA/cm}^2$, and a saturation power density of $P_{\text{sat}} = 30 \text{ kW/cm}^2$. Since we were able to observe gain saturation due to the incident optical power, we confirmed that this measurement method is suitable for evaluating the optical gain.


Acknowledgments This research was supported in part by Grant-in-Aid for JSPS Fellows Number 25 905 and the JSPS Core-to-Core Program, A. Advanced Research Networks. This research was performed in part by the Advanced ICT Research Institute of NICT.

References

1. L. Di, J.E. Bowers, Nat. Photonics **4**, 511 (2010)
2. H. Rong, A.L. Richard, J.O. Cohen, D.H.R. Nicolaescu, A. Fang, M. Paniccia, Nature **433**, 725 (2005)
3. R. Claps, D. Dimitropoulos, B. Jalali, IEEE Electron. Lett. **38**, 1352 (2002)
4. R.L. Espinola, J.I. Dadap, R.M. Osgood Jr, S.J. Mcnab, Y.A. Vlasov, Opt. Express **12**, 3713 (2004)

5. Y. Takahashi, Y. Inui, M. Chihara, T. Asano, R. Terawaki, S. Noda, *Nature* **498**, 470 (2013)
6. S.D. Cloutier, P.A. Kossyrev, J. Xu, *Nat. Mater.* **4**, 887 (2005)
7. M.J. Chen, J.L. Yen, J.Y. Li, J.F. Chang, S.C. Tsai, C.S. Tsai, *Appl. Phys. Lett.* **83**, 2163 (2004)
8. I.V. Altukhov, E.G. Chirkova, V.P. Sinis, M.S. Kagana, Y.P. Gousev, S.G. Thomas, K.L. Wang, M.A. Odnoblyudov, I.N. Yassievich, *Appl. Phys. Lett.* **79**, 3909 (2001)
9. M. Ohtsu, *Dressed photons-concepts of light matter fusion technology* (Springer, New York and London, 2013)
10. T. Kawazoe, M. Ohtsu, K. Akahane, N. Yamamoto, *Appl. Phys. B* **107**, 659 (2012)
11. H. Tanaka, T. Kawazoe, M. Ohtsu, K. Akahane, *Fluoresc. Mater.* (2015). doi:[10.1515/fma-2015-0001](https://doi.org/10.1515/fma-2015-0001)
12. Z.I. Kazi, T. Egawa, T. Jimbo, M. Umeno, *IEEE Photonics Technol. Lett.* **11**, 1563 (1999)
13. H. Tanaka, T. Kawazoe, M. Ohtsu, *Appl. Phys. B* **108**, 51 (2012)
14. T. Kawazoe, M.A. Mueed, M. Ohtsu, *Appl. Phys. B* **104**, 747 (2011)
15. M.A. Green, M.J. Keevers, *Prog. Photovolt.* **3**, 189 (1995)
16. J.L. Pleumeekers, M. Kauer, K. Dreyer, C. Burrus, A.G. Dentai, S. Shunk, J. Leuthold, C.H. Joyner, *IEEE Photonics Technol. Lett.* **14**, 12 (2002)

Non-scanning optical near-field microscopy for nanophotonic security

Naoya Tate¹  · Makoto Naruse² · Tsutomu Matsumoto³ · Morihisa Hoga⁴ · Yasuyuki Ohyagi⁴ · Shumpei Nishio⁴ · Wataru Nomura¹ · Motoichi Ohtsu⁵

Received: 1 July 2015 / Accepted: 22 July 2015 / Published online: 30 July 2015
© Springer-Verlag Berlin Heidelberg 2015

Abstract We propose a novel method for observing and utilizing nanometrically fluctuating signals due to optical near-field interactions between a probe and target in near-field optical microscopy. Based on a hierarchical structure of the interactions, it is possible to obtain signals that represent two-dimensional spatial patterns without requiring any scanning process. Such signals reveal individual features of each target, and these features, when appropriately extracted and defined, can be used in security applications—an approach that we call nanophotonic security. As an experimental demonstration, output signals due to interactions between a SiO₂ probe and Al nanorods were observed by using near-field optical microscopy at a single readout point, and these signals were quantitatively evaluated using an algorithm that we developed for extracting and defining features that can be used for security applications.

1 Introduction

In the critical-security battlefield, a defender tries to produce novel patterns that are difficult to accurately copy, and an attacker seeks a method to counterfeit such patterns [1]. Artifact metrics [2] is one of the most promising concepts for security applications. Artifact metrics utilizes various physical features unique to individual objects in terms of their physical properties, including their electromagnetic [3, 4], mechanical, and optical properties [5, 6]. Some results have been reported in actual implementations, such as ordinary paper [6], paper containing magnetic microfibers [7], plastics, and semiconductor chips. In particular, the essential characteristics of artifact metrics have been ascribed to a physical unclonable function [8]. On the other hand, recent technological advancements in micro-fabrication show promise for realizing various novel technologies that go beyond unclonable functions those developed so far, which have been limited to micrometer-scale precision. Against this background, we recently proposed and demonstrated the concept of *nano-artifact metrics*, which uses nanometer-scale unclonable patterns organized in a random manner [9], which is expected to offer robustness against cloning attacks.

As a further development of nano-artifact metrics, here we propose the concept of *nanophotonic security*, which is realized by combining nanophotonic principles [10–12] with the basics of nano-artifact metrics. Nanophotonics is a novel optical technology utilizing local interactions between nanometric particles via optical near fields. The optical near fields behave as a virtual cloud of photons that is constantly localized around nanometric materials illuminated by incident light. Since the virtual cloud of photons is localized in a region close to the electrons in the material, they can effectively interact with the materials in a unique manner [13].

✉ Naoya Tate
tate@ed.kyushu-u.ac.jp

¹ Faculty of Information Science and Electrical Engineering, Kyushu University, 744 Motoooka, Nishi-ku, Fukuoka 819-0395, Japan

² Photonic Network Research Institute, National Institute of Information and Communications Technology, 4-2-1 Nukui-kita, Koganei, Tokyo 184-8795, Japan

³ Graduate School of Environment and Information Sciences, Yokohama National University, Hodogaya, Yokohama, Kanagawa 240-8501, Japan

⁴ Dai Nippon Printing Co. Ltd., 250-1 Wakashiba, Kashiwa, Chiba 277-0871, Japan

⁵ Department of Electrical Engineering and Information Systems, The University of Tokyo, 2-11-16 Yayoi, Bunkyo-ku, Tokyo 113-8656, Japan

Exploiting the characteristic behavior of optical near fields for implementing optical devices and systems enables novel functions that would otherwise be impossible as long as conventional propagating light is used. In nanophotonic security, signals are read out by a nanometric *reader* from a nanometric *device*. Because such signals necessarily reveal specific individuality not only about the device but also about the reader, they are fundamentally difficult to be known from the nanometrical patterns of the reader and the device. Of course, unclonability of their nanometrical patterns is assured due to the basic concept of nano-artifact metrics. Based on these factors, nanophotonic security merits attention and is expected to lead to novel optical security techniques that will be essential for our sophisticated information society of the future.

Here, as an experimental demonstration of nanophotonic security, we propose using near-field optical microscopy (NOM) *without a scanning process* as a reader. In general, use of NOM entails a scanning process for observing a high-resolution two-dimensional image of spatially distributed optical near fields. However, such a process is not necessarily required in the case of our security applications, because only individual features of each device are required. Instead, appropriate definitions, evaluation of features, and corresponding signal processing are required. In this paper, first the concept and basic procedure of nanophotonic security based on non-scanning NOM are described. Then, results of some experimental demonstrations are shown, and the validity of our approach in an actual application is discussed.

2 Basic procedure

During the readout process in NOM, optical near-field interactions are induced between the nanometrical tip of a probe and a target. Due to these interactions, the readout signals reflect the degree of molecular attraction and the optical responses. By employing an autonomous control mechanism via a feedback structure in the setup, the probe is kept at a constant distance from the target. Here, we focus on inevitable fluctuations of the probe position during the readout process. Based on the concept of the inherent *hierarchy* of optical near-field interactions [14], interactions at various spatial scales are necessarily induced during these fluctuations. That is to say, NOM sequentially observes *compressed* information [15–17] about spatial patterns of the target from a single readout point, in other words without any scanning process. Figure 1 schematically summarizes the basic procedure of our proposed nanophotonic security system based on non-scanning NOM, from readout of the signals to extraction and evaluation of their features.

First, constantly fluctuating signals consisting of the optical responses and signals due to molecular attraction are read out by the non-scanning NOM. Generally, the frequency of such fluctuations can be directly controlled by setting the parameters of the experimental setup. Because the two fluctuating signals in Fig. 1a are obtained with the same time sequence, they can be combined to the single result shown in Fig. 1b. We plotted signals due to molecular attraction on the horizontal axis and signals due to optical responses on the vertical axis. Due to the feedback structure in the setup, the results show orbit-like modulation during the processing time. To allow simple evaluation of the result in Fig. 1b, binary image coding is performed, as shown in Fig. 1c, and the filled-in binary image is subjected to feature extraction. In this paper, the coordinates of corners in the image are defined and utilized as features of the obtained signals. In order to define and determine the coordinates of corners in the image, we employed the features from the accelerated segment test (FAST) [18] method. While various feature extraction methods have been actively studied [19–21] for realizing high-speed classification and searching of images, the FAST method is known to be one of the most effective methods. In the FAST method, only corners are defined as features of a target image, and decision tree analysis is employed to realize real-time processing. Finally, the coordinates of the corners found in each image are defined as individual features of the readout signals and corresponding device.

3 Experimental demonstration

In order to experimentally demonstrate our basic procedure, non-scanning NOM with a SiO₂ probe and Al nanorods was used as a reader and a device, respectively. The radius of curvature of the tip of the probe was less than 20 nm, and the tip was covered with a 50-nm-thick Au layer formed by sputtering, as shown in Fig. 2a. A resonance oscillator with an oscillating frequency of 32 kHz was attached to the probe for detecting molecular attraction between the probe and the device. The distance between the probe and the nanorods was set to be less than 50 nm. The nanorods were grown on a Si substrate by the glancing angle deposition (GLAD) method [22]. This method can realize various sizes, shapes, and constituents of nanorods by controlling multiple independent magnetron sources and three-dimensional rotation stage, which perform the deposition of materials by positioning a sample substrate over each magnetron at the appropriate distance and angle. We prepared two types of device, called *device 1* and *device 2*, which consisted of elements having diameters of 30 nm and 70 nm, as shown in Fig. 2b, c, respectively. All nanorods were grown in the direction vertical to the substrate, and they are slightly less than 200 nm in heights, in

Fig. 1 Basic procedure of nanophotonic security based on non-scanning NOM consists of **a** readout of optical responses and fluctuating signals due to molecular attraction, **b** producing two-dimensional plots of obtained signals, **c** image coding to produce filled-in binary patterns of the plotted results, and **d** feature extraction. In this paper, the coordinates of corners in each coded image are defined as features of the optical near-field interactions between the reader and the device

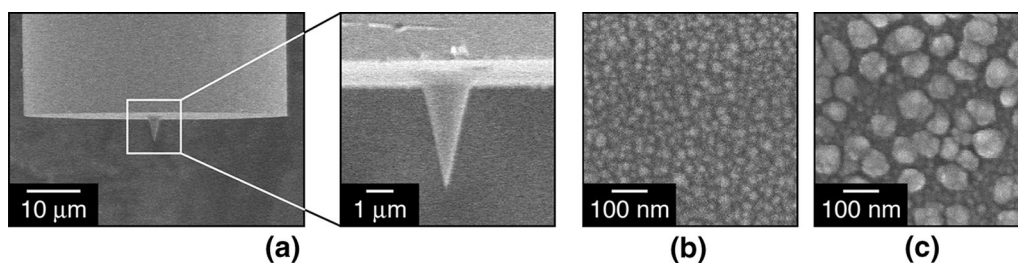
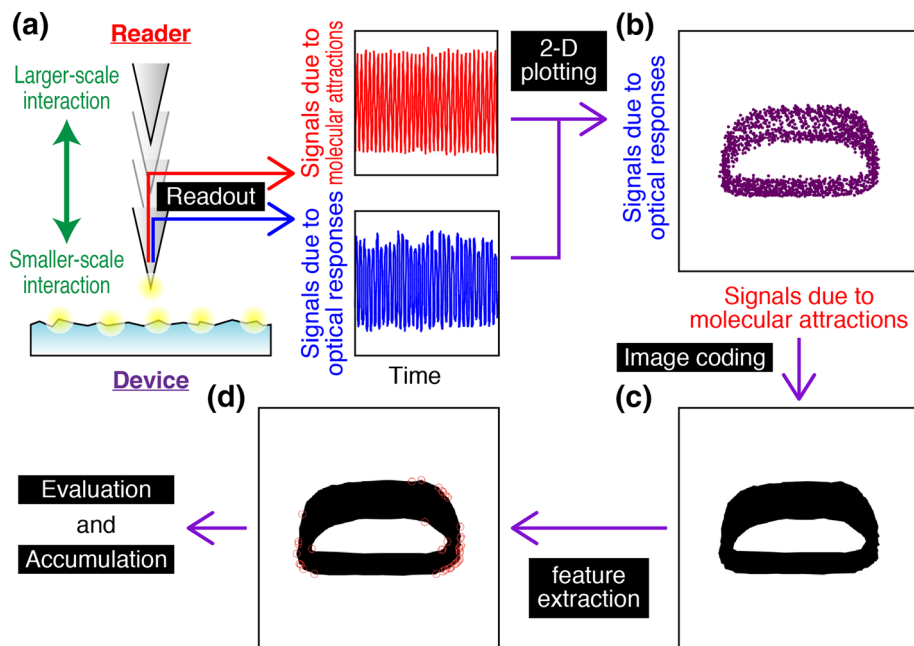


Fig. 2 SEM images of **a** tip of the probe of non-scanning NOM, and top views of nanorods in **b** device 1 and **c** device 2

both devices. A laser with a wavelength of 532 nm was used to induce optical near-field interactions and corresponding molecular attractions and optical responses. Signals due to the optical responses were detected by a photo-multiplier R-3896, manufactured by Hamamatsu Photonics, Japan, and read out as electrical signals, as well as molecular attractions.

Figure 3 shows the two-dimensional plot of the readout signals due to molecular attraction and the optical responses. For comparison, a single reader and two types of devices, device 1 and device 2, were used, and readout distances between the reader and each device are set at less than 50 nm; the plots for these devices are shown in Fig. 3a, b, respectively. A clear difference can be recognized between the two results.

To quantitatively evaluate the difference between the two results, both results were coded to produce filled-in binary patterns, and then, their corners were extracted as their individual features, as we described in the previous section. Then, in order to quantitatively evaluate these results,

we calculated *similarity values* by comparing the coordinates of the extracted corners of both images. Generally, the similarity value is defined as the Hamming distance between two sets of data. In our case, the coordinates of the corners were coded to a binary data set, and the two sets of data were compared with the other. As a result of this calculation, the similarity value between the two was calculated to be 0.10, when normalized to a maximum value of 1.00 in the case of self-similarity. The difference between the two values, 0.10 and 1.00, is sufficiently large for actual authentication between device 1 and device 2.

4 Discussion

In order to experimentally verify the validity of our proposed method and to quantitatively evaluate it using similarity values, other similarity values were obtained for various readout points on the target. We read out signals at discrete points on a single device and coded the results to

Fig. 3 Two-dimensional plots of readout signals by using non-scanning NOM with **a** device 1 and **b** device 2

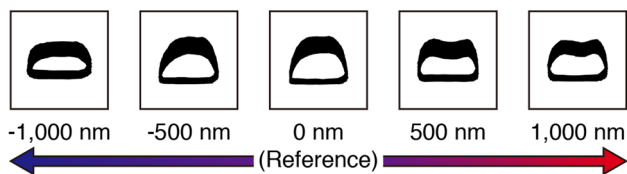
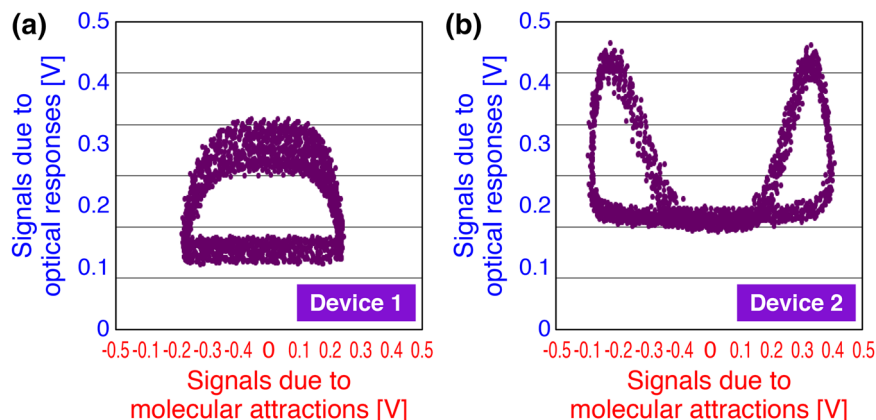


Fig. 4 Filled-in binary images obtained at discrete points on device 1, -1000 nm to $+1000$ nm away from a reference point

produce filled-in binary images, as shown in Fig. 4, which is the result with device 1.

One image is defined as a reference image, and we calculated the relative similarity values between the reference image and the others. Figure 5a, b shows calculated similarity values in the case of using device 1 and device 2, respectively. Additionally, at each point, we set two readout distances between the probe and the nanorods: One distance was set at about 100 nm, which we refer to as *farther readout*, and the other distance was set at less than 50 nm, which we refer to as *nearer readout*. In the case of farther readout, the spatial scale of the interactions between the probe and the device was much larger than in the case of nearer readout.

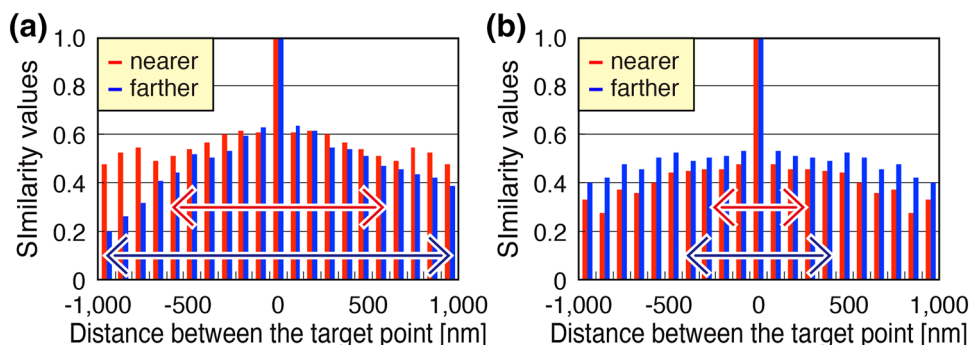
The main finding shown in these results is that all similarity values exhibited periodical increasing and decreasing. This indicates that the obtained signals at each

single readout point are the result of interactions between the probe and the spatial patterns of the nanorods, as we described in the previous section. If this were not the case, the fluctuations of the similarity values would be more random and steeper, but this was not observed. Furthermore, the difference in periods between the results of nearer readout and farther readout corroborates our hypothesis. For example, when using device 1, as shown in Fig. 5a, the pitches of the troughs are about 1200 nm and 2000 nm in the case of nearer readout and farther readout, respectively. Because the signals obtained with farther readout correspond to a larger spatial scale of interactions, the pitch of the increasing and decreasing similarity values becomes necessarily large. In the case of nearer readout, the opposite tendency was revealed. A similar comparison and reasoning also applies in the case where device 2 is used, as shown in Fig. 5b, where the results of nearer readout and farther readout showed trough pitches of about 500 and 800 nm, respectively.

5 Summary

With the goal of verifying the validity and effectiveness of nanophotonic security, we demonstrated the definition and acquisition of individual features of nanometric patterns

Fig. 5 Similarity values between the reference image and other discretely obtained images with two different readout distances [nearer readout (*red bars*) and farther readout (*blue bars*)] using **a** device 1 and **b** device 2



using non-scanning NOM. Our proposed method is suitable for application to actual situations as it takes only a short amount time, less than 1 s in our demonstrations, for the readout process, because it does not require the scanning process that is normally required when using NOM. This aspect, which was realized by exploiting nanometrically fluctuating signals due to optical near-field interactions, is expected to be a conceptual breakthrough not only for security applications but also for various applications related to optical information processing. Finally, although we produced filled-in binary images from readout fluctuating signals and extracted the coordinates of the corners in each image as individual features of each device, this procedure is just one possible procedure used to demonstrate the basic idea of our proposed method. Further studies will need to be performed to optimize each step in our proposed procedure.

The authors wish to thank Y. Pihosh, K. Mawatari, and T. Kitamori in the Department of Applied Chemistry at The University of Tokyo for their technical assistance in preparing the Al nanorods used for our experimental demonstrations. This work was partially supported by the JSPS Core-to-Core Program (A. Advanced Research Networks).

References

1. R.L. van Renesse, *Optical Document Security* (Artech, Morristown, 1994)
2. H. Matsumoto, T. Matsumoto, *IPSJ J.* **44**, 1991–2001 (2003)
3. D. Lim, J.W. Lee, B. Gassend, G.E. Suh, M. van Dijk, S. Devadas, *IEEE T. VLSI Syst.* **13**, 1200–1205 (2005)
4. G. DeJean, K. Darko, *Lect. Notes Comput. Sci.* **4727**, 346–363 (2007)
5. J.D. Buchanan, R.P. Cowburn, A.V. Jausovec, D. Petit, P. Seem, G. Xiong, M.T. Bryan, *Nature* **436**, 475 (2005)
6. M. Yamakoshi, J. Tanaka, M. Furuie, M. Hirabayashi, T. Matsumoto, *Proc. SPIE* **6819**, 68190H-1–68190H-10 (2008)
7. T. Ikeda, S. Hiroe, T. Yamada, T. Matsumoto, Y. Takemura, 3rd International Conference on Anti-counterfeiting, Security, and Identification in Communication 2009, pp. 382–385 (2009)
8. R. Pappu, B. Recht, J. Taylor, N. Gershenfeld, *Science* **297**, 2026–2030 (2002)
9. T. Matsumoto, in *Proceedings of the IEICE Symposium on Cryptography and Information Security*, SCIS 97-19C (1997)
10. K. Kobayashi, S. Sangu, H. Ito, M. Ohtsu, Near-field optical potential for a neutral atom. *Phys. Rev. A* **63**, 013806 (2001)
11. M. Ohtsu, K. Kobayashi, *Optical Near Fields* (Springer, Berlin, 2004)
12. Y. Tanaka, K. Kobayashi, Spatial localization of an optical near field in one-dimensional nanomaterial system. *Phys. E* **40**(2), 297–300 (2007)
13. M. Ohtsu, *Dressed Photons—Concepts of Light-Matter Fusion Technology* (Springer, Berlin, 2013)
14. M. Naruse, H. Hori, K. Kobayashi, M. Ishikawa, K. Leibnitz, M. Murata, N. Tate, M. Ohtsu, *J. Opt. Soc. Am. B* **26**(9), 1772–1779 (2009)
15. E. Candès, J. Romberg, T. Tao, *IEEE Trans. Inf. Theory* **52**, 489–509 (2006)
16. D. Donoho, *IEEE Trans. Inf. Theory* **52**, 1289–1306 (2006)
17. J. Haupt, R. Nowak, *IEEE Trans. Inf. Theory* **52**, 4036–4048 (2006)
18. E. Rosten, T. Drummond, in *European Conference on Computer Vision*, pp. 430–443 (2006)
19. C. Harris, M. Stephens, in *Alvey Vision Conference*, pp. 147–151 (1988)
20. S.M. Smith, J.M. Brady, *Int. J. Comput. Vision* **23**, 45–78 (1997)
21. D.G. Lowe, in *International Conference on Computer Vision*, pp. 1150–1157 (1999)
22. Y. Pihosh, I. Turkevych, J. Ye, M. Goto, A. Kasahara, M. Kondo, M. Tosa, *ECS Trans.* **16**(5), 49–58 (2009)

Spectral properties of a lateral p–n homojunction-structured visible silicon light-emitting diode fabricated by dressed-photon–phonon-assisted annealing

M. Yamaguchi¹ · T. Kawazoe^{1,3} · T. Yatsui^{1,2} · M. Ohtsu^{1,2,3}

Received: 30 June 2015 / Accepted: 10 August 2015 / Published online: 21 August 2015
© Springer-Verlag Berlin Heidelberg 2015

Abstract We developed a visible silicon light-emitting diode (Si-LED) with a lateral p–n homojunction using dressed-photon–phonon (DPP)-assisted annealing. The lateral p–n homojunction was fabricated in order to decrease the absorption loss inherent in light emission with a photon energy higher than the band-gap energy of the material. The fabricated Si-LED emitted light in the entire visible range, including the three primary colors. The light extraction efficiency of the Si-LED was estimated to be 7.8 times higher than that of a conventional LED structure with a vertical p–n homojunction. Owing to the efficient light extraction, we clearly observed two novel features in the electroluminescence (EL) spectrum: a nonlinear increase in the EL intensity with the injected forward current, and an emission peak at 2.7 eV, at which there is no singular point in the electronic structure. From these features, we concluded that the EL from the Si-LED originated from the phonon-assisted radiative recombination of carriers with much higher energy than that of the bottom of the conduction band, via DPPs.

1 Introduction

Silicon (Si) is considered to be an unsuitable material for light-emitting devices due to its indirect band-gap structure. In the past few decades, many researchers have tried to improve the light emission from Si in the visible range, mainly utilizing the quantum confinement effect in nanostructures, such as quantum dots [1–3] or porous Si [4–6]. However, achieving visible light emission from these nanostructures in order to fabricate practical optoelectronic devices is still a challenge due to the difficulty in injecting current. Visible luminescence has also been observed in a bulk Si crystal, originating from radiative recombination of hot carriers by using carrier injection via a scanning tunneling microscope [7], avalanche breakdown [8], or the Purcell effect in a plasmonic structure [9]. However, these light emission processes were realized under special conditions or photoexcitation and are difficult to be directly applied to optoelectronic devices.

To apply the EL from bulk Si crystal to practical devices, the authors have developed light-emitting diodes (LED) using a p–n homojunction [10–13]. By applying a method called dressed-photon–phonon (DPP)-assisted annealing [14], we realized an Si-LED with an external quantum efficiency of 15 % in the infrared band [10]. A dressed photon (DP) is a quasi-particle representing a coupled state of an electron–hole pair and a photon, and a DPP is a quasi-particle representing a coupled state of a DP and phonons. This DPP is generated around a suitable distribution of dopants after the DPP-assisted annealing process, which enables efficient light emission from Si. The photon energy of the light emitted from this Si-LED is identical to that of the laser light irradiated during the annealing process, regardless of the band-gap energy of Si ($E_g = 1.12$ eV). By utilizing this property, we have

✉ T. Yatsui
yatsui@ee.t.u-tokyo.ac.jp

¹ Department of Electrical Engineering and Information Systems, Graduate School of Engineering, The University of Tokyo, 2-11-16 Yayoi, Bunkyo-ku, Tokyo 113-8656, Japan

² International Center for Nano Electron and Photon Technology, Graduate School of Engineering, The University of Tokyo, 2-11-16 Yayoi, Bunkyo-ku, Tokyo 113-8656, Japan

³ Specified Nonprofit Corporation Nanophotonics Engineering Organization, 1-20-10, Sekiguchi, Bunkyo-ku, Tokyo 112-0014, Japan

succeeded in fabricating a visible Si-LED by irradiating it with visible laser light [13]. However, visible Si-LEDs have the intrinsic problem of a low light extraction efficiency originating from large absorption loss. Since semiconductors generally absorb light with a photon energy higher than E_g , visible photons emitted by the p–n homojunction in the Si-LED are absorbed before they reach the surface of the LED. To improve the light extraction efficiency, this absorption loss must be reduced.

In the present paper, we developed a visible Si-LED with a lateral p–n homojunction. Since radiative recombination of electron–hole pairs occurs near the surface in this structure, the absorption loss is expected to be lower. After forming the p–n homojunction by the laser doping method, DPP-assisted annealing was conducted to enhance the light emission of the Si-LED. Due to the resultant high extraction efficiency, we observed two novel features in the EL spectrum. One is that the EL intensity nonlinearly increased with the injected forward current. The other is that an emission peak was observed at a photon energy of 2.7 eV, even though there is no singular point in the electronic structure of Si. These features indicate that light emission from the visible Si-LED originates from the phonon-assisted recombination of carriers with higher energy than that of the bottom of the conduction band, via DPPs.

The paper is organized as follows. In Sect. 2, we describe the principle of light emission from bulk Si. In Sect. 3, we present the fabrication process of the Si-LED with the lateral p–n homojunction. In Sect. 4, we discuss the experimental results, mainly the obtained EL spectrum and its dependence on the forward bias. Finally, we summarize our work in Sect. 5.

2 Principle of light emission

The light emission from the Si crystal presented in this paper utilizes DPPs [14]. The origin of DPPs has been theoretically derived [15], and they have been experimentally observed [16] at the tip of a glass probe. In semiconductor crystals, DPPs are also generated and localized at dopant distributions [10, 17]. Using DPPs, the difference between the wavevector of an electron and that of a hole, which prevents radiative recombination in indirect-transition-type semiconductors, is compensated by the wavevector of a phonon, because DPPs strengthen the coupling between an electron–hole pair and a phonon by several orders of magnitude [12]. Therefore, the DPPs in the crystal enable light emission with high efficiency.

To induce the light emission process via DPPs, a dopant distribution that efficiently generates DPPs is required. By applying the annealing method that we developed, called DPP-assisted annealing, such dopant distributions are

formed in a self-organized manner. In DPP-assisted annealing, a forward current is injected into the device while irradiating it with laser light having a photon energy $\hbar\omega_{\text{anneal}}$.

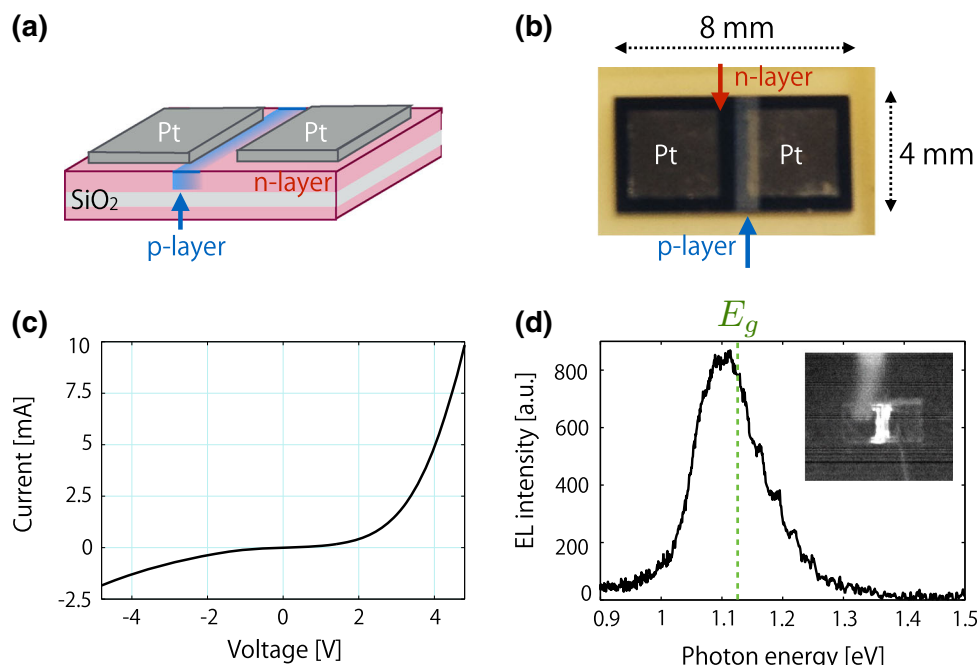
Here, we describe the physical mechanism by which the dopant distribution is modified in DPP-assisted annealing. After starting annealing, heat is generated in the device by absorption of the laser irradiation and Joule heating caused by the injected current. As a result, the dopant atoms are thermally diffused, causing their microscopic distribution to vary. During this diffusion process, there is a probability of forming a dopant distribution that efficiently generates DPPs. Around such a distribution, radiative recombination of electron–hole pairs is enabled by coupling with phonons induced by the DPPs. Therefore, a photon that enters the dopant distribution produces a photon with the same energy as that of the incident photon via stimulated emission. Since the generated photon is radiated outside the dopant distribution, one part of the thermal energy is dissipated, reducing the heat generation. Therefore, the thermal diffusion rate of the dopants in the region in which DPPs are efficiently generated is low compared with that in the region in which DPPs are hardly generated. Consequently, the number of regions having the dopant distribution that efficiently generates DPPs increases through the DPP-assisted annealing process. Note that the formed dopant distribution is suitable for emitting a photon with energy $\hbar\omega_{\text{anneal}}$, the same as that of the laser light irradiated during DPP-assisted annealing. This is because the process of modifying the dopant distribution involves stimulated emission, and the probability of spontaneous emission is proportional to that of stimulated emission. Therefore, the fabricated Si-LED is expected to efficiently emit photons with a photon energy $\hbar\omega_{\text{anneal}}$. Indeed, the EL enhancement around $\hbar\omega_{\text{anneal}}$ has been observed experimentally for other Si-LEDs fabricated by the DPP-assisted annealing [10–13].

3 Fabrication process

The fabrication process was basically the same as that presented in Ref. [13]. However, in this study, we fabricated a lateral p–n junction, as schematically illustrated in Fig. 1a, to reduce the absorption loss. Fabricating a p–n homojunction structure by ion implantation is costly and is thus unsuitable for mass production. Therefore, we adopted the laser doping method, which is suitable for forming a lateral p–n homojunction due to its ability to selectively inject dopants by irradiating the required regions with laser light.

The detailed fabrication process was as follows. First, to serve as electrodes, we deposited chromium/platinum (Cr/Pt) layers with a total thickness of 300 nm on an n-type

Fig. 1 Schematic diagram and photograph of the Si-LED with the lateral p–n homojunction, and its basic properties. **a** Schematic diagram of the structure of the Si-LED with the lateral p–n homojunction. **b** Photograph of the device after laser doping. **c** Voltage–current characteristic of the Si-LED. **d** EL spectrum of the band-edge emission under a forward bias of 15 V. The green dashed line indicates E_g of Si. The relatively broad linewidth originates from the high voltage applied to the device. The inset shows a photograph of the Si-LED acquired by a CCD camera in the infrared region



silicon-on-insulator (SOI) substrate in which the thickness of the device layer was 10 μm and the resistivity was 0.5 $\Omega\text{ cm}$. The sizes of the substrate and the electrodes were 4 mm \times 8 mm and 3 mm \times 3 mm, respectively. Second, we spin-coated B-doped Si nanocrystals (NanoGram® Si ink) with a B density of $1 \times 10^{20}\text{ cm}^{-3}$ on a half of the substrate, and then irradiated it with pulsed laser light having a photon energy of 2.35 eV and a fluence of 4.0 J/cm² to melt the nanocrystals and form a B-doped p-layer. A photograph of the Si-LED after the laser doping process is shown in Fig. 1b. The region shown as the p-layer is the region irradiated with the pulsed laser light.

Figure 1c, d shows the fundamental properties of the fabricated Si-LED. Both the rectification property seen in the current–voltage characteristic in Fig. 1c and the band-edge emission in the EL spectrum in Fig. 1d clearly indicate that a lateral p–n homojunction was successfully formed by the laser doping process.

Finally, we conducted DPP-assisted annealing by applying a forward bias of 15 V and irradiating the device with CW laser light having a photon energy $\hbar\omega_{\text{anneal}} = 3.06$ eV and an intensity of 8.0 W/cm² for 3 h in order to enhance the visible luminescence from the Si-LED.

4 Results and discussion

Figure 2 shows the EL spectra of the fabricated Si-LED under a forward bias of 15 V during the DPP-assisted annealing. The black, blue, and red curves show the EL spectra measured before, and after 30 and 90 min of

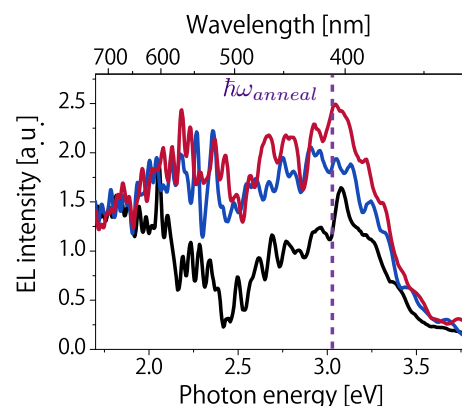


Fig. 2 The EL spectra of the Si-LED under a forward bias of 15 V during the DPP-assisted annealing. The black, blue, and red curves indicate the spectra measured before, and after 30 and 90 min of annealing, respectively. The purple dashed line shows $\hbar\omega_{\text{anneal}}$, the photon energy of the laser irradiated during the annealing

annealing, respectively. Even before the annealing, the Si-LED exhibited visible luminescence with mainly two peaks at 1.9 and 3.0 eV. From the photon energy, the origin of the EL at 3.0 eV is attributed to the direct transition of electrons at the singular point Γ in the band structure of Si, which satisfies the wavenumber conservation law. On the other hand, the origin of the EL at 1.9 eV is attributed to the radiative transition of electrons at the L point via scattering by phonons, because electrons and phonons are weakly coupled even before the DPP-assisted annealing. To the best of our knowledge, there has never been a report of visible EL from a p–n homojunction formed in bulk Si

crystal. The EL that we observed is attributed to the increase in the light extraction efficiency realized by the lateral p–n homojunction.

Figure 2 shows that the visible EL spectra is enhanced at photon energies between 2.0 eV and 3.3 eV, which are around and below $\hbar\omega_{\text{anneal}}$. The selective emission enhancement around $\hbar\omega_{\text{anneal}}$ by the DPP-assisted annealing implies that the enhanced EL originates from the coupling between an electron–hole pair and a phonon via DPPs.

Figure 2 also shows that the Si-LED emitted light in the entire visible wavelength region, including the three primary colors. The photograph of the Si-LED under a forward bias of 15 V shown in Fig. 3a, captured by a CCD camera, confirms that there are spots that generate each of the three primary colors. We consider that the color of the light generated at each spot on the lateral p–n homojunction in Fig. 3a is dependent on the local microscopic distribution of the p-type dopant B.

Figure 3b shows the time evolution of the EL intensity of red (590–700 nm), green (490–590 nm), and blue (400–490 nm). The intensities were normalized by the intensities before the DPP-assisted annealing. We can see from this figure that the annealing time required for the EL enhancement was approximately 90 min for all colors. The most enhanced color was green, corresponding to energies below $\hbar\omega_{\text{anneal}}$. In theory, the DPP-assisted annealing should fundamentally lead to emission around $\hbar\omega_{\text{anneal}}$ [10, 13]. The difference in the photon energy at which the EL is enhanced between the theory and the actual fabricated visible Si-LED is attributed to a radiative recombination

process involving phonon emission, which decreases the photon energy of the emitted light.

Here, we evaluate the improvement in light extraction efficiency achieved by the lateral p–n homojunction, by comparing the present device with our previously fabricated Si-LED having a conventional LED structure with a vertical p–n junction [13]. We consider that the light emission process of these Si-LEDs is the same due to following two reasons: (1) Both LEDs were fabricated using bulk Si doped with the p-type dopant B and were irradiated with laser light having the same photon energy of 3.05 eV during the DPP-assisted annealing. (2) In the EL spectra of both LEDs, two emission peaks were observed at around 2 eV and 3 eV. Based on (1) and (2), we define the relative light extraction efficiency η_r as $I_{3\text{eV}}/I_{2\text{eV}}$, that is to say, the EL intensity of the Si-LED at 3 eV relative to that at 2 eV. Since the absorption coefficient of Si at 3 eV is two orders of magnitude larger than that at 2 eV [18], η_r takes a large value in a device from which the generated light can be efficiently extracted without absorption loss. The value of η_r for the Si-LED with the vertical p–n junction structure [13] is calculated to be 0.14, whereas that of the present Si-LED with the lateral p–n junction is 1.10. These values mean that the lateral p–n homojunction is expected to improve the light extraction efficiency in the blue band by 7.8 times.

Next, we discuss the physical process of the light emission from the visible Si-LED. The emission process in the infrared band using DPPs [10, 12] has been attributed to the coupling between electron–hole pairs and phonons. Although visible emission from the Si-LED is also considered to originate from phonon coupling [13], clear evidence confirming the emission process has not yet been presented. Through the evaluation and discussion given below, we show that the emission from the visible Si-LED originates from phonon-assisted radiative recombination carriers with a higher energy than that of the bottom of the conduction band.

Figure 4a shows the EL spectra of the Si-LED under various forward biases. Under high voltages, EL emission in a high-energy band around 3.0 eV becomes dominant. Consequently, the Commission Internationale de l'Éclairage (CIE) chromaticity coordinate largely shifts toward the blue with increasing applied bias, from $(x, y) = (0.343, 0.359)$ at a forward bias of 8 V (an injection current of 30 mA) to $(0.286, 0.288)$ at 24 V (518 mA), as shown in Fig. 4b. Such a large shift of the chromaticity is generally not observed in conventional LEDs fabricated using compound semiconductors with a direct band-gap structure.

Figure 4c shows the current versus emission intensity characteristic. The emission intensity of the Si-LED was derived by integrating the EL spectrum in the visible range shown in Fig. 4a. In contrast to LEDs fabricated using

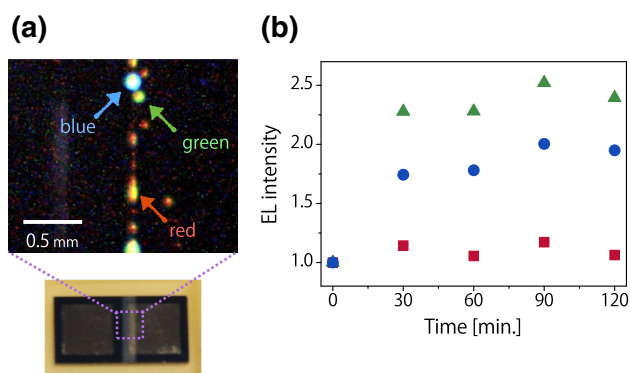


Fig. 3 Photograph and time evolution of the EL at three primary colors. **a** Photograph of the Si-LED after the DPP-assisted annealing under a forward bias of 15 V, captured by a CCD camera in the visible range. **b** Time evolution of the EL intensities of the three primary colors of light, red (590–700 nm), green (490–590 nm), and blue (400–490 nm), during the DPP-assisted annealing. All the intensities were normalized to the EL intensities before annealing

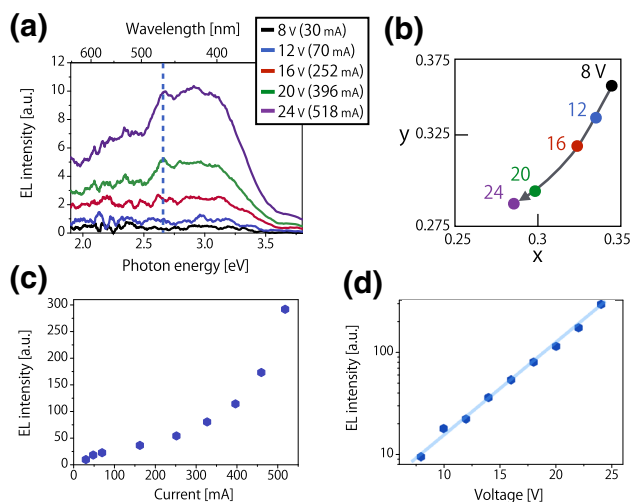


Fig. 4 The dependences of the EL of the Si-LED on the applied forward bias. **a** The EL spectra of the visible Si-LED under forward biases and currents of 8 V (30 mA), 12 V (70 mA), 16 V (252 mA), 20 V (396 mA), and 24 V (518 mA). **b** The dependence of the Commission Internationale de l'Éclairage (CIE) chromaticity coordinate of the Si-LED on the forward bias. The colors at each bias condition correspond to those of the EL spectra in (a). **c** The current versus emission intensity characteristic and **d** the voltage versus emission intensity characteristic of the Si-LED

compound semiconductors that exhibit linear power versus current characteristics, the characteristic of the visible Si-LED is nonlinear. This nonlinearity shows that the emission from the visible Si-LED is derived from hot electrons with much higher energy than the bottom of the conduction band, as described below.

Figure 4d shows the voltage versus emission intensity characteristic. Since it is fitted to a straight line in a semilog plot, the optical power of the Si-LED exponentially increases with the forward bias. We note that the photon energy of the EL emission from the Si-LED shown in Fig. 4a is much higher than E_g of Si ($= 1.12$ eV). Therefore, the EL intensity is proportional to the density of carriers with a higher energy than that of the bottom of the conduction band. In general, the density of electrons with a high energy E depends on the applied forward bias V as $n(E) \propto e^{\frac{qV}{k_B T}}$, where q , k_B , and T are the electronic charge, Boltzmann's constant, and temperature, respectively. Therefore, an exponential power versus voltage characteristic is confirmed by taking account of the fact that the EL of the Si-LED is derived from carriers with high energy, because the density of high-energy carriers is proportional to the exponential of the forward bias. Furthermore, the change of the CIE chromaticity coordinate is accounted for by the scenario that the large bias increases the ratio of high-energy carriers. Consequently, the luminescence in the high-energy band becomes dominant, and

the chromaticity shifts to the blue, which is consistent with the EL spectra shown in Fig. 4a.

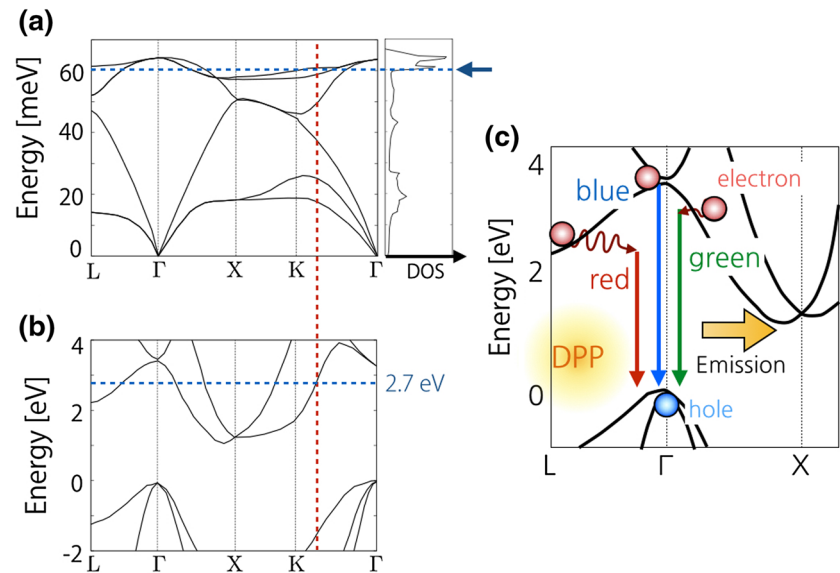
Figure 4a shows another feature of the visible Si-LED, namely, an emission peak at 2.7 eV, represented by the vertical blue dashed line. Since the EL spectrum before the DPP-assisted annealing, shown by the black curve in Fig. 2, has two peaks at 1.9 and 3.0 eV originating from the electronic structure of Si, the peak at 2.7 eV is expected to be involved in an optical process via DPPs as a result of the DPP-assisted annealing. When an electron–hole pair recombines by interacting with a phonon, the wavevector of the phonon has to be the same as that of the electron due to the wavenumber conservation law. The density of states (DOS) of phonon modes in Si has a peak at approximately 60 meV, as shown in the right part of Fig. 5a, corresponding to the wavevector between Γ and K points, as indicated by the blue dashed line (since the other peak of the DOS at 65 meV corresponds to the Γ point with a wavenumber of zero, its contribution to the light emission process in the Si-LED is regarded as being negligible). The red and blue dashed lines shown in Fig. 5a, b indicate that the electron in Si with the same wavevector as that of the phonon with a high DOS has an energy of approximately 2.7 eV. Due to the agreement between the energy of the emission peak observed in the EL spectrum shown in Fig. 4a and the energy of an electron with the wavevector corresponding to the high DOS of the phonon, we conclude that the emission from the visible Si-LED originates from the coupling between an electron–hole pair and a phonon.

Based on the forward bias dependence of the spectrum shown in Fig. 4 and the emission peak at 2.7 eV originating from the coupling between the electron–hole pair and the phonon, the light emission from the visible Si-LED originates from phonon-assisted recombination of a hot electron and a hole via DPPs, as illustrated in Fig. 5c. This description obtained based on the present experimental results is consistent with the results observed in infrared Si-LEDs using DPPs [10, 12].

5 Summary

We developed a visible Si-LED with a lateral p–n homojunction using the DPP-assisted annealing method. The lateral p–n homojunction, adopted to increase the light extraction efficiency, was formed by laser doping. The resultant light extraction efficiency of the Si-LED in the blue band was estimated to be 7.8 times higher than that of a conventional LED structure with a vertical p–n homojunction. Furthermore, we observed two novel features in the EL spectrum: an exponential increase of EL intensity with the applied forward bias, and a characteristic emission

Fig. 5 The contribution of the coupling between the electron–hole pair and the phonon via DPPs. **a** The dispersion relation and the density of states (DOS) of phonons in Si, based on Ref. [19]. **b** The electronic structure of Si, based on Ref. [20]. **c** Schematic illustration of the emission process in the visible Si-LED



peak at 2.7 eV. From a consideration of these features, we concluded that the light emission from the visible Si-LED originates from phonon-assisted radiative recombination of carriers with a higher energy than that of the bottom of the conduction band, via DPPs.

Acknowledgments The authors thank Teijin Co. Ltd. for providing the NanoGram® Si ink. This work was partially supported by a MEXT Grant-in-Aid for Scientific Research (B) (No. 26286022), a MEXT Grant-in-Aid for Exploratory Research Program (No. 26630122), and the JSPS Core-to-Core Program (A. Advanced Research Networks).

References

1. W. Wilson, P. Szajowski, L. Brus, *Science* **262**, 1242 (1993)
2. S. Cloutier, P. Kosyrev, J. Xu, *Nat. Mater.* **4**, 887 (2005)
3. F. Maier-Flaig, J. Rinck, M. Stephan, T. Bocksrocker, M. Bruns, C. Kubel, A. Powell, G. Ozin, U. Lemmer, *Nano Lett.* **13**, 475 (2013)
4. L. Canham, *Appl. Phys. Lett.* **57**, 1046 (1990)
5. A. Cullis, L. Canham, *Nature* **353**, 335 (1991)
6. J. Park, L. Gu, G. von Maltzahn, E. Ruoslahti, S. Bhatia, M. Sailor, *Nat. Mater.* **8**, 331 (2009)
7. P. Schmidt, R. Berndt, M. Vexler, *Phys. Rev. Lett.* **99**, 246103 (2007)
8. R. Newman, *Phys. Rev.* **100**, 700 (1955)
9. C. Cho, C. Aspetti, J. Park, R. Agarwal, *Nat. Photon.* **7**, 285 (2013)
10. T. Kawazoe, M. Mueed, M. Ohtsu, *Appl. Phys. B* **104**, 747 (2011)
11. N. Wada, T. Kawazoe, M. Ohtsu, *Appl. Phys. B* **108**, 25 (2012)
12. M. Yamaguchi, T. Kawazoe, M. Ohtsu, *Appl. Phys. A* **115**, 119 (2014)
13. M. Tran, T. Kawazoe, M. Ohtsu, *Appl. Phys. A* **115**, 105 (2013)
14. M. Ohtsu, *Dressed Photons: Concepts of Light–Matter Fusion Technology* (Springer, Berlin, 2013)
15. Y. Tanaka, K. Kobayashi, *J. Microsc.* **229**, 228 (2008)
16. T. Kawazoe, K. Kobayashi, S. Takubo, M. Ohtsu, *J. Chem. Phys.* **122**, 024715 (2005)
17. Y. Tanaka, K. Kobayashi, *Phys. E* **40**, 297 (2007)
18. M. Green, M. Keevers, *Progr. Photovoltaics Res. Appl.* **3**, 189 (1995)
19. P. Giannozzi, S. de Gironcoli, *Phys. Rev. B* **43**, 7231 (1991)
20. K. Sieh, P. Smith, *Phys. Status Solidi (b)* **129**, 259 (1985)

Optimization of dressed-photon–phonon-assisted annealing for fabricating GaP light-emitting diodes

Jun Hyoung Kim¹  · Tadashi Kawazoe^{1,2} · Motoichi Ohtsu^{1,2,3}

Received: 30 June 2015 / Accepted: 28 August 2015 / Published online: 7 September 2015
© Springer-Verlag Berlin Heidelberg 2015

Abstract Using the two-level two-state model, we analyzed the characteristics of enhanced electroluminescence intensity from a GaP LED fabricated by dressed-photon–phonon-assisted annealing. In this model, we utilized the fact that the adiabatic potential barrier of the electronic excited level in configuration space is lower than that of the ground level. It was confirmed by experiments that, in an actual excited level, the barrier was reduced to 0.48 eV. From this finding, it was shown that the spatial distribution of Zn atoms can be changed by means of current injection and light irradiation even at room temperature. In addition, we showed that a structure that is suitable for light emission via DPPs is formed by means of a transition between a low-barrier excited level and a high-barrier ground level, due to stimulated emission. Also, regarding the optimized conditions for maximizing the effect of DPP-assisted annealing, it was found that the optimum ratio of the number of injected electrons to the number of irradiated photons is close to 1, and this was confirmed experimentally.

1 Introduction

The light emission color of a light-emitting diode (LED) using a direct-transition-type semiconductor depends on the bandgap energy, E_g , of that semiconductor. In addition, by adjusting the molar ratios in mixed crystal materials, it is possible to change the value of E_g . These features, together with development of recent crystal growth techniques, have resulted in the development of LED technology using InGaN or AlGaInP. However, in the case of InGaN, when the molar ratio of In increases, the crystallinity deteriorates [1, 2]. With AlGaInP, on the other hand, when the molar ratio of In decreases, the material becomes an indirect-transition-type semiconductor, and light emission becomes impossible [3, 4]. Because of these problems, it has not been possible to obtain materials that efficiently emit light in the vicinity of a wavelength of 550 nm (photon energy 2.25 eV). On the other hand, the II–VI family of semiconductors that include Cd have a high environmental load [5].

To solve the above problems, a method using GaP ($E_g = 2.26$ eV) has been proposed [6]. However, GaP is an indirect-transition-type semiconductor, and the bottom of the conduction band and the top of the valence band are at different positions in reciprocal lattice space; therefore, the law of conservation of momentum must be satisfied in order for electron–hole pairs to radiatively recombine. In other words, an electron–phonon interaction is required, but the probability of such an interaction is low. To satisfy the law of conservation of momentum, a method in which isoelectronic impurities, such as N atoms, are introduced into GaP has been used for a long time [7]. In this method, the wave function in reciprocal lattice space is made wider by localizing electrons. However, since light emission occurs via localized levels in the forbidden band, part of

✉ Jun Hyoung Kim
kimjh@nanophotonics.t.u-tokyo.ac.jp

¹ Department of Electrical Engineering and Information Systems, Graduate School of Engineering, The University of Tokyo, 2-11-16 Yayoi, Bunkyo-ku, Tokyo 113-8656, Japan

² Specified Nonprofit Corporation Nanophotonics Engineering Organization, 1-20-10, Sekiguchi, Bunkyo-ku, Tokyo 112-0014, Japan

³ International Center for Nano Electron and Photon Technology, Graduate School of Engineering, The University of Tokyo, 2-11-16 Yayoi, Bunkyo-ku, Tokyo 113-8656, Japan

the energy is lost, and therefore, it is not possible to sufficiently use the large E_g possessed by GaP.

However, when dressed-photon–phonon-assisted annealing (DPP-assisted annealing), a novel technique that we have proposed, is applied to a GaP crystal, it is possible to fabricate an LED which overcomes the problems described above [6]. A dressed photon (DP) is a quasiparticle representing the coupled state of a photon and an electron–hole pair in a nano-size region [8]. A dressed-photon–phonon (DPP) is a quasiparticle representing the coupled state of a DP and multimode coherent phonons [8, 9]. Therefore, the law of conservation of momentum is satisfied by the interaction of an electron and multimode coherent phonons, and even an indirect-transition-type semiconductor can be used to fabricate an LED.

Using this method, we have successfully developed LEDs using Si and SiC, which are indirect-transition-type semiconductors [10, 11]. We were also able to considerably enhance the light emission in the band of 2.2 eV and above, even in the case of GaP [6]. In the work described in this paper, we used the two-level two-state (TLTS) model [12, 13] to analyze how the spatial distribution of dopant atoms changes when fabricating an LED by subjecting GaP to DPP-assisted annealing. We also present optimum conditions for the DPP-assisted annealing and report the results of experiments conducted to confirm the optimum conditions.

2 DPP-assisted annealing and principle of device fabrication

Light emission via DPPs occurs due to the property that DPs strongly couple with local-mode phonons [8, 9]. According to previous research, when two or more dopant atoms that are lighter than the atoms forming the host crystal are close to each other, strongly localized phonons exist at that location [9]. When two adjacent dopant atoms are aligned in the Γ – X direction, phonons are localized at that location, and a DP couples with those phonons, forming a DPP. This DPP has a momentum necessary for electrons at the bottom of the conduction band (X point) in GaP to recombine with holes at the top of the valence band (Γ point). Therefore, when an electron in the conduction band interacts with the DPP, the law of conservation of momentum is satisfied, and light emission becomes possible, even in an indirect-transition-type semiconductor. Phonons are localized even when three or more dopant atoms are adjacent to each other; in practice, however, the concentration (10^{17} – $10^{19}/\text{cm}^3$) of the p-type dopant atoms (Zn atoms) that we injected was not high enough for three or more atoms to be adjacent to each other. Therefore, in

the rest of this paper, we consider the case where two Zn atoms are adjacent to each other.

The principles of light emission via DPPs will be described using Fig. 1. Figure 1a is an energy band diagram of GaP in the case where there are no DPPs. Since electron–hole recombination is forbidden, excited electrons have a long lifetime. Therefore, the electrons relax while interacting with multiple phonons over a long period of time, generating heat.

If the spatial distribution of Zn atoms is suitable for locally generating DPPs, the energy band diagram is as shown by the expanded view in Fig. 1b. In this case, since momentum is supplied to the electrons from multimode coherent phonons, the dispersion relation of the DPPs is represented by multiple straight lines parallel to the horizontal axis. In the figure, el in the ket vectors represents an electron, g represents the ground state, and ex and ex' represent excited states. When an electron is injected from outside, an initial state $|E_{ex};el\rangle \otimes |E_{thermal};phonon\rangle$ is formed [10, 11]. Then, via intermediate states

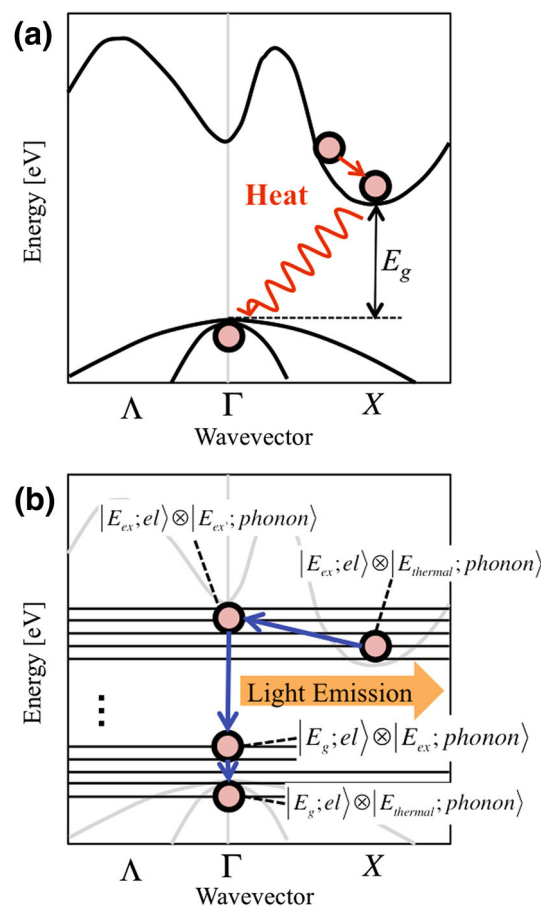


Fig. 1 Light emission via a DPP-assisted process. **a** Relaxation of electron in an indirect-transition-type semiconductor. **b** Light emission process via DPP levels

$|E_{ex};el\rangle \otimes |E_{ex};\text{phonon}\rangle$ and $|E_g;el\rangle \otimes |E_{ex};\text{phonon}\rangle$ coupled with the phonon excited state, the electron finally transitions to the ground state $|E_g;el\rangle \otimes |E_{\text{thermal}};\text{phonon}\rangle$ [9–11]. This process is an electric-dipole-allowed transition, and therefore, propagating light is generated.

Next, the reason why an indirect-transition-type semiconductor emits light via DPP-assisted annealing will be described.

With the conventional doping method, position control of the individual Zn atoms is difficult. To achieve such control, we cause the positions of the Zn atoms to change in a self-organized manner using DPP-assisted annealing [8, 10]. In other words, a forward current is injected into the GaP substrate, in which a p–n homojunction is formed by ion implantation, to perform annealing, and the spatial distribution of the Zn atoms is changed by using the generated thermal energy. During this annealing, the substrate is irradiated with light. Here, atomic coupling is mediated by the outermost shell electrons. Since electrons are injected into the excited level during DPP-assisted annealing, interatomic coupling is different from the case where electrons are in the ground level. Therefore, the barrier height for a state transition also changes [12, 13]. That is the reason why we should consider a model with two levels shown in Fig. 2. This model is widely used for treating the energy of systems below the adiabatic approximation, such as for explaining the spectral hole-burning phenomenon [12]. Here, state B means a local structure suitable for generating DPPs; in other words, adjacent Zn pair is aligned in Γ –X direction so that enables light emission via DPP levels inside the GaP [16]. State A represents other structures, in other words, local structures that are not suitable for generating DPPs. When the electron is in an excited level, the barrier height for a transition

is lowered (changes in this barrier height will be discussed quantitatively in Sect. 4).

In the following, we explain two different cases, according to the spatial distribution of the Zn atoms.

- (state A) Regions where the spatial distribution of Zn atoms is not suitable for generating DPPs: The injected electrons generate heat inside the crystal due to scattering processes. In addition, electrons excited by absorbing the irradiated light also generate heat inside the crystal. In other words, in the excited level, since the barrier height V_{ex} in Fig. 2 is low, and since heat is also generated locally, the spatial distribution of dopants is easily changed.
- (state B) Regions where the spatial distribution of Zn atoms is suitable for generating DPPs: As explained in Fig. 1b, since electron–hole pairs can radiatively recombine, stimulated emission is brought about by external light, and the electrons return to the ground level in Fig. 2. In this level, therefore, the barrier height V_g is high. Also, heat generation is suppressed. Therefore, it is difficult for the Zn atoms to widely diffuse, and thus their spatial distribution cannot be easily changed.

When DPP-assisted annealing is performed, due to the different diffusion rates in regions (1) and (2), the spatial distribution of Zn atoms changes to a spatial distribution that is suitable for stimulated emission via the DPPs. In addition, since the probability of stimulated emission is highly proportional to the probability of spontaneous emission [14], an LED can be realized by using DPP-assisted annealing.

3 Fabrication process

First, an n-type (S concentration, 2×10^{17} to $4 \times 10^{17}/\text{cm}^3$) GaP single-crystal substrate with a surface orientation of (111) was injected with Zn atoms, serving as a p-type dopant, using ion injection to form a p–n homojunction. The peak concentration of the injected Zn atoms was $1 \times 10^{19}/\text{cm}^3$. Then, electrodes were deposited on both surfaces of the substrate by sputtering. An Au/Zn/Ni film with a thickness of 150 nm was deposited on the front surface of the device, that is, the p-type side, and an Au/Ge/Ni film with a thickness of 300 nm was deposited on the rear surface of the device, that is, the n-type side. In particular, the electrodes on the p-type side were patterned into a mesh shape by a lift-off process. This was to allow irradiation light and EL light to be transmitted during DPP-assisted annealing and during driving, respectively. Then, the substrate was diced into a $550 \mu\text{m} \times 550 \mu\text{m}$ chip, which was fixed to a PCB by soldering the negative

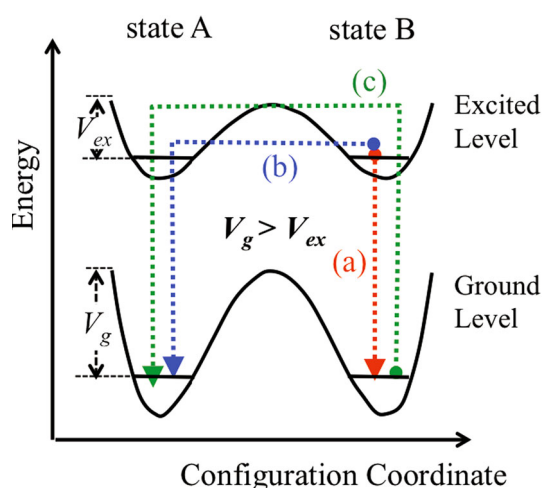


Fig. 2 Potential curves in two-level two-state model

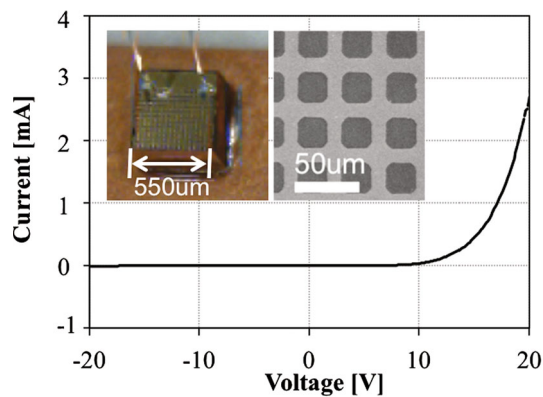


Fig. 3 I - V characteristic and images (*inset*) of fabricated GaP diodes. SEM image (*inset, right*) shows mesh-shaped electrode on surface

electrode. Finally, the positive electrode was connected to the PCB by wire bonding. An image of the completed device and its I - V characteristic are shown in Fig. 3. From this figure, it can be seen that the device has a good rectification characteristic.

Next, we performed DPP-assisted annealing. A forward current (power supply: Keithly, K-2400) was applied to the fabricated device while irradiating it with CW light with a wavelength of 532 nm (2.33 eV) from a DPSS laser, causing the spatial distribution of Zn atoms to change. The substrate temperature was kept constant using a Peltier device. The EL emission spectrum was measured using a grating spectrometer and a cooled Si-CCD (Roper Scientific Inc.).

4 Results and discussion

4.1 Changing the barrier height by applying an external field

First, we derive the height of the barrier that the Zn atoms must get over in order to make a transition, in the presence of two external fields (DC electric field and irradiated light). The net transition rate from state A to state B in the excited level in Fig. 2 is given by [13]

$$\gamma_T \propto \exp\left(-\frac{V_{\text{ex}}}{kT}\right) \quad (1)$$

Here, V_{ex} is the height of the potential barrier in the excited level, k is Boltzmann's constant, and T is temperature. The DC bias voltage used in the experiments was 22 V, and the irradiation light power was 0.2 W (beam diameter, 0.55 mm). During the measurements, a constant current of 25 mA was injected. Figure 4 shows the measured relationship between the EL intensity and the DPP-assisted

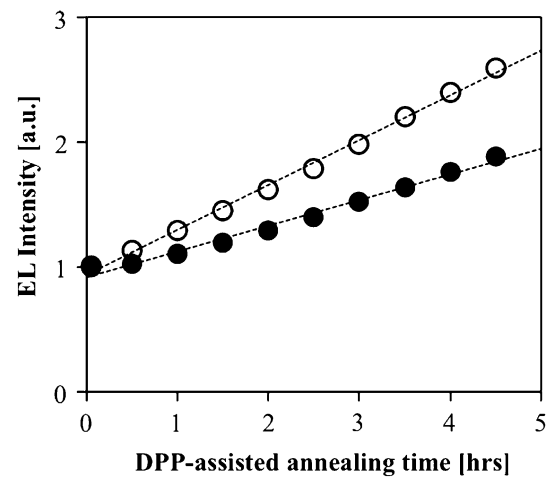


Fig. 4 EL intensity versus DPP-assisted annealing time for different system temperatures

annealing time. The white circles and black circles are the results obtained when the devices were maintained at temperatures of 320 and 310 K, respectively. The broken lines are straight lines obtained by fitting to the measured value. From this figure, we can see that the EL intensity increased as the DPP-assisted annealing time increased and that the rate of increase differed depending on the temperature. The rate of increase is proportional to γ_T in Eq. (1), and therefore, from Eq. (1), the barrier height in the excited level is expressed by

$$V_{\text{ex}} = k \frac{T_1 T_2}{T_1 - T_2} \log \frac{\gamma_{T_1}}{\gamma_{T_2}} \quad (2)$$

By substituting $T_1 = 320$ K and $T_2 = 310$ K, and by substituting the ratio of the gradients of the two straight lines in Fig. 4 for $\gamma_{T_1}/\gamma_{T_2}$, we obtain the value $V_{\text{ex}} = 0.48$ eV.

In the absence of an external field, according to previous research, the height of the barrier that electrons in the Zn atoms must get over to make a transition inside the GaP crystal is 0.61 eV, and the required barrier height obtained when Ga sites are substituted via the kick-out mechanism is 1.64 eV [15]. By comparing these values, we were able to reduce the barrier height to 0.48 eV by using an external field. From this finding, we conclude that the local dopants distribution can be changed by means of DPP-assisted annealing even at room temperature.

4.2 Optimization of DPP-assisted annealing

In a previous study, it was shown that the rate of increase in EL with an energy above E_g is considerably increased by using DPP-assisted annealing [6]. When annealing is performed with only an injection current, without light

irradiation, as explained in Sect. 4.1, the barrier height is reduced by the DC electric field and the Zn atoms can easily diffuse. However, this diffusion is random and is equivalent to thermal diffusion. In contrast, diffusion can be controlled by the irradiation light.

In this subsection, we demonstrate that the spatial distribution of the Zn atoms is controlled by de-excitation and relative cooling due to stimulated emission. First, using the TLTS model, we explain the existence of an optimal ratio of the injection current to the irradiation light power during DPP-assisted annealing. Then, we described experiments performed while varying the current and irradiation light power, to confirm the validity of our hypothesis.

First, it is assumed that the p–n homojunction section is at all of the state B in Fig. 2, in other words, at local structures that are suitable for generating DPPs, and let us consider the state transition that can occur via photons and externally injected electrons.

- (a) (Red arrow in Fig. 2) Since an electron is injected, the system is in the excited level at state B. This electron emits a photon via spontaneous emission or stimulated emission and transitions to the ground level at state B.
- (b) (Blue arrow in Fig. 2) Similarly to case (a), the system is in the excited level. If a photon is not emitted, the lifetime of the excited electron is extended, and the probability of a transition to state A increases. After the state transition to state A, the electron transitions to the ground level at state A via nonradiative relaxation.
- (c) (Green arrow in Fig. 2) The ground level rises to the excited level by absorbing a photon. Considering a case similar to (b), the system subsequently transitions to state A and returns to the ground level at state A via nonradiative relaxation.
- (d) Other. In all other processes, the system transitions from the ground level at state B to the excited level by absorbing a photon and then transitions to the ground level at state B.

Of these four cases, in (a) and (d), the initial state and final state are at state B, and the local structure of the spatial distribution of Zn atoms is maintained; however, in (b) and (c), since the final state is at state A, the local structure changes. Therefore, to maintain a local structure that is suitable for light emission via DPPs, the probabilities of (b) and (c) occurring must be reduced. Noting that, in stimulated emission, a single photon induces stimulated emission of a photon from a single electron, the probability of stimulated emission will be maximum if the injected electrons are irradiated with the same number of photons. In other words, the probability in case (a) will be maximum when the ratio of the number of electrons to the number of

photons is 1. If the number of electrons is increased, and the number of excess electrons that do not contribute to the stimulated emission process increases, the proportion of case (b) must increase. Conversely, if the number of excess photons that do not contribute to the stimulated emission process increases, the proportion of case (c) must increase. In other words, to keep the local structure that is suitable for light emission, the ratio of the number of electrons to the number of photons must be 1.

Next, the above discussion will be applied to DPP-assisted annealing. Before annealing, states A and states B in Fig. 2 both exist. First, since a photon is not emitted at state A, the system in the excited level can only undergo non-radiative relaxation at state A, or transition to state B. In other words, the EL intensity monotonically increases. In the case of nonradiative relaxation, localized heat generation occurs, and therefore, the transition rate becomes higher, according to Eq. (1). At state B on the other hand, the above discussion can be applied. As shown in Fig. 4, since DPP-assisted annealing is a process that is performed for a long time, it is important to allow transitions from state A to state B in Fig. 2; however, it is also important to keep a local structure at which the system have already transitioned to state B.

In summary, it is expected that the EL enhancement effect will be most conspicuous when the ratio of the number of electrons to the number of photons is 1. The value of this ratio is determined by the ratio of the injection current to the irradiation light power, and this was confirmed experimentally. Figure 5a, b shows the results obtained when the irradiation light power during DPP-assisted annealing was 180 and 260 mW, respectively. In both graphs, curves (i) and (ii) represent the results obtained with injection currents of 20 and 30 mA, respectively. The bandgap energy of GaP ($E_g = 2.26$ eV) and the photon energy of the laser light used in annealing ($E_{\text{anneal}} = 2.33$ eV) are shown by broken lines. Here, $R(E)$ means the rate of increase in EL intensity at photon energy E . In Fig. 5a, the values of $R(E > E_g)$ were higher for the injection current of 20 mA than for the injection current of 30 mA. On the other hand, in Fig. 5b, the values of $R(E > E_g)$ were higher for the injection current of 30 mA than for the injection current of 20 mA.

Figure 6 shows measurement results of R ($E_{\text{anneal}} = 2.33$ eV) for various values of injection current and irradiation light power, including also the cases shown in Fig. 5. In this figure, the x-axis is the ratio of the number of photons to the number of electrons, calculated by substituting the irradiation light power and the injection current for the number of photons and the number of electrons, respectively. As is seen from this figure, R is large around a photon-to-electron ratio of 1.3. This value is in good agreement with the ratio obtained from the above

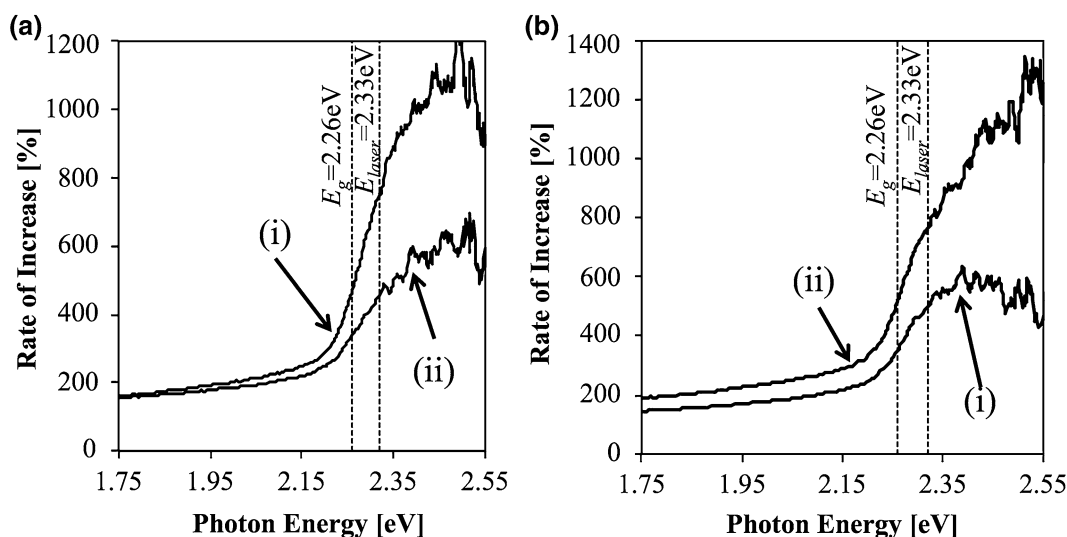


Fig. 5 Change in the rate of increase in EL intensity for different DPP-assisted annealing conditions: (i) current of 20 mA, and (ii) current of 30 mA. **a** Results obtained with laser power of 180 mW. **b** Results obtained with laser power of 260 mW

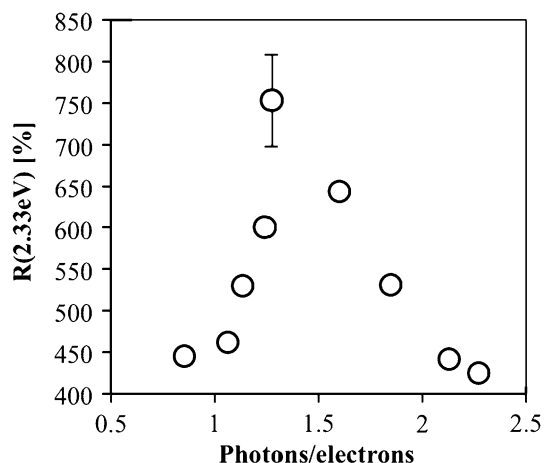


Fig. 6 Rate of increase in EL intensity at photon energy of 2.33 eV, according to current and laser power conditions during DPP-assisted annealing. Ratio on x-axis was calculated by substituting the irradiation light power and the injection current for the number of photons and number of electrons, respectively

discussion, namely 1. The deviation comes from the nonuniform distributions of laser beam and current. The laser we used emits beams that approximate a Gaussian profile on the focal plane, and the current distribution also deviates from a uniform distribution because of the shape of the surface electrode. We have shown that there is an optimum ratio of the injection current to the irradiation light power, which was estimated using the TLTS model in Fig. 2. In addition, when the ratio of the number of injected

electrons to the number of irradiated photons is substituted for this ratio, it was found that the ratio is close to 1.

5 Conclusion

Using a TLTS model, we analyzed the characteristics of an enhancement in EL intensity from a GaP LED due to DPP-assisted annealing. The central idea is that the potential barrier is reduced in the presence of an external field (DC electric field and light irradiation). We confirmed experimentally that, in the excited level, the barrier height was reduced to 0.48 eV. From this finding, we showed that the spatial distribution of Zn atoms can be changed by current injection and light irradiation even at room temperature.

Simply reducing the barrier height does not increase the EL intensity because this merely brings about random diffusion of the Zn atoms. In this research, we showed that a structure that is suitable for light emission via DPPs is formed by means of a transition between a low-barrier excited level and a high-barrier ground level due to stimulated emission and that this structure is maintained. In addition, we found that optimum condition for maximizing the effect of DPP-assisted annealing could be achieved when the ratio of the number of injected electrons to the number of irradiated photons was close to 1, and we confirmed this experimentally.

Acknowledgments This work was partially supported by the Core-to-Core Program of JSPS (A. Advanced Research Network) and a Grant-in-Aid for Scientific Research (B) (No. 24360023) of MEXT.

References

1. T. Takeuchi, H. Takeuchi, S. Sota, H. Sakai, H. Amano, I. Akasaki, *Jpn. J. Appl. Phys. Part-2 Lett.* **36**, L177 (1997)
2. T. Sugahara, M. Hao, T. Wang, D. Nakagawa, Y. Naoi, K. Nishino, S. Sakai, *Jpn. J. Appl. Phys.* **37**, L1195 (1998)
3. B. Hakki, A. Jayaraman, C. Kim, *J. Appl. Phys.* **41**, 5291 (1970)
4. D. Bour, J. Shealy, G. Wicks, W. Schaff, *Appl. Phys. Lett.* **50**, 615 (1987)
5. L.A. Kolodziejski, R.L. Gunshor, A.V. Nurmikko, *Annu. Rev. Mater. Sci.* **25**, 711 (1995)
6. J. H. Kim, T. Kawazoe, M. Ohtsu, *Adv. Opt. Technol.* **2015**, 236014 (2015). doi:[10.1155/2015/236014](https://doi.org/10.1155/2015/236014)
7. R. Logan, H. White, W. Wiegmann, *Solid-State Electron.* **14**, 55 (1971)
8. M. Ohtsu, *Nanophotonics* **1**, 83 (2012)
9. Y. Tanaka, K. Kobayashi, *J. Microsc.* **229**, 228 (2008)
10. T. Kawazoe, M. Mueed, M. Ohtsu, *Appl. Phys. B* **104**, 747 (2011)
11. T. Kawazoe, M. Ohtsu, *Appl. Phys. A-Mater. Sci. Process.* **115**, 127 (2014)
12. R. Jankowiak, R. Richert, H. Bässler, *J. Phys. Chem.* **89**, 4569 (1985)
13. W. Köhler, J. Meiler, J. Friedrich, *Phys. Rev. B* **35**, 4031 (1987)
14. A. Einstein, P. Ehrenfest, *Zeitschrift für Physik A Hadrons Nucl.* **19**, 301 (1923)
15. A. Höglund, C. Castleton, S. Mirbt, *Phys. Rev. B* **77**, 113201 (2008)
16. T. Kawazoe, K. Nishioka, M. Ohtsu, *Appl. Phys. A*, **1** (2015). doi:[10.1007/s00339-015-9288-8](https://doi.org/10.1007/s00339-015-9288-8)

High-speed flattening of crystallized glass substrates by dressed-photon–phonon etching

W. Nomura^{1,4} · T. Yatsui^{1,2} · T. Kawazoe^{1,3} · N. Tate^{1,5} · M. Ohtsu^{1,2,3}

Received: 3 July 2015 / Accepted: 28 August 2015 / Published online: 4 September 2015
© Springer-Verlag Berlin Heidelberg 2015

Abstract Dressed-photon–phonon (DPP) etching is a non-contact flattening technology that realizes ultra-flat surfaces and has been reported to achieve an arithmetic mean surface roughness, R_a , on the order of 0.1 nm in various materials, such as fused silica, plastic films, and GaN crystal. In this study, we successfully flattened the surface of a crystallized glass substrate in several seconds using laser light with a higher power density than that used in previous studies. The target substrate had an initial appearance similar to frosted glass, with an R_a of 92.5 nm. We performed DPP etching under a Cl_2 atmosphere using a CW laser with a wavelength of 532 nm, a power of 8 W, and a spot diameter of 0.2 mm. After 1 s of processing, we obtained a flat surface with an R_a of 5.00 nm. This surface roughness equaled or surpassed that of a substrate flattened by conventional chemical mechanical polishing, with an R_a of 5.77 nm. Through the detailed analysis of atomic force

microscopic images, we found the DPP etching resulted in the smaller standard deviation of the height difference than CMP in the smaller lateral size than 50 nm.

1 Introduction

Surface flattening is a basic, important issue in many industries. Ultra-flat surfaces are essential, especially for optical elements such as mirrors and optical crystals, as well as high-density storage media such as hard disk drives (HDDs) and semiconductor crystal wafers for electronics. The major flattening technology employed for recent industrial products is chemical mechanical polishing (CMP), which produces surfaces with an arithmetic mean surface roughness, R_a , on the order of 1 nm [1]. However, the final flatness achievable using CMP is limited because the target object makes contact with the polishing pad and slurries. On the other hand, there are non-contact flattening technologies that do not use any pads or abrasives. For example, electropolishing of metal surfaces [2, 3] and ion beam etching of diamond [4, 5] have been reported. However, these technologies have some problems, such as the limited number of applicable materials and the difficulty of realizing ultra-flat surfaces with a flatness on the order of 0.1 nm in terms of R_a .

To overcome these problems, a non-contact ultra-flat-flattening technology called dressed-photon–phonon (DPP) etching has been developed [6, 7]. When the target is irradiated with light, dressed photons are generated around nanometric protrusions on the surface. The dressed photons couple with coherent phonons, forming a DPP, which allows certain photochemical reactions by complementing the photon energy [8]. In fact, energy up-conversion is realized via the generation of DPPs. Thus, in the case of a

✉ W. Nomura
nomura@molecular-device.kyushu-u.ac.jp

¹ Department of Electrical Engineering and Information Systems, Graduate School of Engineering, The University of Tokyo, 2-11-16 Yayoi, Bunkyo-ku, Tokyo 113-8656, Japan

² The International Center for Nano Electron and Photon Technology, The University of Tokyo, 2-11-16 Yayoi, Bunkyo-ku, Tokyo 113-8656, Japan

³ Specified Nonprofit Corporation Nanophotonics Engineering Organization, 1-20-10 Sekiguchi, Bunkyo-ku, Tokyo 112-0014, Japan

⁴ Present Address: Education Center for Global Leaders in Molecular Systems for Devices, Kyushu University, 744 Motoooka, Nishi-ku, Fukuoka 819-0395, Japan

⁵ Present Address: Faculty of Information Science and Electrical Engineering, Kyushu University, 744 Motoooka, Nishi-ku, Fukuoka 819-0395, Japan

target sample placed in a reactive gas atmosphere and irradiated with light having a lower photon energy than that of the absorption peak of the gas molecule, the gas is dissociated by the DPPs due to energy up-conversion. The dissociated gas radicals have high reactivity and etch the target surface at areas where the DPPs are generated; in other words, the nanometric protrusions are selectively etched. As a result, the surface is flattened by removing the protrusions, and eventually the generation of DPPs and the associated etching process autonomously stop.

Using DPP etching, ultra-flat surfaces with R_a values on the order of 0.1 nm have been obtained in various materials, such as fused silica [6], GaN wafers [7], and diamond [9]. Furthermore, the flattening of side walls in three-dimensional structures by exploiting the advantages of this non-contact process has also been reported [10].

In previous reports on DPP etching, targets with an initial R_a , in the range of 0.2–20 nm, and uniform compositions were used, and the DPP etching process time was from 1 min to several hours. In this report, to expand the range of applications of DPP etching, we tried to flatten a crystallized glass substrate with a rougher surface and a nonuniform composition. Using a laser with a high power density, the substrate was successfully flattened in several seconds.

2 Experiment

We employed crystallized glass substrates used in commercial 2.5" HDDs as targets in the DPP etching experiment. The substrate consisted of mainly 60–70 % amorphous SiO₂ as the host material, 10–20 % Al₂O₃ microcrystals, and 0–5 % TiO₂ microcrystals. Figure 1 shows a photograph of the initial state of the substrate, which we named Sample A. Sample A had an appearance like frosted glass, due to having been lapped using diamond abrasives. We measured the surface morphology using an atomic force microscope (AFM, L-Trace II, a product of HITACHI High Technologies), as shown in Fig. 1b. The measurement area was 5 μm × 5 μm, with a resolution of 256 × 256 pixels. We found convex structures with a width of about 1 μm and a height of about 500 nm in the whole measurement area. From this AFM image, we calculated the arithmetic mean surface roughness, R_a , to be 92.5 nm. For comparison, we also prepared a sample using the same crystallized glass substrate but polished by CMP instead of diamond abrasives (Sample B). Sample B appeared transparent and specular, as shown in Fig. 1c. The AFM image of Sample B shown in Fig. 1d was taken with the same conditions as those of Sample A. There were many low grains with a width of 100–500 nm and height of about 20 nm over the entire

measured area. The R_a value of Sample B was calculated to be 5.77 nm.

We performed DPP etching on the lapped substrates with the following conditions and settings using the setup shown in Fig. 2. The samples were placed in a vacuum chamber with an optical window. The chamber was filled with Cl₂ gas at a pressure of 200 Pa. We employed a second harmonic of a continuous wave Nd:YAG laser with a wavelength of 532 nm and a power of 8 W (Shanghai Dream Laser, Co., SDL532-15000T). The laser light was introduced into the chamber through the optical window via a 5° tilted prism and was focused with a lens having a focal length of $f = 100$ mm. The beam spot on the sample had a diameter of 0.2 mm and was movable by using the tilted prism mounted on an electrically rotatable holder. The optical power density was calculated to be 2.5×10^4 W/cm², which was 10^3 – 10^4 times higher than that in previous studies on DPP etching [6, 7]. We controlled the irradiation time of the laser by controlling the rotation speed of the prism holder. The samples were named Samples C and D, whose irradiation times were 1 and 5 s, respectively. Samples C and D were prepared with the same lapping process as Sample A, and the initial surface profiles of Samples C and D were similar to that of Sample A.

Figure 3a shows a photomicrograph of the area around the laser spot after DPP etching for 5 s. The left side in Fig. 3a was outside the laser spot, and the right side was the irradiated region. The irradiated region appeared brighter than the non-irradiated region because the light was scattered by the convex structures in the non-irradiated region. AFM images of Samples C and D are shown in Fig. 3b, c, respectively. The measurement conditions and vertical scales of Fig. 3b, c are the same as those in Fig. 1d. To compare the typical surface structures, we took cross-sectional profiles of the AFM images of Samples A–D between the white arrows in Fig. 1b, d, and Fig. 3b, c, as shown by the black, green, red, and blue solid lines in Fig. 3d, respectively. The height of the convex structures with a width of about 1 μm was reduced from about 500 nm in Sample A to about 20 nm in Sample C. Additionally, the convex structures were almost removed in Sample D. However, we found a few protrusions with widths of 50–200 nm and heights of <100 nm in Samples C and D.

3 Discussion

Table 1 represents the R_a and the maximum peak-to-valley vertical intervals, P – V , of the AFM images of Samples A (lapped), B (CMP), C (1 s DPP etching), and D (5 s DPP etching). The R_a value was reduced by DPP etching from

Fig. 1 **a, c** Photographic images of crystallized glass substrates: **a** lapped with diamond abrasives (Sample A) and **c** polished by CMP (Sample B). **b, d** AFM images of Samples A (**b**) and B (**d**), respectively. *White arrows* indicate positions of cross sections shown in Fig. 3d

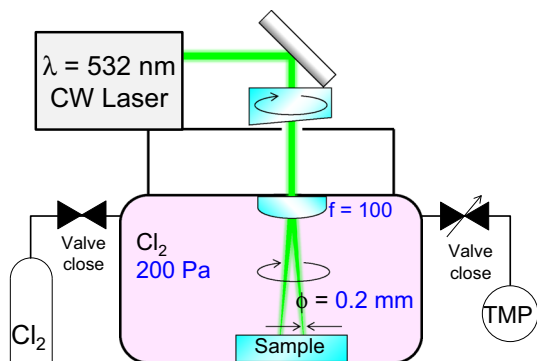
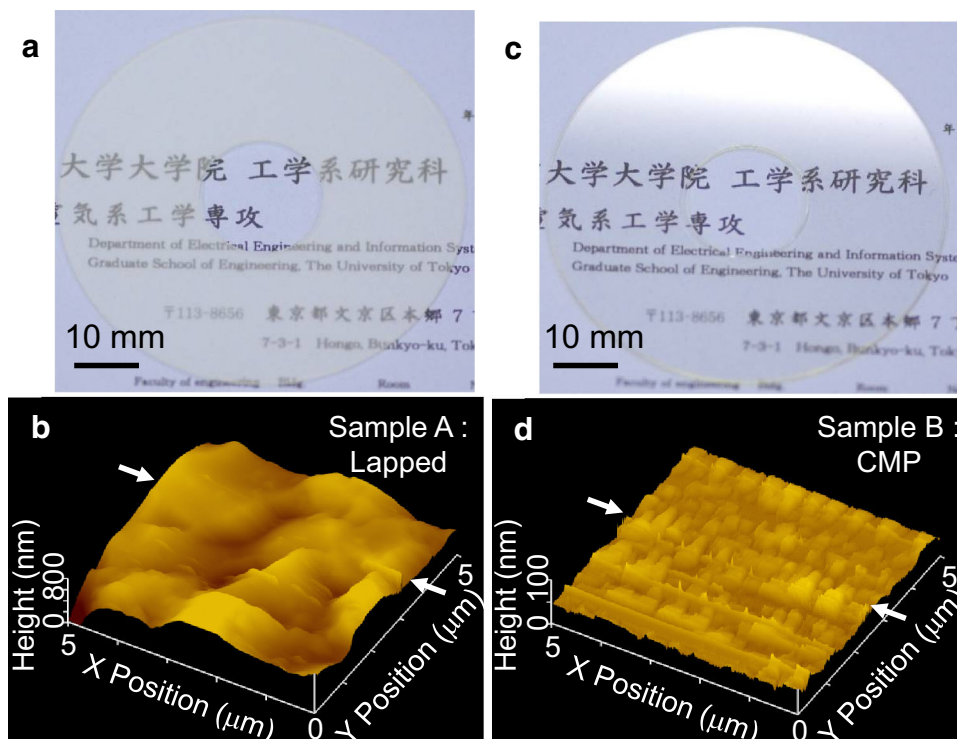


Fig. 2 Schematic diagram of experimental setup for DPP etching

92.5 nm in Sample A to 5.00 nm in Sample C and to 5.20 nm in Sample D, either equaling or surpassing the R_a value of 5.77 nm in Sample B. On the other hand, the P – V values were reduced by DPP etching from 966 nm in Sample A to 112 nm (Sample C: 1 s DPP etching) and 198 nm (Sample D: 5 s DPP etching), which are higher than the value of 83.6 nm in Sample B. Although the DPP etching resulted in the smaller R_a value than CMP, larger P – V values of after DPP etching than CMP are owing to the remaining protrusions in Samples C and D. From these results, utilizing a laser with high power density, we successfully flattened crystallized glass substrates by DPP etching in 1–5 s, from the initial lapped surface to a flatness equal to or better than that achieved by CMP.

As described above, the surface of Sample A consisted of convex structures with a width of about 1 μm and a height of about 500 nm. These structures were too large to generate dressed photons, which we speculate is the reason why those convex structures could not be removed by DPP. We considered that the mechanism by which the surfaces were flattened involved a combination of DPP etching and thermal effects associated with photochemical reactions due to the use of a laser with a high power density.

We performed simple calculations to estimate the amount of heating by using the physical properties of general glass material (thermal conductivity 1.5 W/mK, density 2.5 g/cm³, specific heat 1.2 J/gK, glass-transition temperature about 500 °C, and melting point about 1500 °C) and the dimensions of the sample substrates (thickness 0.635 mm, outer diameter 63.5 mm, and inner diameter 20 mm). First, we measured the absorbance, A , from the difference of the transmittances of a fused silica substrate prepared with CMP and Sample B as $A = 0.10$. The heating rate due to internal absorption in the crystallized glass substrates was calculated to be 0.73 W. Next, considering heat transfer from the laser beam spot to the entire substrate, the amount of heat transferred when the temperature difference between the areas inside and outside the beam spot was 390 °C was calculated to be 0.73 W; in other words, the heating by laser irradiation stops. Then, we estimated the average increase in temperature from the volume of the substrate, the density, and the

Fig. 3 **a** Photomicrographic image of Sample D. *Right* and *left* sides are region irradiated with laser light for 5 s and non-irradiated region, respectively. **b, c** AFM images of Samples C (**b**) and D (**c**), respectively. **d** Cross-sectional profiles of AFM images taken along *white arrows* in Fig. 1b, d, and Fig. 3b, c. *Black, green, red, and blue solid lines* are for Samples A, B, C, and D, respectively

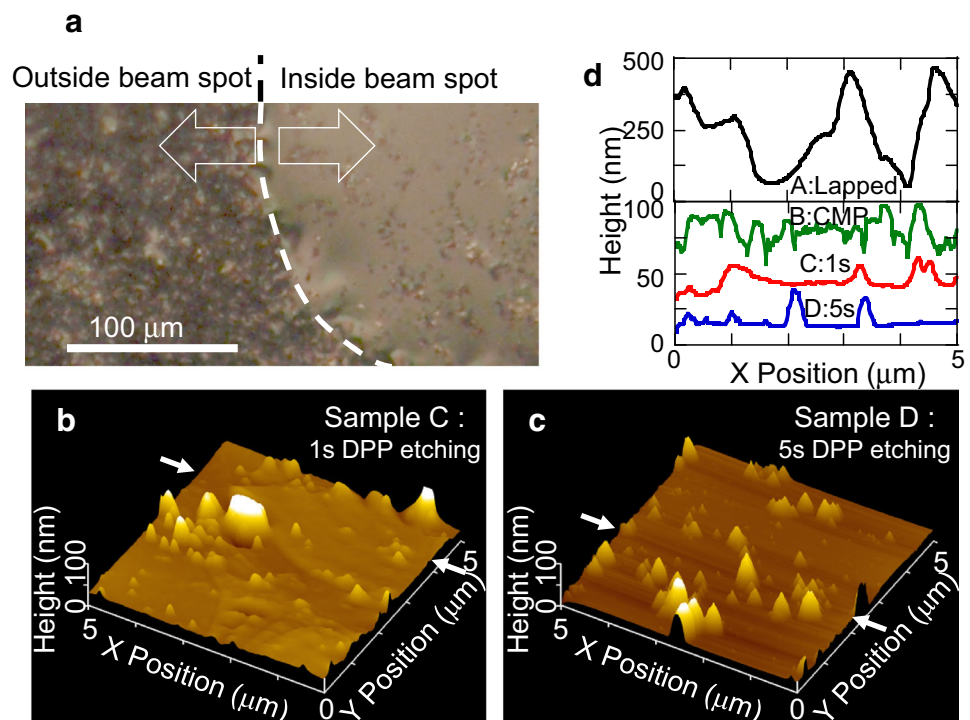


Table 1 Arithmetic mean surface roughness, R_a , and the maximum peak-to-valley vertical interval, $P-V$, calculated from the AFM images of Samples A, B, C, and D

	R_a (nm)	$P-V$ (nm)
A: Lapped	92.5	966
B: CMP	5.77	86.5
C: 1 s DPP etching	5.00	112
D: 5 s DPP etching	5.20	198

specific heat to be 7.2 °C per minute. Since the total laser irradiation time in the experiment was less than 1 min, the temperature at the beam spot did not exceed the glass-transition temperature or melting point. Thus, it seems that the flattening of Sample A was not attributed to heating due to laser irradiation only, but was the result of a combination of DPP etching and thermal effects associated with photochemical reactions.

In order to confirm the contribution of DPP etching, we calculated the standard deviation of the height difference $R(l)$, which indicates the height and frequency of a structure with a lateral size of l , from the AFM images using the method given in Ref. [7]. The black, green, red, and blue solid lines in Fig. 4 represent $R(l)_A$, $R(l)_B$, $R(l)_C$, and $R(l)_D$ calculated from AFM images of Samples A, B, C, and D, respectively. $R(l)_B$, $R(l)_C$, and $R(l)_D$ had varying magnitude relations depending on l , which reflects the trend of each

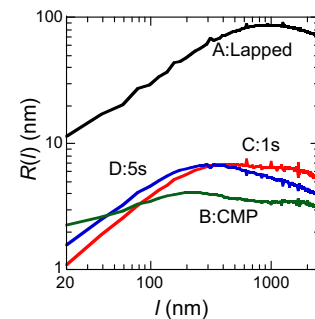


Fig. 4 Standard deviation of the height difference, $R(l)$, calculated from the AFM images. *Black, green, red, and blue solid lines* are those obtained from Samples A, B, C, and D, respectively

sample, and $R(l)_A$ took higher values than the others in the entire range of l , similarly to R_a and $P-V$. In the case of $l \approx 1000$ nm, the magnitude relation was $R(l)_C > R(l)_D > R(l)_B$. The larger value of $R(l)_C$ (1 s DPP etching) than $R(l)_D$ (5 s DPP etching) originates in the convex structures with a width of about 1 μm and a height of about 20 nm which existed in Sample C and was removed in Sample D. In the case of $l \approx 100$ nm, the magnitude relation was $R(l)_D > R(l)_C > R(l)_B$, in which larger values of $R(l)_D$ and $R(l)_C$ (DPP etching) than $R(l)_B$ (CMP) represent the protrusions with widths of 50–200 nm in Samples C and D. On the other hand, in the case of $l < 50$ nm, the magnitude relation was $R(l)_B > R(l)_D > R(l)_C$. This trend agrees well with the typical characteristics of DPP etching, namely that nanometric structures are selectively removed,

and also with the results of previous studies in which a surface prepared by CMP was flattened by DPP etching [6, 7, 9, 10].

Finally, we discuss the surface structures of Samples B, C, and D. The origin of these structures was considered to be the nonuniform composition of the crystallized glass substrates. As described above, the substrates had Al_2O_3 and TiO_2 microcrystals in the host amorphous SiO_2 . However, the possible causes of the surface structures formed differ between CMP and DPP etching. For example, Al_2O_3 has a Vickers hardness about two times higher than that of SiO_2 [11]. Thus, since Sample B was polished by CMP, which is a contact process, the grains with widths of 100–500 nm and heights of about 20 nm were assumed to be produced due to the difference in hardness. In contrast, DPP etching is a non-contact process based on photochemical reactions. The microcrystals in the substrate may have resulted in non-uniform etching because they have various compositions and crystal orientations. For example, the etching selectivity of Al_2O_3 versus SiO_2 for dry etching using Cl_2 gas was reported to be 0.5–0.7 [12, 13], and Al_2O_3 also shows an anisotropic etching rate [14]. In order to estimate the material of the protrusions in Samples C and D, we calculated the area ratio of the protrusions relative to the whole measurement area of AFM, defining areas with heights higher than a threshold height as protrusions. The threshold heights of Samples C and D were set to 47.5 and 32.0 nm, respectively. As a result, the densities were calculated to be 4.34 and 10.0 % in Samples C and D, respectively. These calculated values were in suitable agreement with the experimental results. As written in Sect. 2, the reduction in the height of initial convex structures by DPP etching was not completed in Sample C, in contrast to Sample D. Thus, the density of protrusions in Sample D was higher than that in Sample C, indicating that the protrusions consisted of materials with lower etching rates than those of the others. Moreover, the approximated density of protrusions in Sample D (10 %) and the approximated Al_2O_3 microcrystal content (10–20 %) suggest that the protrusion materials are the microcrystals in the crystallized glass substrate.

4 Conclusion

In this report, we successfully flattened crystallized glass substrates used for HDDs using DPP etching with laser light having a high power density. The surface roughness, R_a , was reduced from 92.5 to 5.00 nm (1 s DPP

etching) and 5.20 nm (5 s DPP etching) when irradiated with CW laser having a wavelength of 532 nm, a power of 8 W, and spot diameter of 0.2 mm under Cl_2 gas with a pressure of 200 Pa. The obtained surface roughness either equaled or surpassed that of a substrate polished by CMP, whose R_a value was 5.77 nm. In addition to the R_a value reduction by DPP etching, from numerical calculations and analysis of AFM images, DPP etching resulted in the selective etching of smaller lateral size than 50 nm.

Owing to the composition of the crystallized glass substrate and the nonuniform etching rate, the substrates after DPP etching had protrusions with widths of 50–200 nm and heights of less than 100 nm. We expect smoother surfaces should be obtained by removing such protrusions, because DPP etching can be applied to various compositions by selecting a suitable light source and reactive gases.

Acknowledgments This research was supported in part by the Ministry of Economy, Trade and Industry (METI). The crystallized glass substrates used in this study were provided by Showa Denko K.K.

References

1. L.M. Cook, J. Non-Cryst. Solids **120**, 152 (1990)
2. W.C. Elmore, J. Appl. Phys. **10**, 724 (1939)
3. S.-J. Lee, Y.-H. Chen, J.-C. Hung, Int. J. Electrochem. Sci. **7**, 12495 (2012)
4. S. Ilias, G. Sené, P. Möller, V. Stambouli, J. Pascallon, D. Bouchier, A. Gicquel, A. Tardieu, E. Anger, M.F. Ravet, Diam. Relat. Mater. **5**, 835 (1996)
5. F. Frost, R. Fehner, B. Ziberi, D. Flamm, A. Schindler, Thin Solid Films **459**, 100 (2004)
6. T. Yatsui, K. Hirata, W. Nomura, Y. Tabata, M. Ohtsu, Appl. Phys. B **93**, 55 (2008)
7. T. Yatsui, W. Nomura, F. Stehlin, O. Soppera, M. Naruse, M. Ohtsu, Beilstein J. Nanotechnol. **4**, 875 (2013)
8. M. Ohtsu, *Dressed Photons* (Springer, Berlin, 2013)
9. T. Yatsui, W. Nomura, M. Naruse, M. Ohtsu, J. Phys. D **45**, 475302 (2012)
10. T. Yatsui, K. Hirata, Y. Tabata, Y. Miyake, Y. Akita, M. Yoshimoto, W. Nomura, T. Kawazoe, M. Naruse, M. Ohtsu, Appl. Phys. B **103**, 527 (2011)
11. F. Gao, J. He, E. Wu, S. Liu, D. Yu, D. Li, S. Zhang, Y. Tian, Phys. Rev. Lett. **91**, 015502 (2003)
12. J.D.B. Bradley, F. Ay, K. Wörhoff, M. Pollnau, Appl. Phys. B **89**, 311 (2007)
13. C.H. Jeong, D.W. Kim, J.W. Bae, Y.J. Sung, J.S. Kwak, Y.J. Park, G.Y. Yeom, Mater. Sci. Eng. B **93**, 60 (2002)
14. Y.P. Hsu, S.J. Chang, Y.K. Su, J.K. Sheu, C.H. Kuo, C.S. Chang, S.C. Shei, Opt. Mater. **27**, 1171 (2005)

Polarization control of an infrared silicon light-emitting diode by dressed photons and analyses of the spatial distribution of doped boron atoms

Tadashi Kawazoe^{1,2} · Katsuhiko Nishioka¹ · Motoichi Ohtsu^{1,2,3}

Received: 18 May 2015 / Accepted: 15 June 2015 / Published online: 25 June 2015
© Springer-Verlag Berlin Heidelberg 2015

Abstract This paper reports the fabrication of a polarization-controlled infrared LED fabricated by dressed-photon–phonon (DPP)-assisted annealing of a bulk Si crystal. For the DPP-assisted annealing, linearly polarized infrared light with a wavelength of 1.342 μm was made normally incident on the top surface of the crystal. The photon energy at the peak of the emitted light spectrum of the fabricated LED was close to that of the light irradiated during the DPP-assisted annealing. A degree of polarization of as large as 0.07 was obtained. The spatial distribution of the doped B atoms in the fabricated LED was measured, and the following findings were obtained: (1) B atoms formed pairs in which the separation between the two B atoms was three times the lattice constant of the Si crystal; and (2) the B atom pairs were apt to orient along the direction perpendicular to the propagation direction and to the polarization direction of the light irradiated during the DPP-assisted annealing. Based on these findings (1) and (2), photon breeding was confirmed with respect to photon energy and spin, respectively.

1 Introduction

Although bulk silicon (Si) crystal has been popularly used for electronic devices, it has not been used for practical light-emitting devices such as light-emitting diodes (LEDs) and lasers. This is because Si is an indirect transition-type semiconductor, meaning that electrons in the conduction band have to change their momenta in order to produce light emission. Here, the problem is that the probability of the interaction between an electron and a phonon, indispensable for the momentum change, is very low.

In order to solve this problem, for example, porous Si [1], a super-lattice structure of Si and SiO₂ [2, 3], and Si nanoprecipitates in SiO₂ [4] have been used to emit visible light. To emit infrared light, Er-doped Si [5] and Si–Ge [6] have been employed. In these examples, the emission efficiency is too low for practical use since Si still works as an indirect transition-type semiconductor in these materials.

To drastically increase efficiency, a novel fabrication method named DPP-assisted annealing has been recently devised by the authors [7]. This method has been used to fabricate an infrared LED whose external quantum efficiency and output power were as high as 15 % and 1 W, respectively, at a wavelength of 1.32 μm (CW operation at room temperature). A visible LED [8], an infrared laser [9, 10], an optical and electrical relaxation oscillator [11], and an infrared photodetector with optical amplification [12] have also been fabricated by this method. Furthermore, visible LEDs have been fabricated by using a bulk silicon carbide (SiC) crystal, even though this material is also an indirect transition-type semiconductor [13].

The dressed photon (DP) is a quasi-particle created as a result of the interaction between a photon and an electron in a nanometric space [14]. Furthermore, the DP excites

✉ Motoichi Ohtsu
ohtsu@ee.t.u-tokyo.ac.jp

¹ Department of Electrical Engineering and Information Systems, Graduate School of Engineering, The University of Tokyo, 2-11-16 Yayoi, Bunkyo-ku, Tokyo 113-8656, Japan

² Specified Nonprofit Corporation Nanophotonics Engineering Organization, 1-20-10, Sekiguchi, Bunkyo-ku, Tokyo 112-0014, Japan

³ International Center for Nano Electron and Photon Technology, Graduate School of Engineering, The University of Tokyo, 2-11-16 Yayoi, Bunkyo-ku, Tokyo 113-8656, Japan

multimode coherent phonons, and they couple to form a novel quasi-particle called a dressed-photon–phonon (DPP), which can be used for device fabrication and operation. The phonons in the DPP contribute to the required momentum change in the electron described above. The Huang–Rhys factor, representing the coupling strength between electrons and optical mode phonons, has been evaluated to be as large as 4.08 for a fabricated silicon LED (Si-LED) [15]. This value is about 10^2 – 10^3 times that in conventional bulk Si crystals, which demonstrates the large interaction probability between the electrons and phonons in this Si-LED. Furthermore, modes of coherent phonons in the DPP have been identified by pump–probe laser spectroscopy [16].

In the case of a conventional LED, it should be pointed out that the photon energy of the emitted light is determined by the bandgap energy E_g of the semiconductor used [17]. In contrast, in the case of the present Si-LED, it is determined by the photon energy $h\nu_{\text{anneal}}$ of the light irradiated during the DPP-assisted annealing. This phenomenon has been called photon breeding [18]. In other words, the photon energy of the emitted light is identical to $h\nu_{\text{anneal}}$, because the difference between $h\nu_{\text{anneal}}$ and E_g is compensated for by the energy of the phonons in the created DPP. Therefore, even infrared light, whose photon energy is lower than E_g , can be emitted from the Si-LED based on photon breeding. Photon breeding has been confirmed also in a visible Si-LED [8] and a visible SiC-LED [13], which have been fabricated via DPP-assisted annealing by irradiating bulk Si and SiC crystals with visible light, respectively. The magnitudes of the phonon sidebands in the output light spectrum have been controlled by irradiating pairs of light pulses during the DPP-assisted annealing [19].

It is expected that photon breeding takes place not only with respect to photon energy described above but also with respect to photon spin. That is, the light emitted from the LED can be polarized if it is fabricated by irradiating the Si crystal with polarized light during the DPP-assisted annealing.

The output light from conventional LEDs is not polarized, and several methods have been proposed for polarizing it, such as using the specific anisotropic optical properties of nonpolar GaInN quantum wells [20] and installing a complicated subwavelength-size metallic nanograting [21]. Instead of these approaches, the present paper proposes a novel polarization control method for infrared Si-LEDs based on photon breeding with respect to photon spin. It also reports the results of high-spatial-resolution three-dimensional analyses of the spatial distribution of the doped B atoms, performed in order to confirm the photon breeding.

Radiation energy dissipation from relativistic jets in blazars has also been called photon breeding [22]. In this

astrophysical phenomenon, very high-energy X rays are generated from low-energy infrared or visible light by inverse Compton scattering with a charged particle. Therefore, the photon breeding discussed in the present paper, creating photons by using a DPP in a nanometric-sized space in a material, is fundamentally different from that in astrophysics. Due to this difference, the present photon breeding may have to be called “nano-photon breeding” in order to avoid confusion. However, this paper uses the name “photon breeding” for conciseness.

2 Fabrication and operation

The structure of the fabricated Si-LED is schematically shown in Fig. 1a. The fabrication method was equivalent to that in Ref. [7], except that linearly polarized light was irradiated during the DPP-assisted annealing.

2.1 Fabrication by DPP-assisted annealing

First, to form the p–n homojunction, an As-doped n-type Si crystal with a thickness of $625\ \mu\text{m}$, whose electrical resistivity was $10\ \Omega\ \text{cm}$, was used. The top surface of the Si crystal was a (001) plane. The upper part of this crystal

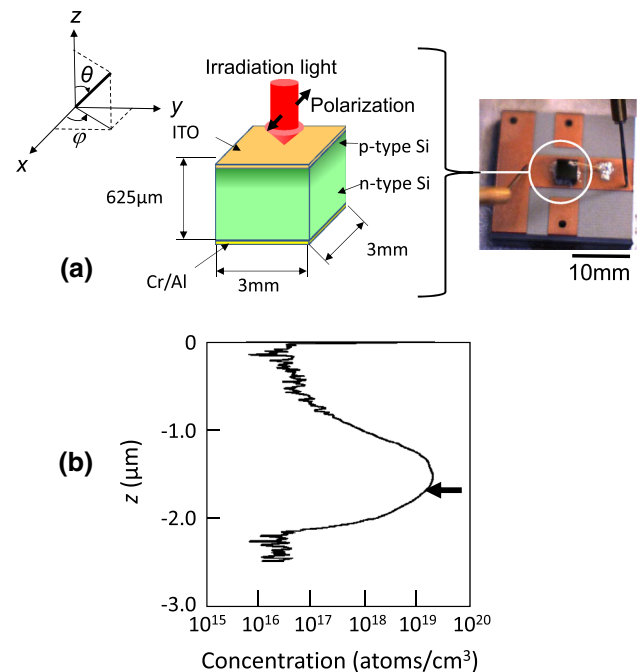


Fig. 1 Structure of the Si-LED. **a** A bird’s-eye view and photograph of the device. Definitions of the Cartesian coordinates (x , y , z), the zenith angle θ , and the azimuthal angle φ are also given. **b** Cross-sectional profile of the doped B atom concentration along the z -axis, measured by secondary ion mass spectroscopy. The *thick arrow* represents the area of the measurement, to be presented in Fig. 3

was further doped with B by ion implantation to form a p-type layer. The implantation direction was the $[00\bar{1}]$ orientation (along the z -axis in Fig. 1a, normal to the (001) plane), and the energy was 700 keV, which realized a doped B atom concentration of 10^{19} cm^{-3} , corresponding to 0.04 % of the Si atom concentration. Figure 1b shows the cross-sectional profile of this concentration along the z -axis, measured by secondary ion mass spectroscopy, which represents the p–n homojunction at a position 1.5–2.0 μm down from the top surface of the Si crystal. An ITO film (150 nm thick) was deposited on the top surface of the Si crystal. Cr and Al films were subsequently deposited on the bottom surface (5 and 100 nm thick, respectively). They were used as an anode and cathode, respectively. After depositing these films, the Si crystal was diced to form a device with an areal size of $3 \text{ mm} \times 3 \text{ mm}$.

Second, for the DPP-assisted annealing, a forward bias voltage was applied to inject the current (170 mA: current density of 1.89 A cm^{-2}) in order to generate Joule energy, causing the B to be diffused by the Joule-heat and varying the spatial distribution of its concentration. During the annealing, infrared light, linearly polarized along the x -axis in Fig. 1a, was normally incident on the top surface of the Si crystal, through the ITO anode. Its power density, photon energy $h\nu_{\text{anneal}}$, and wavelength were 3.3 W cm^{-2} , 0.924 eV, and 1.342 μm , respectively.

Since the photon energy $h\nu_{\text{anneal}}$ of this light is lower than E_g (=1.12 eV), it can propagate through the Si crystal without suffering absorption, creating a DPP on the surface of the B atom at the p–n homojunction. The electron in the conduction band at the p–n homojunction interacts with this DPP to exchange momentum with the phonons in the DPP, and, as a result, a photon is created by stimulated emission. The created photon propagates to outside the Si crystal, which means that a part of the Joule energy is transformed to the propagating photon energy and is dissipated from the Si crystal. This dissipation decreases the diffusion rate of the B atoms, affecting the variation of the spatial distribution of B atoms. The fabrication is finished when this distribution reaches a stationary state.

2.2 Operation based on photon breeding

For the operation of the fabricated S-LED, the infrared light irradiation is not required any more; it is used only during the DPP-assisted annealing. Only forward current injection is required, as is the case of the conventional LED operation. By this forward current, an electron is injected into the conduction band at the p–n homojunction and creates a photon by spontaneous emission even though its probability is very low. However, once this photon is

created, it subsequently creates a DPP on the surface of the B atom at the p–n homojunction, and this DPP interacts with another electron in the conduction band to exchange momentum so that a secondary photon is created. By repeating these momentum exchange and photon creation processes, the emitted light intensity is amplified and reaches a stationary value within a short duration, so that light with a sufficiently high intensity is emitted from the p–n homojunction. It should be noted that the photon energy of the emitted light is identical to $h\nu_{\text{anneal}}$. This is because the spatial distribution of the B atoms has been controlled by the light irradiated during the DPP-assisted annealing, enabling most efficient stimulated emission and spontaneous emission of photons with identical photon energy. In other words, the light irradiated during the DPP-assisted annealing serves as a “breeder” that creates photons with an energy equivalent to $h\nu_{\text{anneal}}$. This is the reason why this novel phenomenon is named photon breeding with respect to photon energy.

For evaluating the polarization characteristics of the fabricated Si-LED, the emitted light was decomposed into two linearly polarized components by using a linear polarizer, and their intensities (I_{\parallel} , I_{\perp}) were acquired. The polarization directions of these components are, respectively, parallel and perpendicular to that of the light irradiated during the DPP-assisted annealing.

Their light emission spectra at an injection current of 100 mA are represented by the curves A and B in Fig. 2a, whose spectral peaks are close to $h\nu_{\text{anneal}}$ due to the photon breeding with respect to photon energy. It is seen that I_{\parallel} is larger than I_{\perp} in a wide spectral range around $h\nu_{\text{anneal}}$. Since the linearly polarized light is the superposition of the two photons with up- and down-spins, this difference between I_{\parallel} and I_{\perp} in this figure also represents the successful results of polarization control, which is due to photon breeding with respect to photon spin.

The black squares in Fig. 2b represent the measured relation between the DPP-assisted annealing time and the degree of polarization $P = (I_{\parallel} - I_{\perp}) / (I_{\parallel} + I_{\perp})$ at the photon energy $h\nu_{\text{anneal}}$. The value of P in this figure is zero at zero annealing time because the Si crystal is optically isotropic. However, this value increases with increasing annealing time and asymptotically approaches a maximum value of 0.07. This increase is not due to the optical anisotropy induced by the Joule-heat because the applied Joule energy was too low to strain or deform the Si crystal. For reference, the surface temperature was maintained at as low as 154 °C in the DPP-assisted annealing (Fig. 2 in Ref. [7]).

The measured values were fitted by the solid curve in Fig. 2b. This curve represents the result of numerical calculation based on the two-level system model, which is a theoretical model popularly used for the light-induced

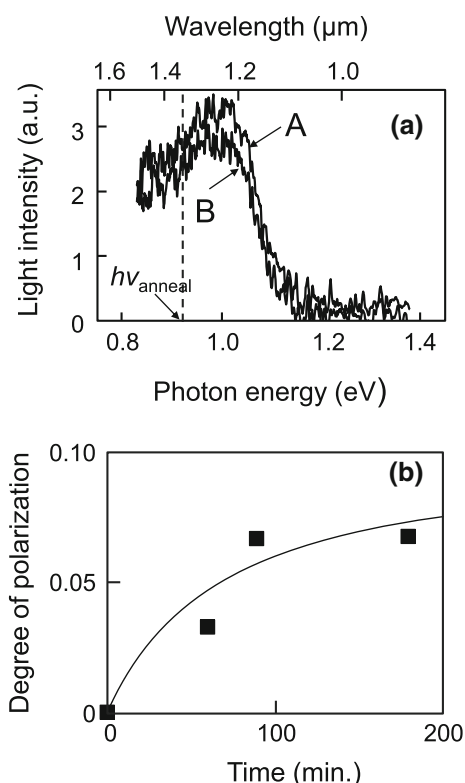


Fig. 2 Characteristics of the light emitted from the fabricated Si-LED. **a** The light emission spectra. Curves *A* and *B* are the linearly polarized components, which are, respectively, parallel and perpendicular to the direction of the linear polarization of the light irradiated during the DPP-assisted annealing. The annealing time was 180 min. **b** Relation between the DPP-assisted annealing time and the degree of polarization P at the photon energy, $h\nu_{\text{anneal}}$. *Black squares* represent the measured values. The *solid curve* represents the theoretical values, which were fitted to the measured values

variations of the configuration coordinates in several phenomena, such as spectral hole burning [23]. The agreement between this curve and the measured values suggests that the polarization was controlled by the linearly polarized light irradiated during the DPP-assisted annealing.

3 Analyses of the spatial distribution of boron atoms

To confirm the hypothesis given at the end of Sect. 2.2, this section presents the analysis results of the three-dimensional spatial distribution of the doped B atoms, which was measured by atom-probe field ion microscopy with sub-nanometer resolution [24]. The measured area is represented by a thick arrow in Fig. 1b. Figure 3 shows the measured three-dimensional spatial distribution of B atoms at the p–n homojunction. The black dots represent the positions of the individual B atoms. The distribution is projected onto the xy -, yz -, and zx -planes ((001), (100), and

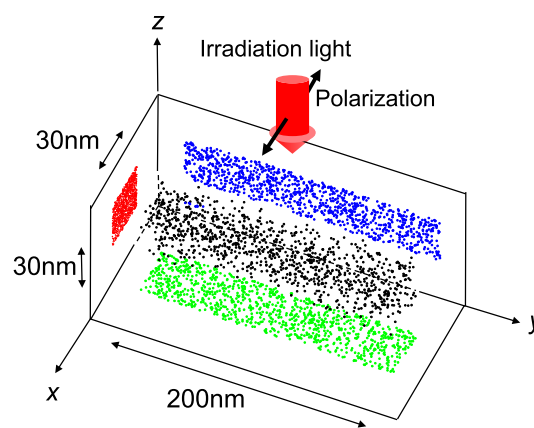


Fig. 3 Three-dimensional spatial distribution of B atoms, measured by the atom-probe ion microscopy

(010) planes), represented by green, blue, and red dots, respectively.

It should be noted that the Si crystal is composed of multiple cubic lattices with a lattice constant a of 0.54 nm [25], and its top surface lies in the xy -plane. The light irradiated during the DPP-assisted annealing is normally incident on this plane; i.e., the light propagation direction is parallel to the z -axis, which is parallel to the [001] orientation.

3.1 Separation between the boron atoms in the pair

Some of the regularly arranged Si atoms are replaced by the doped B atoms in the DPP-assisted annealing. It has been pointed out that phonons can be localized at the B atoms for creating a DPP under light irradiation because the B atoms are lighter than the Si atoms. However, for this localization, it has also been pointed out that two or more adjacent B atoms (in other words, two or more unit cells containing B atoms) are required [26]. Since the doped B atom concentration is as low as 0.04 % relative to the Si atom concentration, making it difficult for more than three B atoms to aggregate, the following discussion considers two closely spaced adjacent B atoms (a B atom pair), around which a phonon is localized for creating a DPP. That is, the pair of unit cells containing the B atoms serves as a phonon localization center.

Figure 4a, b shows the numbers of B atom pairs plotted as a function of the separation, d , between the B atoms in the pair, which were derived from the measurement results in Fig. 3. Since the distribution of the number of B atom pairs is nearly random, it can be least-squares-fitted by the Weibull distribution function (the solid curve in these figures), which is expressed as

$$p(d) = (3/\beta) \cdot (d/\beta)^2 \cdot \exp\left[-(d/\beta)^3\right], \quad (1)$$

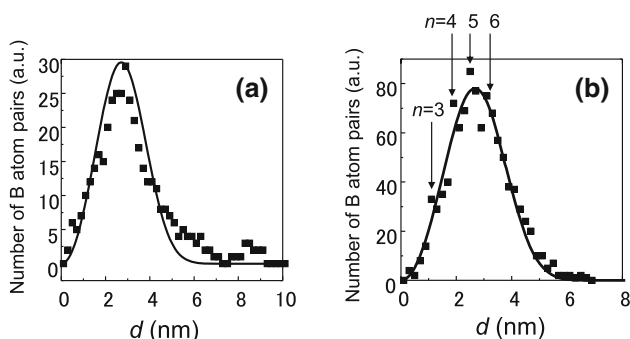


Fig. 4 Number of B atom pairs plotted as a function of the separation d between the B atoms in the pair. **a** The un-annealed Si crystal. **b** The DPP-assisted-annealed Si crystal

where δ is the concentration of the B atoms, and $\beta = \sqrt[3]{3/4\pi\delta}$. In the un-annealed Si crystal (Fig. 4a), the measured number of B atom pairs deviates from the solid curve in the range $d > 45$ nm. The deviation depends on the characteristics of the ion implantation.

In contrast, in the Si crystal after the DPP-assisted annealing (Fig. 4b), the deviation is much less than that in Fig. 4a, which means that the DPP-assisted annealing modified the spatial distribution and decreased the deviation induced by the ion implantation, making the distribution more random. However, at specific values of $d (=na$, where $n = 3, 4, 5, 6$; refer to the four downward arrows in this figure), the number of B atom pairs still deviates from the solid curve and is larger than that of the solid curve. This is explained as follows: The B atom pair with the shortest d (i.e., equal to the lattice constant a) can orient in a direction parallel to the $[1,0,0]$, $[0,1,0]$, or $[0,0,1]$ orientation because the Si crystal is composed of multiple cubic lattices. As a result, the wave-vector (momentum) of the localized phonon points in this direction, which corresponds to the $\Gamma - X$ direction in reciprocal space (Fig. 5). Thus, a photon is efficiently created because this $\Gamma - X$ direction is the same as the direction of the wave-vector of the phonon required for recombination between an electron at the bottom of the conduction band at the X -point and a hole at the top of the valence band at the Γ -point. Here, it should be noted that the absolute value of the wave-vector of the phonon has to be $1/a$ for this electron-hole recombination to take place. Furthermore, it should also be noted that, among the phonons localized at the B atom pair with separation $d (=na)$, the absolute value of the wave-vector of the lowest mode is $1/na$. By comparing these two absolute values, it is found that the DPP at this B atom pair has to create n phonons for recombination. Thus, it can be concluded that the four downward arrows in Fig. 4b indicate selective increases in the number of B atom pairs with separation $d = na$ due to the DPP-assisted annealing, and these pairs serve as localization centers for the phonons.

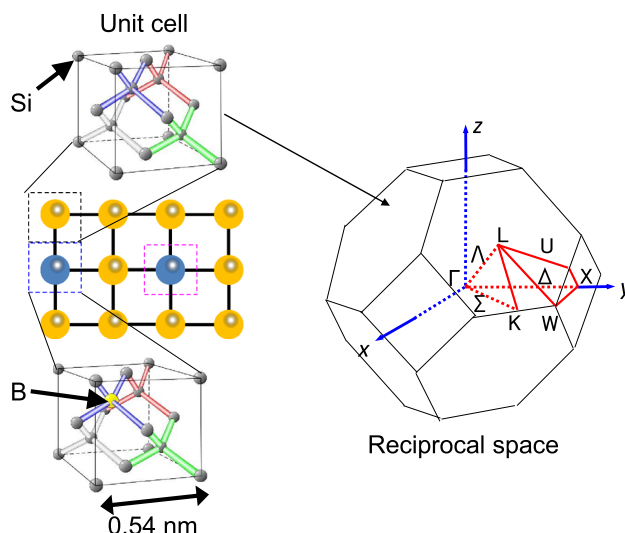


Fig. 5 Unit cell of the Si crystal in real space and in reciprocal space

Figure 6a shows the relation between n and the measured deviation in Fig. 4b. This figure shows that the deviation takes the maximum value at $n = 3$, which means that B atom pairs most efficiently create three phonons for

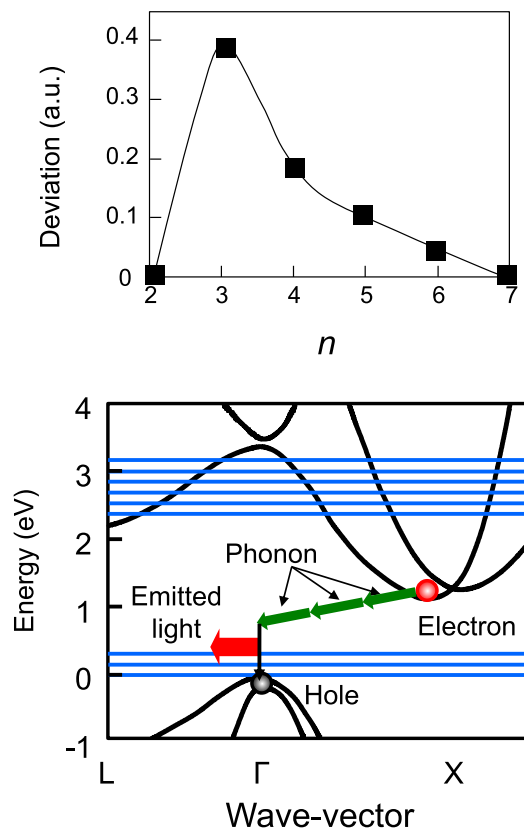


Fig. 6 Relation between n and the deviation. **a** Measured results. **b** The energy band diagram of Si and schematic explanation of light emission

light emission, as is schematically shown in Fig. 6b. This phonon creation process is consistent with the discussion in Ref. [15], in which the magnitudes of the phonon sidebands in the light emission spectra were analyzed based on the density of states of phonons and the estimated value of the Huang–Rhys factor. As a result, the emitted photon energy $h\nu_{\text{em}}$ is expressed as $h\nu_{\text{em}} = E_g - 3E_{\text{phonon}}$. By substituting the values of E_g ($=1.12$ eV) and the relevant optical mode phonon energy E_{phonon} ($=65$ meV [27]) into this equation, the value of $h\nu_{\text{em}}$ is derived to be 0.925 eV, which is identical to the photon energy $h\nu_{\text{anneal}}$ irradiated during the DPP-assisted annealing. This numerical relation confirms that photon breeding with respect to photon energy occurs.

3.2 Dependence on the zenith and azimuthal angles

Figure 4b indicates selective increases in the number of B atom pairs with separation $d = na$. This means that, since n is an integer, B atom pairs are apt to orient along a plane perpendicular or parallel to the top surface of the Si crystal (zenith angle $\theta = 0^\circ$ or 90° in Fig. 1a). Orientation along other directions in which n is not an integer ($\theta \neq 0^\circ, 90^\circ$) hardly occurs.

Figure 7a shows the relation between the zenith angle θ and the number of B atom pairs. It can be seen that this number takes the maximum value at $\theta = 90^\circ$, which means that the B atom pairs are apt to stretch in a plane (xy -plane) which is parallel to the top surface of the Si crystal, i.e., perpendicular to the propagation direction ($[00\bar{1}]$ orientation; z -axis) of the light irradiated during the DPP-assisted annealing. On the other hand, the number of B atom pairs takes the minimum value at $\theta = 0^\circ$, which means that the B atom pairs hardly orient along the propagation direction (z -axis) of the light irradiated during the DPP-assisted annealing. This is because the phonons are hardly localized along this direction since their momenta (wave-vectors) are parallel to $\theta = 90^\circ$ [28].

Figure 7b shows the relation between the azimuthal angle φ and the number of the B atom pairs. This angle is defined in the xy -plane ($\theta = 90^\circ$), and $\varphi = 0^\circ$ corresponds to the polarization direction (x -axis) of the light irradiated during the annealing. The vertical axis in Fig. 7b represents the difference in the numbers of B atom pairs after and before the DPP-assisted annealing. The negative value of this difference at $\varphi = 0^\circ$ means that the number of B atom pairs orienting to $\varphi = 0^\circ$ decreases as a result of the DPP-assisted annealing. In the region $\varphi > 45^\circ$, this difference becomes a positive value, which means that the number increased due to the DPP-assisted annealing. The number of B atom pairs takes the maximum value at $\varphi = 90^\circ$. This angular dependence means that the diffusion of the B atoms was controlled by the linearly polarized light

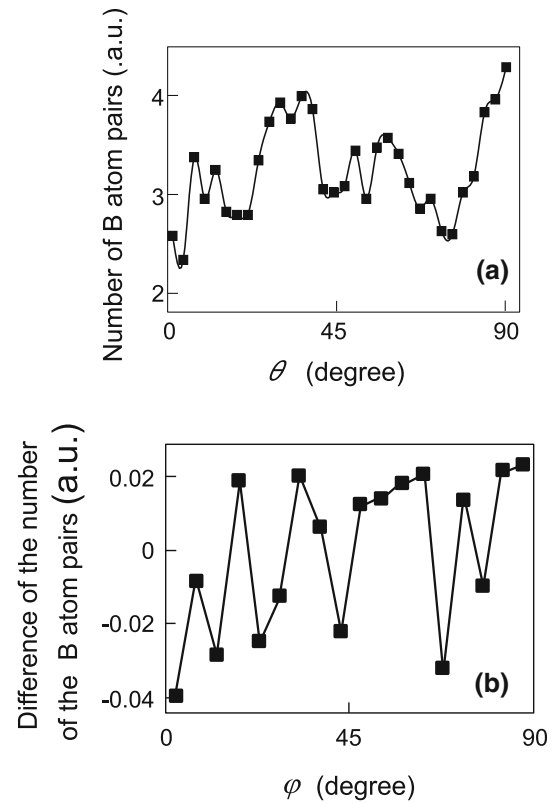


Fig. 7 Relation between the orientation angle and the number of B atom pairs. **a** Relation between the zenith angle θ and the number of B atom pairs. **b** Relation between the azimuthal angle φ and the difference in the numbers of B atom pairs after and before the DPP-assisted annealing

irradiated during the DPP-assisted annealing, with the result that the B atom pairs oriented to $\varphi = 90^\circ$.

As a result, the light emitted from the fabricated LED was polarized, and the polarization direction was governed by that of the light irradiated during the DPP-assisted annealing. There are two possible origins of this induced polarization of the emitted light: (1) Since the oriented B atom pairs work as a kind of nano-wire grid in the xy -plane (the orientation of this grid is $\varphi = 90^\circ$), the light emitted from the fabricated LED can be linearly polarized in the direction ($\varphi = 0^\circ$) perpendicular to the direction of the grid. (2) First, when the LED is fabricated by the DPP-assisted annealing, transverse optical phonons are created at the B atom pairs and couple with the DPs. The vibration direction of these phonons is parallel to that of the electric field of the polarized light ($\varphi = 0^\circ$) irradiated during the DPP-assisted annealing. Next, when the fabricated LED is operated, since these phonons are created again, the direction of the electric field vector of the emitted light becomes also parallel to the vibration direction of these phonons. Therefore, the polarization direction of the

emitted light becomes identical to that of the light irradiated during the DPP-assisted annealing.

The number of B atom pairs at $\varphi \geq 45^\circ$ in Fig. 7b is 8.6 % of the total, which corresponds to a P value of 0.07 for the 180-min annealing time. This correspondence supports the origins (1) and (2) presented above. It should be possible to increase P further by more precisely controlling the annealing parameters for orienting more B atom pairs along the direction $\varphi = 90^\circ$ (and also $\theta = 90^\circ$).

4 Summary

This paper reported the fabrication of an infrared LED by using DPP-assisted annealing of a bulk Si crystal and evaluation of its light emission characteristics. For the DPP-assisted annealing, linearly polarized infrared light with a wavelength of 1.342 μm was made normally incident on the top surface of the bulk Si crystal in order to control the polarization of the light emitted from the fabricated LED. As a result, the photon energy at the peak of the emitted light spectra of the fabricated LED was close to that of the light irradiated during the DPP-assisted annealing. A degree of polarization of as large as 0.07 was obtained.

In order to confirm the photon breeding involved in this polarization control, the spatial distribution of the doped B atoms was measured. The following findings were obtained: (1) B atoms formed a pair, in which the separation between the two B atoms was three times the lattice constant of the Si crystal. This separation is the origin of the photon breeding with respect to photon energy. (2) The B atom pairs are apt to orient in the direction $\theta = 90^\circ$ and $\varphi = 90^\circ$. The former and the latter are the values of the zenith and azimuthal angles, which are perpendicular to the propagation direction and the polarization direction of the light irradiated during the DPP-assisted annealing, respectively. These orientations are the origin of the photon breeding with respect to photon spin.

For reference, the polarization of the output light from a visible SiC-LED has also been controlled by the method devised in the present work, and a value of P as high as 0.12 was obtained at a wavelength of 480 nm [29]. Such polarization control of visible LEDs could be advantageous for reducing power consumption in backlight systems for displays and imaging applications.

Acknowledgments This work was partially supported by the Core-to-Core Program of JSPS (A. Advanced Research Network), a Grant-

in-Aid for Scientific Research (B) (No. 24360023) of MEXT, and the Exploratory Research program (No.15K13374) of MEXT.

References

1. K.D. Hirschman, L. Tysbekov, S.P. Dutttagupta, P.M. Fauchet, *Nature* **384**, 338 (1996)
2. Z.H. Lu, D.J. Lockwood, J.-M. Baribeau, *Nature* **378**, 258 (1995)
3. L. Dal Negro, R. Li, J. Warga, S.N. Beasu, *Appl. Phys. Lett.* **92**, 181105 (2008)
4. T. Komoda, *Nucl. Instrum. Methods Phys. Res. SectB Beam Interact. Mater. Atoms* **96**, 387 (1995)
5. S. Yerci, R. Li, L. Dal, Negro. *Appl. Phys. Lett.* **97**, 081109 (2010)
6. S.K. Ray, S. Das, R.K. Singha, S. Manna, A. Dhar, *Nanoscale Res. Lett.* **6**, 224 (2011)
7. T. Kawazoe, M.A. Mueed, M. Ohtsu, *Appl. Phys. B* **104**, 747 (2011)
8. M.A. Tran, T. Kawazoe, M. Ohtsu, *Appl. Phys. A* **115**, 105 (2014)
9. T. Kawazoe, M. Ohtsu, K. Akahane, N. Yamamoto, *Appl. Phys. B* **107**, 659 (2012)
10. H. Tanaka, T. Kawazoe, M. Ohtsu, K. Akahane, *Fluoresc. Mater.* **1**, 1 (2015)
11. N. Wada, T. Kawazoe, M. Ohtsu, *Appl. Phys. B* **108**, 25 (2012)
12. H. Tanaka, T. Kawazoe, M. Ohtsu, *Appl. Phys. B* **108**, 51 (2012)
13. T. Kawazoe, M. Ohtsu, *Appl. Phys. A* **115**, 127 (2014)
14. M. Ohtsu, *Dressed Photon* (Springer, Dordrecht, 2013), pp. 11–18
15. M. Yamaguchi, T. Kawazoe, M. Ohtsu, *Appl. Phys. A* **115**, 119 (2014)
16. N. Wada, M.-A. Tran, T. Kawazoe, M. Ohtsu, *Appl. Phys. A* **115**, 113 (2014)
17. P.Y. Yu, M. Cardona, *Fundamentals of Semiconductors*, 4th edn. (Springer, Dordrecht, 2010), pp. 345–426
18. M. Ohtsu, *Progress in Nanophotonics I*, ed. by M. Ohtsu (Springer, Dordrecht, 2011), pp.8–11
19. T. Kawazoe, N. Wada, M. Ohtsu, *Adv. Opt. Technol.* (2014) Article IC 958327, doi:10.1155/2014/958327
20. M.F. Schubert, S. Chhajed, J.K. Kim, E.F. Schubert, *Appl. Phys. Lett.* **91**, 051117 (2007)
21. L. Zhang, J.H. Teng, S.J. Chua, E.A. Fitzgerald, *Appl. Phys. Lett.* **95**, 261110 (2009)
22. B.E. Stern, J. Poutanen, *Mon. Not. R. Astron. Soc.* **383**, 1695 (2008)
23. R. Jankowiak, R. Richert, H. Bässler, *J. Phys. Chem.* **89**, 4569 (1985)
24. K. Hono, *Prog. Mater. Sci.* **47**, 621 (2001)
25. K. Godwod, R. Kowalczyk, Z. Szmied, *Phys. Status. Solidi (a)* **21**, 227 (1974)
26. Y. Tanaka, K. Kobayashi, *Phys. E* **40**, 297 (2007)
27. E. Anastassakis, A. Pinczuk, E. Burstein, F.H. Pollak, M. Cardona, *Solid State Commun.* **8**, 133 (1970)
28. Y. Shinohara, T. Otobe, J. Iwata, K. Yanaba, *J. Phys. Soc. Jpn.* **67**, 685 (2012)
29. T. Kawazoe, K. Nishioka, M. Ohtsu, *Abstract of the 21st International Display Workshops*, (Soc. Information Display, 2014) PRJ-1 (Niigata, Japan, 3–5 Dec 2014)

[II] PRESENTATIONS IN INTERNATIONAL CONFERENCES



Mathematical quantum field theory and related topics

Date : 6 /June/2016 - 8/June/2016

Place : West 1 building D-413, IMI Kyushu University, Fukuoka, Japan

http://www.imi.kyushu-u.ac.jp/pages/joint_research_auditorium.html

Monday 6 June

10 : 00-10 : 50 Tadahiro Miyao (Hokkaido)

Long-range charge order in the two-dimensional ionic Hubbard model

11 : 00-11 : 50 Asao Arai (Hokkaido)

Inequivalence of quantum Dirac fields of different masses and a general structure behind it

13 : 30-14 : 20 Daniel Braak (Augsburg)

Integrable and non-integrable models in quantum optics

14 : 30-15 : 20 Motoichi Ohtsu (Tokyo, emeritus)

Dressed Photons

---Concepts of off-shell photon and applications to light-matter fusion technology---

16 : 00-16 : 50 Masato Wakayama (Kyushu IMI)

Representation theoretic approach to the spectrum of quantum Rabi or its generalized models

17 : 00-17 : 50 Marco Falconi (Rome)

Borh's correspondence principle in the Nelson model

Tuesday 7 June

10 : 00-10 : 50 Tomohiro Kanda (Kyushu)

A KMS state on the resolvent CCR algebra

11 : 00-11 : 50 Fumio Hiroshima (Kyushu)

Semi-relativistic QED

13 : 30-14 : 20 Oliver Matte (Aarhus)

Differentiability properties of stochastic flows in non-relativistic QED

14 : 30-15 : 20 Zied Ammari (Rennes)

On the relationship between non-linear Schroedinger dynamics,
Gross-Pitaevskii hierarchy and Liouville's equation

Motoichi Ohtsu

Title:

Dressed Photons ---Concepts of off-shell photon and applications to light-matter fusion technology---

Abstract:

This presentation reviews recent progress in dressed photon technology. After a discussion of the concepts of dressed photons based on the off-shell photon picture, some applications are reviewed, including novel optical functional devices, nano-fabrication technologies, energy conversion technologies, and information processing systems. Novel mathematical scientific models are also presented, as well as an outlook for the future, hinting at the possibilities of dressed photon technology.

Speckle reduction by using transmissive ZnO device based on dressed-photon–assisted optical modulation

Naoya Tate, Tadashi Kawazoe*, Shunsuke Nakashima, Wataru Nomura, Motoichi Ohtsu^{*,**}

Kyushu Univ., 744 Motoooka Nishi-ku, Fukuoka 819-0395, Japan

* Research Institute of Nanophotonics, 1-20-10 Sekiguchi, Bunkyo-ku, Tokyo 112-0014, Japan

** The Univ. Tokyo, 2-11-16 Yayoi, Bunkyo-ku, Tokyo 113-8656, Japan

Keywords: nanophotonics, dressed-photon, optical modulator, laser speckle, speckle reduction

ABSTRACT

We demonstrated large optical modulation using zinc oxide single crystal doped with nitrogen ions, which was annealed by a dressed-photon–assisted annealing method. The device, having a thin, transmissive structure, was used as a key component of a novel speckle reduction method.

1. INTRODUCTION

Oxide semiconductors, which have a large bandgap, are one of the most widely utilized direct-transition-type materials. Although such materials are in high demand for electro-optical applications, it is technically difficult to implement electrically induced optical functions using the standard doping methods that are used with other types of semiconductors [1–5]. Recently, a technique known as dressed-photon–assisted annealing [6] has been developed to autonomously form a dopant distribution that works as a p–n homojunction layer that is suitable for effectively inducing dressed photons [7] by irradiating the material with light. Based on this approach, various electrically induced optical functions have been successfully demonstrated by using indirect- and direct-transition-type semiconductors [6, 8–15].

We focused on zinc oxide (ZnO). A novel electro-optical modulator has been implemented with this material by using dressed-photon–assisted annealing [6]. We previously reported the results of some experimental demonstrations that revealed giant polarization rotation using a reflective-type device [16]. Polarization rotation is strongly required for reducing laser speckles [17], which are unwanted interference patterns generated in laser-displayed images [18] due to the high coherence of laser light. Here we describe new experimental demonstrations using a transmissive-type device, instead of the reflective-type device, in order to avoid unwanted optical signals due to reflection at the device surface and to improve the practicality for implementing an actual system. We also propose a speckle reduction method based on modulation of the focal position of laser light, instead of the previous method based on polarization rotation [19]. Although their fundamental physics and basic mechanisms are different from each other,

proposed method is expected to have more sufficient performance for practical implementation of a speckle reduction system.

2. OPTICAL MODULATION

To fabricate a transmissive-type ZnO device, we used a commercially available n-type ZnO single crystal, which was prepared by the hydrothermal growth method, and N^+ and N^{2+} ions were doped into the crystal by using multi-step implantation. Then, the doped crystal was set on a glass epoxy substrate with an aperture to allow transmission of incident light. After connecting top and bottom electrodes to the crystal, dressed-photon–assisted annealing [6] was performed; that is, the device was irradiated with laser light during Joule heating brought about by the application of a forward bias current between the electrodes. A schematic diagram and the actual appearance of the device are shown in Fig. 1(a) and (b), respectively.

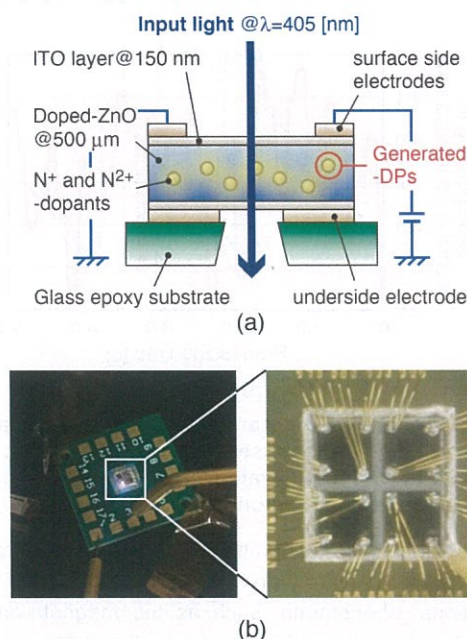


Fig. 1 (a) Schematic diagram of transmissive-type ZnO device and (b) appearance of the device consisting of 2x2 unit elements.

As shown in Fig. 1(a), to demonstrate use of the ZnO

device as an electro-optical modulator, an original arrangement of electrodes was used for applying an in-plane current to the device, so that current-induced magnetic fields induced effective interactions between dopant-originated optical near-fields due to incident light. Based on repeated interactions during propagation of light in the device, finally, extremely large amounts of phase shift and corresponding polarization rotation are obtained.

The experimental setup for demonstrating polarization rotation using the device was designed to observe only modulated light among the linearly-polarized incident light, as shown in Fig. 2(a). Figure 2(b) shows an example of the output light intensity observed with 1 Hz sawtooth modulation of a ± 10 V voltage applied to the device. The result was obtained by extracting pixel values from sequential images, which were obtained by rendering video data. As shown, while the applied voltage was increased to +10 V, the pixel values were changed in four cycles, corresponding to more than 4π radians of polarization rotation.

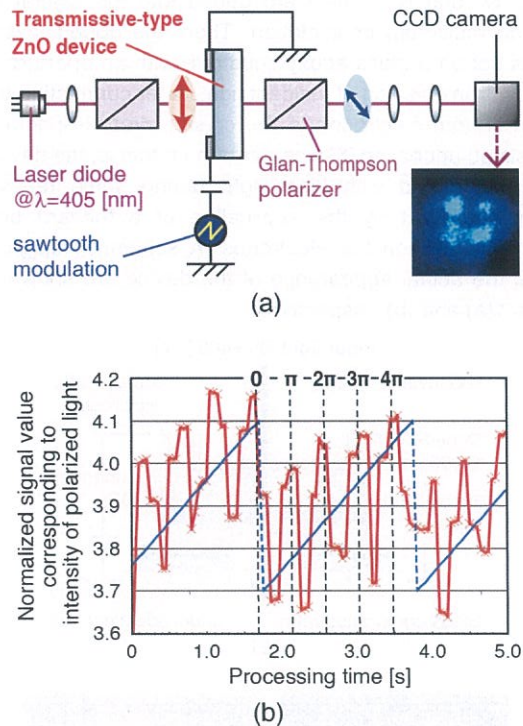


Fig. 2 (a) Schematic diagram of setup for polarization rotation using transmissive-type ZnO device. (b) Experimentally demonstrated modulation of optical intensity due to polarization rotation.

The polarization rotation obtained in this demonstration was many times higher than that achievable using similar conventional phenomena, such as the magneto-optical effect. As we previously described, the origin of the polarization rotation in our device is interactions between current-induced magnetic fields and dopant-originated optical near-fields. In other words, the spatial distribution

of dopants in the device, which is optimized to induce optical near-fields in the areas surrounding each dopant via dressed-photon-assisted annealing, is fundamentally important. Such a strong electrically-induced optical function has never been realized by using oxide semiconductors or any other materials.

3. SPECKLE MODULATION

Because speckle noise is a critical issue in displaying high-resolution images by laser scanning, reducing speckle noise is one of the most important issues in realizing practical laser displays [18]. Although several approaches for reducing speckle noise have been investigated, including a method of decreasing the coherence of laser light so that beams do not interfere with each other [20-22] and generating fluctuating speckle patterns [23-25], there has been no decisive proposal or breakthrough that will enable the practical realization and widespread adoption of laser displays. The main reasons for this are the lack of high-speed, compact, and energy-efficient devices.

Here we propose a novel speckle-reduction method based on high-speed modulation of the focal position of laser light using our transmissive-type ZnO device. Sufficiently high-speed modulation of the focal position enables high-speed modulation of speckle patterns. As a result, the speckle contrast of time-averaged images is necessarily decreased. Due to the novel specifications of our device, we expect that this approach will be one of the most promising breakthroughs in the development of laser displays and related research.

Before demonstrating speckle reduction, we verified that the focal position of the transmitted light could be modulated by a large amount. This was achieved by applying 5 Hz sawtooth modulation to the device and observing the corresponding change of refractive index of the ZnO device. As shown in Fig. 3(a), a noticeable difference was obtained in the light patterns formed on a CCD camera. Moreover, the corresponding refractive index modulation level was approximately calculated by assuming focusing by a single BK-7 lens. The result is shown in Fig. 3(b). As shown, a refractive index change of more than 1.5 % was obtained by applying a voltage of 20 V to the device. Such a result is quite useful for speckle reduction in situations where rapid modulation of the focal position is expected to generate various speckle patterns during the modulation, resulting in lower-contrast, time-averaged images being displayed on a screen.

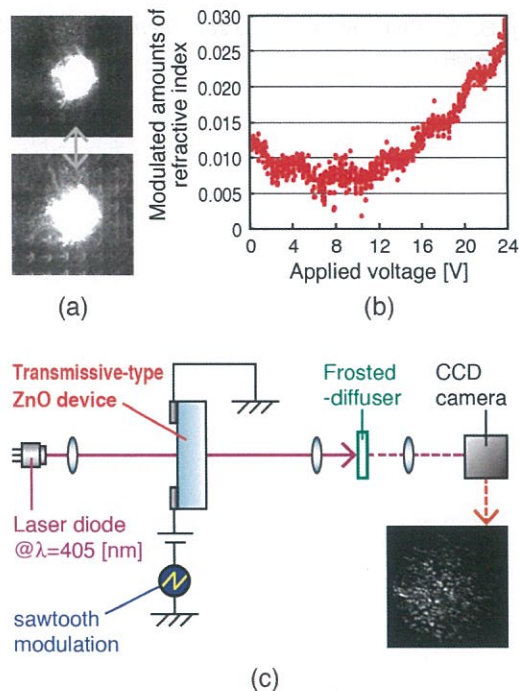


Fig. 3 (a) Experimentally demonstrated modulation of focal position of laser light, and (b) approximate change in refractive index caused by the modulation. (c) Schematic diagram of setup for speckle reduction using ZnO device, and experimentally obtained speckle pattern (inset).

Modulation of the focal position is due to a lens effect in the ZnO device. Specifically, the distribution of current density applied in-plane to the device induces a spatial change in the refractive index distribution, giving rise to a corresponding lens effect. In order to verify the high-speed modulation of speckle patterns by modulating the focal position of the laser light, we constructed another setup using a frosted-diffuser and obtained modulated speckle patterns, as shown in Fig. 3(b).

The main advantages of our idea are the coaxiality and a setup that does not require mechanical devices. The conventional approach [23-25], which is also based on modulation of speckle patterns, additionally requires a mechanical setup to realize high-speed fluctuation of the displayed screen. This is a disadvantage in terms of not only the system complexity but also its implementation cost and power consumption. In contrast, while the basic concept of our approach is similar to the conventional one, our setup does not require any mechanical devices. Therefore, a compact, high-speed system for speckle reduction can be implemented.

4. SUMMARY

We have reported the realization of an original optical modulator, namely, a transmissive-type ZnO device. The results of experimental demonstrations of polarization rotation using the device revealed large amounts of modulation, similar to those we previously demonstrated

using a reflective-type device. Moreover, in order to apply this approach to speckle reduction, we focused on high-speed modulation of the focal position of laser light by using the device. In future research, we plan to quantitatively verify the response characteristics of the modulation and optimize the specifications of the device so that it can be applied to practical speckle reduction for laser displays in the near future.

This work is supported by a research grant from The Murata Science Foundation and by Kyushu University Interdisciplinary Programs in Education and Projects in Research Development.

REFERENCES

- [1] N. Yamazoe, *Sens. Actuators B: Chem.* **5**, Issue 1-4, 7-19 (1991).
- [2] K.D. Schierbaum, et al., *Sens. Actuators B: Chem.* **7**, Issues 1-3, 709-716 (1992).
- [3] G. Kiss, et al. *Thin Solid Films*, **391**, Issue 2, 216-223 (2001).
- [4] K. Nomura, et al., *Nature*, **432**, No. 7016, 488-492 (2004).
- [5] J.S. Park, et al., *Thin Solid Films*, **520**, Issue 6, 1679-1693 (2012).
- [6] T. Kawazoe, et al., *J. Chem. Phys.*, **122**, No. 2, 024715 (2005).
- [7] T. Kawazoe, et al., *Appl. Phys. B*, **104**, No. 4, 747-754 (2011).
- [8] K. Kitamura, et al., *Appl. Phys. B*, **107**, No. 2, 293-299 (2012).
- [9] T. Kawazoe, et al., *Appl. Phys. B*, **107**, No. 3, 659-663 (2012).
- [10] H. Tanaka, et al., *Appl. Phys. B*, **108**, No. 1, 51-56 (2012).
- [11] N. Wada, et al., *Appl. Phys. B*, **108**, No. 1, 25-29 (2012).
- [12] M.A. Tran, et al., *Appl. Phys. A*, **115**, Issue 1, 105-111 (2014).
- [13] N. Wada, et al., *Appl. Phys. A*, **115**, Issue 1, 113-118 (2014).
- [14] M. Yamaguchi, et al., *Appl. Phys. A*, **115**, Issue 1, 119-125 (2014).
- [15] T. Kawazoe et al., *Appl. Phys. A*, **115**, Issue 1, 127-133 (2014).
- [16] N. Tate, et al., *Sci. Rep.*, **5**, No. 12762 (2015).
- [17] J. W. Goodman, *Speckle Phenomena in Optics* (Roberts and Co., Greenwood Village, CO, 2007).
- [18] M. Kuwata, et al., *J. Soc. Inf. Disp.* **17** (2009) 875.
- [19] N. Tate, et al., The 21st International Display Workshops (IDW'14) (2014).
- [20] N. George, et al., *Appl. Opt.* **12**, pp. 1202-1212 (1973).
- [21] F. Riechert, et al., *Appl. Opt.* **48**, pp. 792-798 (2009).
- [22] H. Murata, et al., *Opt. Rev.* **19**, pp. 436-439 (2012).
- [23] S. Lowenthal, et al., *J. Opt. Soc. Am.* **61**, pp.

847-851 (1971).

[24] E. G. Rawson, et al., *J. Opt. Soc. Am.* **66**, pp. 1290-1294 (1976).

[25] S. C. Shin, et al., *J. Disp. Tech.* **2**, pp. 79-84 (2006).

SiC magneto-optical current-transformer applicable to a polarization rotator using dressed photons

Tadashi Kawazoe¹, Naoya Tate², and Motoichi Ohtsu^{1,3}

¹Nanophotonics Engineering Organization, 1-20-10 Sekiguchi, Bunkyo-ku, Tokyo 112-0014, Japan

²Faculty of Information Science and Electrical Engineering, Kyushu University, 744 Motooka, Nishi-ku, Fukuoka 819-0395, Japan.

³Department of Electrical Engineering and Information Systems, Graduate School of Engineering, The University of Tokyo, 2-11-16 Yayoi, Bunkyo-ku, Tokyo 113-8656, Japan

Keywords: Nanophotonics, Polarization, Optical current-transformer, SiC, Dressed photon

ABSTRACT

An magneto-optical current-transformer using SiC was demonstrated. This device was SiC homojunction diode processed by the dressed-photon-phonon annealing. The Verdet constant of the device was 600 deg/A and the Faraday rotation angle was 7800 deg/cm. Its potential as a display component is extremely high.

1. INTRODUCTION

The magneto-optical current-transformer (MOCT) as the current measurement system for large current have been practical realized [1]. The device mechanism is based on the Faraday effect [2]. MOCT as a current sensor is noncontact and insulated operation. Therefore MOCT sensor is suitable for high-power system. The Faraday effect of the transparent material used in MOCT is very small. The Verdet constant, which is the material constant indicating the magnitude of Faraday effect, of those materials, e.g., optical fiber glass, semiconductors and other conventionally paramagnetic materials are 1×10^{-8} - 1×10^{-3} deg/A [3]. On the other hand, the Faraday rotation of the ferromagnetic materials, e.g., Fe(iron), Co(cobalt) and Ni(nickel) are very large ($> 1 \times 10^5$ deg/cm) [4,*]. Such large Faraday rotation is applicable to the polarization rotator as display components. However, conventional ferromagnetic materials are not transparent for visible light.

Recently, we found a giant polarization rotation using a ZnO(zinc oxide) crystal processed by a dressed-photon-phonon (DPP) annealing[5]. Its potential as a display component was extremely high. So far, we have reported homojunction semiconductor LEDs including ZnO and SiC(silicon carbide) fabricated by a dressed-photon-phonon (DPP) annealing [6,7]. Therefore, appearance of the polarization rotation was expected in DPP annealed SiC crystal. 4H-SiC crystal is also transparent for the visible light like a ZnO crystal. If the polarization rotation appears using the SiC crystal, it is also applicable to display components. The polarization rotation using a ZnO crystal is a kind of MOCT but its mechanism is not clarified. Higher stability of the

crystal quality of SiC than that of ZnO strongly supports the clarification of the mechanisms.

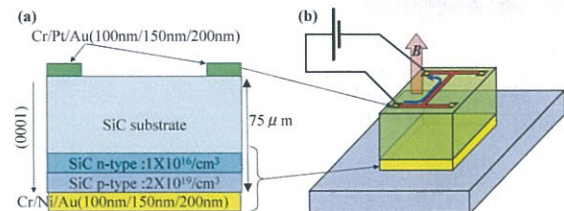


Fig. 1. (a) The cross-sectional structures of the device. (b) The electrode geometry on the top surface of the device. The injection current is carried in the electrode at the device operation, as shown by the blue arrow. The induction magnetic field B is generated by the injection current.

2. EXPERIMENTAL

First, we prepared a SiC p-n homojunction formed by ion implantation in n n-type bulk wafer. The junction structures are shown in Fig.1 (a). The electrodes were fabricated on the both side of the SiC pn homojunction by sputtering. After bonding it on the circuit board, the devices were annealed by Joule heating brought by a forward bias current under laser irradiation. This process is DPP annealing[5-7]. Here, we used a 405 nm laser with a power of 20 mW. After DPP annealing, the SiC homojunction acts as a LED by applying the forward bias currents. When the device is used as a magneto-optical current-transformer, i.e., a polarization rotator, the current is applied along with the patterned electrode, as shown in Fig.1(b), to generate the magnetic field with the normal direction to the top side of the device.

Figure 2 (a) shows a top side photograph of the SiC device chip after DPP annealing. The estimated magnetic flux density is shown in Fig.2 (b) for the current of 30 mA along with the current pathway shown by the yellow arrows in Fig.2(a). The estimated magnetic flux density was 1.8 mT at the center position of the laser irradiation spot. Figure 2(c) shows the experimental setup to demonstrate MOCT. The incident laser with the wavelength of

405 nm is linearly polarized by Glan-Thompson prism. The laser beam is focused onto the SiC device. The reflected laser by the bottom-side electrode of the device returns back to Glan-Thompson prism. Finally, the polarization rotational components is measured by a camera or a photodiode.

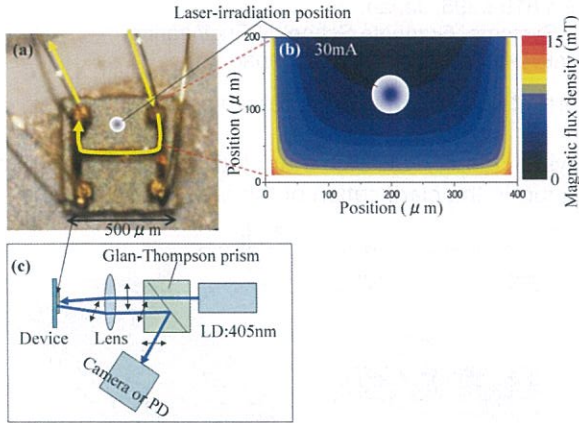


Fig. 2. (a) A top side photograph of the SiC device chip. Currents are shown by arrows at the operation. (b) Calculated magnetic-flux-density distribution in the device. (c) The experimental setup used for Faraday rotation measurement.

3. DISCUSSIONS

Figure 3(a) shows the shot images (insets) and temporal revolution of the signal intensity (a black curve) measured by the camera and the photodiode(PD) shown in Fig.2(c), respectively. The red line shows the temporal evolution of the incident current: triangle wave (frequency: 166Hz). The relation between polarization rotation angle θ and the measured signal intensity I , reflected by the Gran-Thompson prism, is given by $I = a \cdot I_0 \cdot \sin^2 \theta$ where $a(<1)$ is a loss coefficient due to scattering, absorption, and so on. The blue curve is the fitted result by using this relation on the assumption that the rotation angle θ is proportional to the magnitude of the injection current, *i.e.*, the induced magnetic flux density.

Figure 3(b) shows the magnetic-flux-density dependence of the Faraday rotation angle. The blue line shows the Verdet constant of 600 deg/A. The horizontal arrow (\rightarrow) shows the Faraday rotation angle of 7800 deg/cm under the saturated magnetic flux density. Appearance of the threshold value (shown by \downarrow) at $B \neq 0$ indicates the SiC device has a remanent magnetization feature.

4. SUMMARY

An magneto-optical current-transformer using SiC crystal was demonstrated. DPP annealed SiC

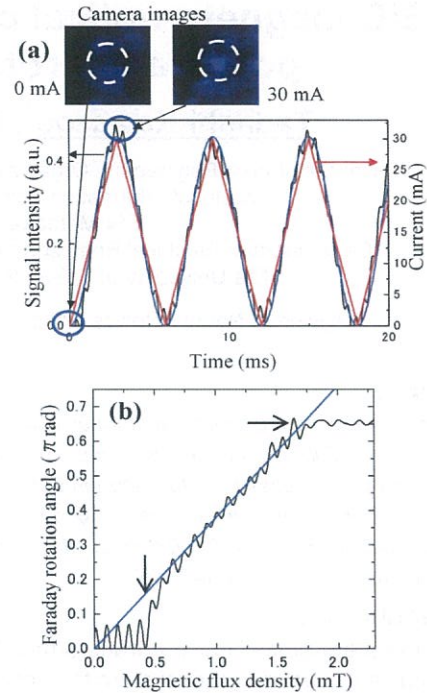


Fig. 3. (a) Detected signal intensity of the photodiode measuring the reflected laser light from the SiC polarization rotator and Glan-Thompson prism. (b)Faraday rotation angle dependence on the magnetic flux density. The blue line shows the Verdet constant of 600 deg/A. A horizontal arrow (\rightarrow) shows the Faraday rotation angle of 7800 deg/cm under the saturated magnetic flux density.

homojunction device had 10^6 times larger Verdet constant (600 deg/A) than that of the conventional paramagnetic material. This device also showed ferromagnetic feature. Its Faraday rotation angle was 7800 deg/cm. The large polarization rotation indicate the extremely high potential as display components.

REFERENCES

[1] A. C. S. Brigida, et al., Photonic Sensors, **3**, 29 (2013).
 [2] A. Papp & H. Harms, Applied optics **22**, 3729 (1980).
 [3] Chronological scientific tables 2015, National Astronomical Observatory of Japan.
 [4] Landolt-Bornstein: Zahlenwerte und Funktionen II-9, Maganetischen Eigenschaften 1.
 [*] Verdet constant is unsuited for the ferromagnetic materials. This is because mechanisms of Faraday rotation of the ferromagnetic materials are different from that of the paramagnetic materials.
 [5] N. Tate, et al., Sci. Rep., **5**, No. 12762 (2015).
 [6] T. Kawazoe, et al., Appl. Phys. A **115**, 127 (2014); Appl. Phys. B **104**, 747 (2012); Appl. Phys. B, **107**, 659 (2012); Appl. Phys. B, **108**, 25 (2012);
 [7] M. Ohtsu, Nanophotonic. **1**, 83 (2012).

Recent progress in dressed-photon–assisted electro-optical modulation

Naoya Tate¹, Tadashi Kawazoe², Shunsuke Nakashima¹, Wataru Nomura² and Motoichi Ohtsu³

¹Kyushu University, 744 Motoooka, Nishi-ku, Fukuoka 819-0395, Japan

Tel.: +81-92-802-3694, E-mail: tate@ed.kyushu-u.ac.jp

²Nanophotonics Engineering Organization, 1-20-10, Sekiguchi, Bunkyo-ku, Tokyo, 112-0014, Japan

³The University of Tokyo, 2-11-16 Yayoi, Bunkyo-ku, Tokyo, 113-8656, Japan

OCIS codes: (160.6000) Semiconductor materials; (200.4740) Optical processing; (230.4110) Modulators; (250.4745) Optical processing devices; (350.4238) Nanophotonics and photonic crystals

We have developed a novel optical modulator using zinc oxide single crystal doped with nitrogen ions and have experimentally demonstrated current-induced giant polarization rotation¹. Our idea is based on dressed-photon–phonon assisted annealing², which autonomously forms a suitable distribution of dopants for effectively generating dressed photons (DPs)³ by applying thermal annealing and light irradiation at the same time. During modulation of light, induced DPs in the regions surrounding clustered dopants are considered to strongly enhance the interactions between input light and current-induced magnetic fields. In the work described in this paper, we present the basic concept of our idea and our recent research activities. In particular, we constructed a physical model of the fundamental phenomena involved in nanometric interactions between magnetic fields and DPs, and we confirmed the validity of this model from the results of some experimental demonstrations.

Previously, by using a reflective-type light modulator (Fig. 1(a)), we achieved a polarization rotation of more than 20π radians by applying a current of 100 mA¹. As shown in the schematic diagram in Fig. 1(b), clustered dopants become the sources of DPs in the presence of incident light. At the same time, current-induced magnetic fields strongly affect the phase of the DPs via the distribution of dopants (Fig. 1(c)). In such a situation, the incident optical energy and magnetic fields are allowed to efficiently interact with each other via the DP states, which are efficiently energetically coupled with the phonon states of the material. After the interaction, reconversion of optical energy from the DPs to propagating light occurs, and other interactions are induced in the regions surrounding other dopants. While the expected amount of modulation in a single process is not large enough, after a number of iterations of this process, a large modulation is eventually realized. This aspect may be experimentally verified by demonstrating the light intensity dependency of the amount of light modulation.

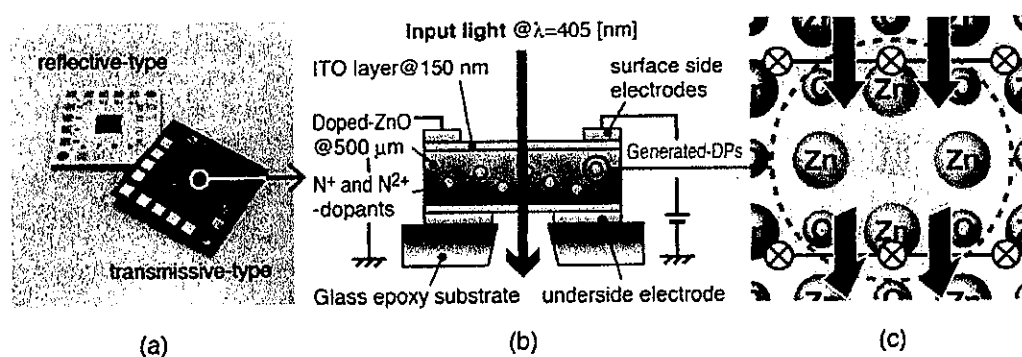


Fig. 1. (a) Photographs of developed reflective- and transmissive-type optical modulators, which consist of 2×2 unit elements. (b) Schematic diagram of a single element of the transmissive device, and (c) nanometrically local interactions between current-induced magnetic fields and DPs in regions surrounding dopants.

Acknowledgment

The research is supported by a research grant from The Murata Science Foundation.

References

1. N. Tate, *Scientific Reports*, 2(9), 243 (2015).
2. T. Kawazoe, et al., *J. Chem. Phys.*, 122, No. 2, 024715 (2005).
3. M. Ohtsu, *Dressed Photons - Concepts of Light-Matter Fusion Technology* (Springer, 2013).

[III] REVIEW PAPERS



ドレスト光子は、ナノ寸法の空間において励起子エネルギーの衣をまとった光子である。本稿ではその発生の原理、性質をオフシェル領域に発生する量子場の観点から紹介する。応用例として、シリコン結晶を材料とする発光ダイオード、レーザーを紹介

し、これらのデバイスが発する光は光子ブリーディングと呼ばれる性質を示すことを指摘する。今後の発展のため、量子場のミクロ・マクロ双対性、複雑系の理論研究を紹介し、研究開発を展望する。

1. まえがき

ガラスファイバの先端の曲率半径を数 nm になるように先鋭化した後に後端から光を入射したとき、先端に光は発生するか？ シリコン (Si) 結晶を使って発光ダイオードやレーザーを作ることができるか？ などの問いに対し、従来の光技術による答えは「不可」であった。しかし、ドレスト光子 (Dressed Photon: DP) を用いた技術では、それらは「可」となる。

このように、従来の光技術とは異なった答えを与える DP に関して、本稿ではその概念、原理を概説した後、応用の最近の状況を紹介します、将来を展望する。

2. ドレスト光子とは

光の量子論的な描像である光子の運動量とエネルギーの関係 (分散関係) を、図 1 に示す。図 1 の破線の直線は、真空中を伝搬する光の場合である。一方、光の波長より大きな寸法の物質中を伝搬する光が電子と正孔の対 (励起子) と相互作用すると、新しい定常状態が物質全体にわたり形成される。この定常状態は励起子ポラリトンと呼ばれる準粒子であり、図 1 中の実線の曲線はその分散関係である。図 1 の直線およびこの曲線が表す状態は、量子場の理論においてオンシェル (on shell) と呼ばれている¹⁾。

一方、図 1 にはこれらの直線、曲線から外れた広い領域があり、ここでは緑色で表している。この領域はオフシェル (off shell) と呼ばれている。

2.1 オフシェル領域の準粒子の特徴

オフシェル領域に準粒子が存在するとすれば、それは次の 2 つの性質をもつ。(1) 図 1 中の水平の両矢印 A で表されるように運動量のとりうる範囲は広い。したがって、運動量と位置に関する不確定性原理から決まる準粒子の存在範囲は光の波長以下である。(2) 図 1 中の垂直の両矢印 B で表されるようにエネルギーのとりうる範囲は広い。したがって、エネルギーと時間に関する不確定性原理から決まる準粒子の存在時間は短い。

(1) の性質からわかるように、オフシェル領域の準粒子は波長以下の寸法のナノ物質^{†1)} 中またはマクロ物質表面にあるナノ構造^{†1)} の位置に局在することから、この準粒子は「近接場光」と呼ばれてきた²⁾。一方、(2) の性質より、これは「仮想光子」と呼ばれている。以上の近接場光と仮想光子の性質を併せて表す用語が「ドレスト光子」である^{3,4)}。すなわち、DP はオフシェル領域に発生する量子場としての準粒子である。

2.2 理論的描像

2.1 節で示した性質 (1) のように、DP はナノ物質やナノ構造に発生する。その簡単な発生方法はナノ物質に伝搬光 (図 1 の破線の直線で表されるオンシェルの光子) を照射することである。このとき、照射光がナノ物質中の励起子と相互作用する。その様子を記述するには系のエネルギーを量子化する必要がある。しかし、その領域はナノ寸法 (光の波長以下) なので量子化のための共振器を定義できない。すなわち、電磁場のモードが定義できない。そこで、無限数のモードの場を

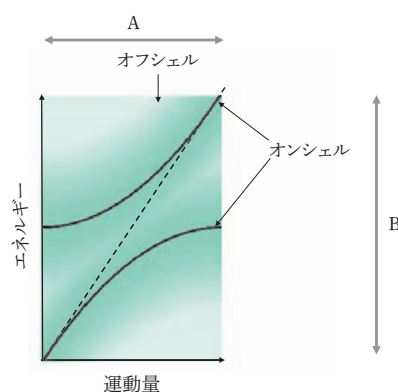


図 1 分散関係.

^{†1)} ナノ物質, ナノ構造 ナノ物質とはナノ寸法の物質のこと。本稿では紫外～赤外の光の波長に比べずっと小さい物質を意味する。一方、寸法がこれらの波長に比べ大きなマクロ物質の表面にも一般にはナノ寸法の突起がある。本稿ではこのような突起部分をナノ構造と呼んでいる。

考える。一方、性質(2)に記したようにエネルギー範囲が広いので、物質中の励起子のエネルギー準位も無限数考える。こうしてハミルトニアンを書き下して対角化し、同時にこの相互作用を表す準粒子の生成・消滅演算子が導出される。これらの演算子は光子の演算子と励起子の演算子の和から成ることから、光子は励起子のエネルギーの衣をまとうと考えられ、DPと呼ばれている^{3,4)}。DPの主な性質は次のとおりである。(a)近接して置かれた複数のナノ物質の間でDPのエネルギーを授受する際、エネルギー授受のポテンシャルエネルギーは湯川関数^{†2}で表され、その空間的広がりにはナノ寸法と同等である⁵⁾。(b)DPは多モードのフォノンのエネルギーの衣をまといDPフォノン(DPP)と呼ばれる新たな準粒子を形成する⁶⁾。このときDPが空間的に局在し、エネルギー範囲が広いことから、多モードのコヒーレントフォノン^{†3}がDPと結合する。(c)DPPは物質の突起部、物質中の不純物原子の位置に選択的に局在する⁷⁾。

3. 発光デバイスへの応用

ナノ寸法空間で発生するオプシタル現象を巨視的寸法空間におけるオプシタル現象に変換することができれば、多くの応用が可能になる。2.2節の(a)~(c)に記した性質を利用することで、これまでに加工、デバイス、システムに関する多様な応用が展開されている⁸⁾。例えば、加工では性質(c)のうち物質の突起部に選択的に局在するDPPを利用する。本章では、物質中の不純物原子の位置に局在するDPPを利用した例としてSi結晶を材料とする発光デバイスを紹介する。

Siは間接遷移型半導体であり、帯間遷移のためには運動量の異なる電子と正孔とが再結合しなければならない。その際、運動量の保存則を満たすためには光子のほかにもフォノンも同時に放出する必要があるが、その放出確率は低い。したがって、これまではSiを発光デバイス用材料として用いることは容易でなかった。しかし、DPPはフォノンを含むので、これが伝導帯中の電子と相互作用すれば運動量の保存則が満たされ、発光デバイスが実現する。そのためには、図2に示すように製作時、および動作時にDPPを使う。

3.1 製作

ここでは近赤外光を発生する発光ダイオード(Light-Emitting Diode: LED)を例にとり、図2(a)に示すDPP援用アニールと呼ばれる製作方法について概説する⁹⁾。まず、n型Si結晶表面にイオン注入法などによりホウ素(B)原子を注入しp型とする。これに順方向電流^{†4}を流し、ジュール熱によりアニール^{†4}する。これによりB原子は熱拡散するが、そ

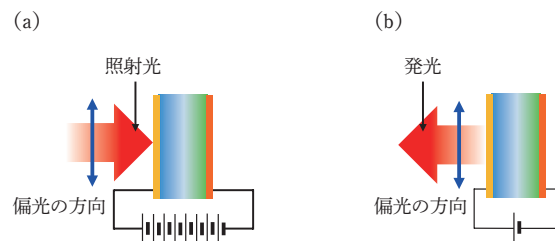


図2 Si結晶を用いた発光素子の製作と動作。(a)DPP援用アニールによる製作。直線偏光を照射する場合。(b)動作時には(a)に示す光を照射する必要はない。電流注入により直線偏光が発生する。

の際結晶表面に波長約1.3 μm の近赤外光を照射する。この光の光子エネルギーはSiのバンドギャップエネルギー E_g (=1.12 eV)に比べ小さいので吸収されず、結晶内部に侵入し、性質(c)によりB原子の位置にDPPを発生・局在させる。

このDPP発生位置付近にある伝導帯中の電子は、DPP中のフォノンと運動量を授受し発光する。これはDPPにより駆動された誘導放出光であり、結晶外部に伝搬する。言いかえると、加熱のために加えられたジュールエネルギーの一部は光エネルギーとなって外部へ散逸する。その結果、DPPの発生した位置ではSi結晶が局所的に冷却され、B原子の拡散は制限される。

このようなDPPの発生、誘導放出、エネルギー散逸が各所で生じ、やがてB原子の空間分布は定常状態に達する。その間、結晶温度は次第に低下し、また発光強度は次第に増加して定常値に達する。以上で製作が終了する。なお、このアニールが効率よく進行するための最適条件は、順方向電流および照射光によりpn接合部に毎秒注入される電子数と光子数の比が1:1であることが確認されている¹⁰⁾。これは上記のジュールエネルギーによる加熱と誘導放出による冷却の釣り合いを表している。

3.2 動作

LEDを動作させる際、図2(b)に示すように、製作時の照射光は不要である。また、順方向電流の値は従来のLEDとほぼ同等であり、これは製作時の電流に比べずっと低い。この電流注入により結晶内部でDPPが発生し、これが発光源となる。図3中の曲線Aは、30分間のDPP援用アニールにより製作されたLEDの発光スペクトルである¹¹⁾。このLEDの外部量子効率の値は15%、発光パワーは1.1Wに達し、高効率・高パワー発光していることが確認されている。

アニール前の微弱な発光スペクトルを、図3の曲線Bに示す。曲線Bの発光スペクトルはバンドギャップエネルギー E_g

^{†2} 湯川関数 $\exp(-kr)/r$ の形をもつ関数。中心力のポテンシャルを表す関数。質量 μ の中間子により媒介される核力のポテンシャルを表すのに使われる。 r はこのポテンシャルの中心位置からの距離。 k は μ に反比例する。

^{†3} コヒーレントフォノン コヒーレント状態にあるフォノン。コヒーレント状態とはボーズ粒子としてのフォノンの消滅演算子の固有状態。この状態では確率密度

関数が時間によらず凝集しており、座標と運動量の不確定性の積が最小である。

^{†4} 順方向電流、アニール 順方向電流とは半導体においてpn接合を形成するp型半導体からn型半導体の方向へ流れる電流である。アニールとは材料の加熱処理技術の一つで、焼きなましとも呼ばれている。本稿では順方向電流により生ずるジュール熱を利用した加熱処理技術を意味する。

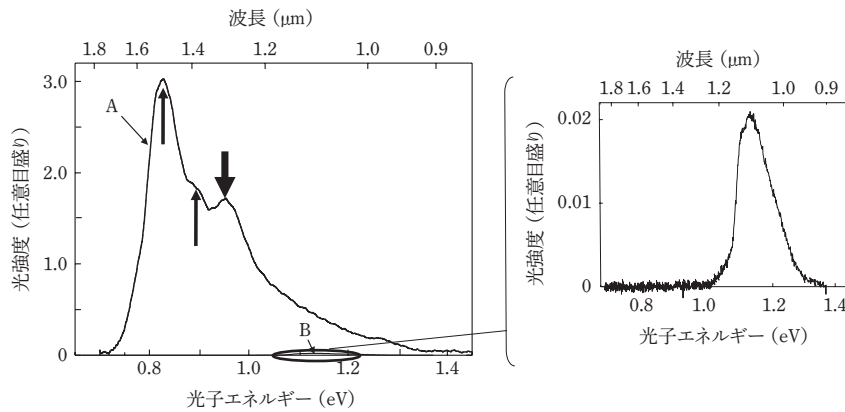


図3 発光スペクトル。曲線Aは製作されたLEDの発光スペクトル。曲線BはDPP 援用アニール前の微弱な発光スペクトル。右図は左図の曲線Bの拡大図。

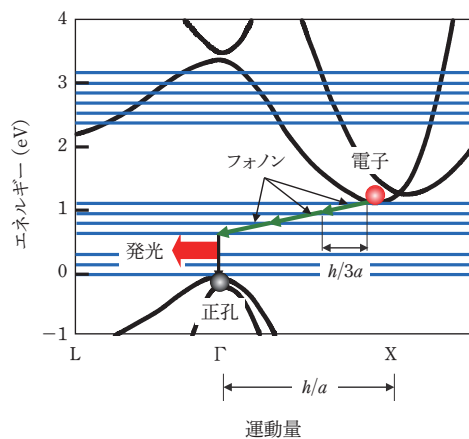


図4 電子の運動量とエネルギーの関係。青い直線は等間隔で並んだ無数のフォノンエネルギー準位のうちの一部分を表す。

より高エネルギー側に分布しているが、これはSi中のフォノン散乱による間接遷移の結果生ずる発光である。曲線Aの形は曲線Bと大きく異なっており、発光スペクトルは E_g 以下の低エネルギー側に広がっている。 E_g の位置に明瞭な発光ピークは存在せず、製作の際に照射した光の光子エネルギー(0.95 eV)に相当する領域にピーク(下向き矢印)が現れている。すなわち、発光は照射光の複製になっており、この現象は光子エネルギーに関する光子ブリーディング(Photon Breeding: PB)と呼ばれている¹²⁾。

なお、2つの上向き矢印の位置での光子エネルギーは0.83 eV, 0.89 eVである。したがって、図3中の3つの矢印の間隔は0.06 eVであり、これはSiの光学フォノンのエネルギーと一致している。すなわち、2つの上向き矢印は0.95 eVのエネルギーをもつDPPが1個の光学フォノンを放出し発光する過程、および2個の光学フォノンを放出して発光する過程にお

の対応している。これらの過程はこれらのフォノンが運動量の授受に関わっていることを表している。

DPP 援用アニールの際に直線偏光を照射すると、製作されたLEDからの発光も同様に直線偏光することが確認されている¹³⁾。これは光子スピン^{†5}に関するPBである。以上の知見に加え、電子正孔対とフォノンとの結合の大きさを表すHuang-Rhys因子が4.08と推定されているが¹⁴⁾、これはDPP 援用アニール前のSi結晶の値に比べ $10^2 \sim 10^3$ 倍大きく、LEDの発光がDPPに起因することを示している。また、コヒーレント状態の縦モード光学フォノンがDPと結合しDPPを形成していることも確認されている¹⁵⁾。

PBの起源を探るために、アトムプローブ法^{†6}を用いB原子の空間分布が測定された¹³⁾。その際、1つのB原子とその近隣にあるもう1つのB原子に注目し、両者をB原子対と見なしてその長さや方向が評価された。なぜならば、性質(c)に加え、不純物の対があるとフォノンはさらに局在しやすくなるため、このB原子対はDPPを生成するためのフォノン局在中心として働くことが指摘されているからである¹⁶⁾。この性質に留意して上記の測定結果を精査した結果、DPP 援用アニール前にはB原子分布はランダムであるが、アニール後にはB原子対の長さ d はSi結晶の格子定数 a の3倍($d=3a$)、かつその方向は入射光の伝搬方向と垂直面内(結晶表面と平行)となっていることが確認された¹³⁾。すなわち、B原子の空間分布に規則性が生じたが、これをSi結晶のエネルギー帯構造をもとに考察すると次のようになる。

近赤外光の発生に関わる電子の伝導帯の底は、図4に示すようにX点近傍にあり、価電子帯の頂上はΓ点にある。この位置の電子と正孔が再結合し発光するには、電子とフォノンとの間でのX点とΓ点の差に相当する運動量の授受が要求される。X点とΓ点の差に相当する運動量は h/a (h はプランク定数)であるが、 $d=3a$ の場合、このB原子対に局在するフォノンの運動量は $h/3a$ となり、必要な値の1/3である。ここで、DPPを構成するフォノンはコヒーレント状態であることから複数のフォノンを含み、したがってフォノン3つ分の運動量を電子と授受することができる。この結果、上記の要求に応え電子は正孔と再結合して発光し、その光子エネルギーは $E_g - 3E_{\text{phonon}}$ (E_{phonon} はフォノンのエネルギー)となるが、こ

†5 光子スピン ポーズ粒子としての光子のスピン。古典光学における円偏光状態に対応。

†6 アトムプローブ法 アトムプローブ電界イオン顕微鏡法。電界イオン顕微鏡に飛行時間型質量分析器を取り付けた装置を用いて、物質表面の個々の原子を観察・同定する局所分析法である。

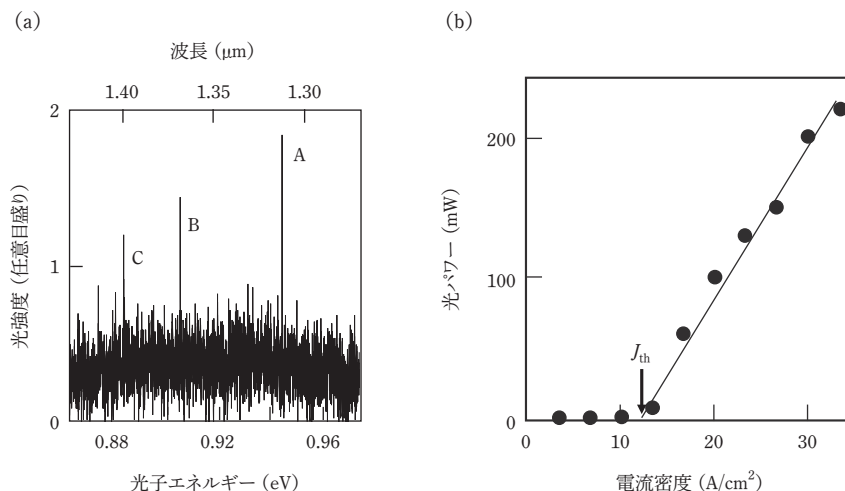


図5 レーザーの発振特性。(a)発振スペクトル。(b)注入電流密度と両端面出力パワーとの関係。

の値が製作時の照射光の光子エネルギーと等しい。これが光子エネルギーに関するPBである。言いかえると、製作の際にB原子は自律的にその空間分布を変え、電子とフォノンとの運動量の授受、それによる発光、PBの効果を実現させているのである。

また、製作の際に直線偏光を照射した場合にもアニール後のB原子対の長さ、方向は上記と同等となり、さらに直線偏光の方向と垂直に配列することが確認されている¹³⁾。製作の際にはDP中の横モードの光学フォノンがDPP援用アニールに寄与するが、このフォノンの格子振動の方向はDPP援用アニールの際の照射光の直線偏光の方向と平行である。動作時にもこのフォノンが発光に寄与するため、発光の偏光方向は照射光の偏光方向と一致するのである。これが光子スピンに関するPBの原因である。

Si結晶に共振器構造を作り付けることにより、上記LEDと同様の近赤外光を発するレーザーも製作されている¹⁷⁾。この結晶はホモpn接合であるため、レーザー用の光導波路の光閉じ込めの効果は低い。しかし、赤外光に対するSiの吸収損失が低いことに注目し、高出力化を目的として狭ストライプ導波路を使わない長共振器(長さ1mm)構造が採用された。このように大きな共振器であるため、図5(a)のスペクトルが示すように、多モード発振となっている¹⁸⁾。そのうち、スペクトルピークAで表される発振モードの光子エネルギーはDPP援用アニール時の照射光の光子エネルギーと等しく、PBの効果を表している。ピークB、Cはフォノンによる側波帯で、おのおの縦モード、横モードの光学フォノンの寄与による。図5(b)に示すように、発振のためのしきい値電流密度 J_{th} は 12.5A/cm^2 、共振器両端面出力パワー200mWに達し、低いしきい値電流密度・高パワー発光を実現している。

以上の発光デバイスのほか、Si結晶を用いた可視光のLED¹⁹⁾、Siと同様の間接遷移型半導体であるSiC結晶²⁰⁾、GaP結晶を用いたLED²¹⁾、さらには光増幅機能付きの光検出器^{22,23)}、偏光変調器²⁴⁾なども実現している。

4. 将来展望

図1中の直線と曲線が占めるオンシユルの領域は狭く(線分なので面積は0)、したがって、そこに存在する光子(伝搬光)は極めて特殊な量子場といえよう。従来の光技術は、このような特殊な光子を使ってきたのである。それに対し、オフシユルの領域は広いので、そこに存在する量子場のほうがより一般的である。また、オンシユルの技術では第1章冒頭の質問に対する答えは「不可」であったが、オフシユルの技術では「可」となった。オンシユルとオフシユルは図1中で互いに排他的な領域を占めるので、このように相反する答えが出ても奇異ではなく、両技術の間には共通点はない。

あえて共通点を見いだすとすれば、DP、DPPの発生、検出に伝搬光を使うことである。すなわち、前者ではナノ寸法の空間にDP、DPPを生成させるために伝搬光を照射する。後者ではDP、DPPが関与する光・物質相互作用が生じた結果を、そこから生ずる伝搬光として検出する。これまでに、DPおよびDPPの応用は広範囲で進展しているが、今後は上記の発生、検出の過程を詳しく調べることにより関連技術の一層の発展が期待される。

オフシユルの領域に存在する量子場という新しい概念には新しい理論的アプローチが必要となり、それは従来の光学理論の外部にある理論体系を導入する必要がある。最近はそのための研究が進んでいる。その1つはオフシユルとオンシユルの間の変換、言いかえると、ナノ寸法の微小な空間におけるDP、DPPの関わる現象を外部の巨視的空間から制御して発生させる方法、およびエネルギーの移動と散逸を経て検出する方法を精査することである。これには量子場のマイクロ・マクロ双対性に関する研究の手法が使われ^{25,26)}、DPP援用アニールにより発現したB原子対の配列に関わる規則性を手がかりに研究が進んでいる。

もう1つはDP、DPPが光子、電子、フォノンから成る複合粒子であることに注目し、これを複雑系と捉える方法である。このときDP、DPPを発光源として機能する前章の発光デバイ

スも同じく複雑系と考え、デバイス用材料にデバイス性能を還元するのではなく、材料中の独特の構造が自律的に生成される過程に注目する（そうしないと、「Si 結晶を使って発光ダイオードやレーザーを作ることは不可」というオンシェル固有の結論になってしまう）。

この考え方にに基づき、最近では数値シミュレーションが行われている。そのために、B 原子の拡散を相互作用をもつランダムウォークと見なし、さらに光子、電子、フォノンの結合を平均場的な相互作用をもつポアソン過程として表す多粒子確率過程モデルがつけられた。その結果、アニール時の結晶温度低下、発光強度増加、アニールの最適条件、PB の効果などの実験結果が再現された²⁷⁾。

このシミュレーションで再現された B 原子対は互いに孤立し、その空間分布はまばらである。この特徴は互いに斥力を有する多数の微粒子が形成する空間分布を表す過程（ジニブル点過程）と類似している²⁸⁾。さらに、このまばらな空間分布は従来の固体レーザー中の互いに孤立したイオンの空間分布と類似である。

B 原子対がこのようにまばらに分布するため、いったん発光すればその光は Si 結晶中で吸収されることなく外部へ出射され、高パワーが得られる。高利得発光は DPP と電子との相互作用により、さらに低吸収損失は DPP により制御された B 原子対の分布によりもたらされたのである。

今後は以上の考察を基に、発光デバイスの設計指針の確立が望まれるが、より重要なのは DP、DPP が関与する現象をもたらし自律的構造形成の詳細を明らかにしていくことである。

5. むすび

ナノ寸法の空間において励起子のエネルギーの衣をまとった光子であるドレスト光子について、オフシェル領域に発生する量子場の観点から発生の原理、性質を紹介した。また DP は多モードのコヒーレントフォノンと結合し、ドレスト光子フォノンと呼ばれる新たな準粒子を形成して物質の突起部、物質中の不純物原子の位置に局在することを記した。

ドレスト光子、ドレスト光子フォノンは加工、デバイス、システムに幅広く応用されているが、ここでは Si 結晶を材料とする発光ダイオード、レーザーを紹介した。これらのデバイスが発する光の光子エネルギーは製作の際に照射する光の光子エネルギーの複製になっていること、すなわち光子ブリーディングと呼ばれる性質を示すことを指摘した。

最後に、今後の発展のための理論研究として量子場のマイクロ・マクロ双対性の観点から扱う方法、DP と DPP が関与する現象を複合系複雑系と捉える方法とその現状について紹介した。

謝辞

DP の理論研究にご協力いただく小嶋泉（元・京都大学）、西郷甲矢人（長浜バイオ大学）、岡本和弥（名古屋大学）、香取眞理（中央大学）の各氏に感謝します。また実験研究

にご協力いただく川添忠（（特非）ナノフォトニクス工学推進機構）、八井崇、金俊亨（共に東京大学）の各氏に感謝します。本研究の一部は（独）日本学術振興会（JSPS）研究拠点形成事業（A.先端拠点形成型）、科学研究費補助金（挑戦的萌芽研究）の支援を受けた。また第 4 章の理論研究は主にドレスト光子研究起点において行われた。

文献

- 1) R.P. Feynman: *The Theory of Fundamental Processes* (W.A. Benjamin, 1962).
- 2) M. Ohtsu: *Progress in Nanophotonics IV*, M. Ohtsu ed., p.1 (Springer, 2017).
- 3) 大津元一：ドレスト光子——光・物質融合工学の原理, p.10 (朝倉書店, 2013).
- 4) M. Ohtsu: *Dressed Photons: Concepts of Light-Matter Fusion Technology*, p.11 (Springer, 2013).
- 5) K. Kobayashi and M. Ohtsu: *J. Microscopy* **194**, 249 (1999).
- 6) Y. Tanaka and K. Kobayashi: *Physica E* **40**, 297 (2007).
- 7) Y. Tanaka and K. Kobayashi: *J. Microscopy* **229**, 228 (2008).
- 8) M. Ohtsu: *Progress in Nanophotonics* **1**, M. Ohtsu ed., p.1 (Springer, 2011).
- 9) M. Ohtsu: *Silicon Light-Emitting Diodes and Lasers: Photon Breeding Devices using Dressed Photons*, p.16 (Springer, 2016).
- 10) J.H. Kim, T. Kawazoe, and M. Ohtsu: *Appl. Phys. A* **121**, 1395 (2015).
- 11) T. Kawazoe, M.A. Mueed, and M. Ohtsu, *Appl. Phys. B Lasers O.* **104**, 747 (2011).
- 12) M. Ohtsu: *Progress in Nanophotonics IV*, p.10 (Springer, 2017).
- 13) T. Kawazoe, K. Nishioka, and M. Ohtsu: *Appl. Phys. A* **121**, 1409 (2015).
- 14) M. Yamaguchi, T. Kawazoe, and M. Ohtsu: *Appl. Phys. A* **115**, 119 (2014).
- 15) N. Wada, M.-A. Tran, T. Kawazoe, and M. Ohtsu: *Appl. Phys. A* **115**, 113 (2014).
- 16) D.N. Payton and W.M. Visscher: *Phys. Rev.* **154**, 802 (1967).
- 17) M. Ohtsu: *Silicon Light-Emitting Diodes and Lasers: Photon Breeding Devices using Dressed Photons*, p.84 (Springer, 2016).
- 18) M. Ohtsu: *Highly Coherent Semiconductor Lasers*, p.43 (Artech House, 1992).
- 19) M.A. Tran, T. Kawazoe, and M. Ohtsu: *Appl. Phys. B* **115**, 105 (2014).
- 20) T. Kawazoe and M. Ohtsu: *Appl. Phys. B* **115**, 127 (2014).
- 21) J.-H. Kim, T. Kawazoe, and M. Ohtsu: *Adv. Opt. Technol.* **2015**, 236014 (2015).
- 22) H. Tanaka, T. Kawazoe, and M. Ohtsu: *Appl. Phys. B* **108**, 51 (2012).
- 23) 池川晶貴, 川添忠, 大津元一：第 63 回応用物理学会春季学術講演会予稿集, 19a-S622-9 (2016).
- 24) N. Tate, K. Kawazoe, W. Nomura, and M. Ohtsu: *Sci. Rep.* **5**, 12762 (2015).
- 25) I. Ojima: *Stochastic Analysis: Classical and Quantum Perspectives of White Noise Theory*, T. Hida ed., p.143 (World Scientific, 2005) arXiv: math-ph/0502038.
- 26) I. Ojima and H. Saigo: *Mathematics* **3**, 897 (2015).
- 27) M. Katori and H. Kobayashi: *Progress in Nanophotonics IV*, M. Ohtsu ed., p.21 (Springer, 2017).
- 28) J. Ginibre: *J. Math. Phys.* **6**, 440 (1965).

(2016 年 7 月 15 日 受理)

Profile



大津 元一（おおつ もといち）

1978 年東京工業大学大学院博士課程修了。同大助手、助教授。教授を経て、04 年東京大学大学院工学系研究科教授。16 年定年退職。その後、現所属、東京大学および東京工業大学名誉教授。ドレスト光子研究起点代表。

総論：ドレスト光子とは何か？その応用展開は？

東京大学
大津元一

1 オンシェルvsオフシェル

本シリーズでは実用化が加速されている日本発の独創技術「ドレスト光子工学」の現状を紹介し将来を展望する。【第1回】の本稿ではその概念、原理から応用展開、さらに将来展望を概説する。

そのためにまず準粒子（素励起：多体系の励起状態）の運動量とエネルギーとの関係、すなわち分散関係について考えよう¹⁾。光が物質に入射すると光子は物質に吸収され励起子（固体中の電子・正孔対を一つの粒子と見なした準粒子）が発生するが、その後、この励起子が消滅し光子が発生する。この繰り返しの現象が物質中を伝搬する。すなわち光子と励起子が互いに時間的および空間的に逆位相で生成、消滅を繰り返す。この現象は光子と励起子との相互作用により新しい定常状態が物質全体にわたり形成されることを意味しているが、この定常状態は分極場と考えられポラリトンと呼ばれる準粒子である。特にこれは光子と励起子とが相互作用した結果生じた準粒子なので励起子ポラリトンと呼ばれており、電磁場と励起子の分極場とが作る連成波である。励起子ポラリトンの運動量（波数に比例、波長に反比例）とエネルギーの関係は分散関係と呼ばれており図1中の実曲線により表される。従来の光技術ではこの曲線を使って材料やデバイスが設計されている。

この他の準粒子の例としてフォノン（結晶中の格子振動の基準モード）、プラズモン（電子気体中の電子密度

の集団運動）、ポラロン（伝導電子と光学フォノンの結合）、マグノン（スピン密度波の集団モード）などがあるが、それらの分散関係もこのような実曲線によって表される。この曲線は量子場の理論などでオンシェル（on shell）と呼ばれている²⁾。一方この図には実曲線から外れた広い領域があり、ここでは灰色で表している。この領域はオフシェル（off shell）と呼ばれている。

オフシェル領域に存在する準粒子の特性は次のとおりである。

- (1)運動量 p 、波数 k の取り得る範囲 Δp 、 Δk は広い。従って不確定性原理 $\Delta p \Delta x \geq \hbar$ から決まる準粒子の寸法 Δx

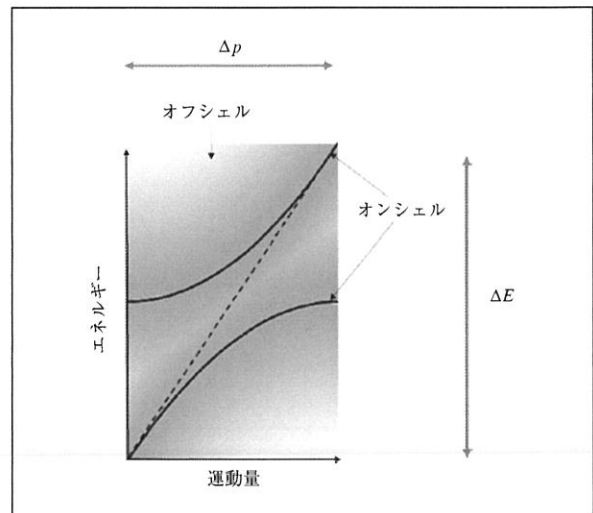


図1 分散関係の例
実線は励起子ポラリトンの場合。破線は真空中の光の場合。

は小さく、波数 k との間の不確定性原理 $\Delta k \Delta x \geq 1$ から励起用の光の波長以下である。

(2)エネルギー E の取り得る範囲 ΔE は広い。従って不確定性原理 $\Delta E \Delta t \geq \hbar$ から決まる準粒子の存在時間 Δt は短い。

(1), (2)の特性は各々「近接場光」, 「仮想光子」なる用語により表されている。これらの特性を表す統一用語が「ドレスト光子 (dressed photon: DP)」である^{3,4)}。すなわちDPはオフシェル領域に発生する量子場としての準粒子に他ならない。

(1)からわかるように、DPは真空中ではなく物質中またはその表面に発生し、その領域はナノ寸法(すなわち光波長以下)なので場の量子化のための共振器を定義することはできない。そこで無限モードの場を考え、その重ね合わせとして表す。一方、DPは物質とエネルギーをやりとりするが、(2)のようにDPのエネルギー範囲は広いので、物質中の電子のエネルギー準位も無限数考える。こうしてDPの生成消滅を表す演算子が導出されたが、それらは光子の演算子と電子の演算子の和からなることから、光子は電子エネルギーの衣をまとっていると考えられ、DPと呼ばれている^{3,4)}。DPはまたフォノンのエネルギーの衣をまといDPフォノン(DPP)と呼ばれる準粒子を形成する。DPが空間的に局在し、エネルギー範囲が広いことから、ここで扱うフォノンは局在、かつコヒーレント状態のフォノンである。

2 応用展開

DPPは(a)ナノ物質中または表面に発生する。さらに、マクロ物質でも(b-1)表面のナノ寸法の突起部、(b-2)内部のナノ寸法の不純物表面にも発生する。これらのDPおよびDPPの特性を利用し、多様な技術が生まれている⁵⁾。その主なものは下記のとおりである。(図2)

(i)微小な光デバイス：半導体のナノ物質の間でのDPを介したエネルギー移動を利用することによりナノ寸法の光デバイス、すなわちドレスト光子デバイスが作られている。このデバイスでは特定の寸法比をもつ大小二つのナノ物質の間でのエネルギー移動、それにより第二のナノ物質中に励起された電子正孔対の緩和によ

るエネルギー散逸を利用して光信号を伝送し取り出す。これまでに多様なデバイスが開発されており、さらにこれらを用いたナノ寸法の光ルータシステムや情報セキュリティシステムが開発されている。

(ii)微細加工：フォトマスク開口端部に発生させたDPPによるリソグラフィ、さらにはフォトマスク等の特別な部品を使わず被加工物質表面の小さな突起に発生するDPPを用いた自己組織的な物質表面の超平坦化技術などが開発されている。

(iii)光エネルギー変換：DPは多くのエネルギーを含んでいるのでエネルギー上方または下方変換の現象が生じる。例えば色素微粒子の間でのDPPのエネルギー移動の際のエネルギー上方変換を利用し、赤外光が可視光に変換されている。一方、下方変換を利用し紫外光を可視光に変換する技術も進展している。

(iv)光子ブリーディング素子：従来の光源には発光ダイオード(LED)、レーザーなどがあるが、これらに対し、本技術による発光デバイスはその原理、作製方法、特性が全て異なることから「第三の光源」と位置づけられ、光子ブリーディング素子と呼ばれている。

本シリーズの第2回、第3回ではこれらのうち次の二例について紹介する。

【第2回】物質表面の超平坦化研磨⁶⁾(図3(a))：光エッチングを用いる。すなわち物質表面に光を照射する。このとき上記(a)、(b-1)によると表面の突起部にDPPが発生する。そこにエッチング用分子があれば、DPPにより分子は解離し、析出した化学反応性の強い原子で突起部をエッチングする。このとき前節(2)によればDPPのエネルギー範囲 ΔE は広いので、照射光は紫外線よりも低エネルギーの可視光でよい。従ってDPPの発生しない平坦部はエッチングされないため、自律的な超平坦化が実現する。

【第3回】シリコン(Si)結晶を用いた発光素子^{7,8)}(図3(b))：Siは間接遷移型半導体であるため、従来技術では長年にわたり発光素子には不適であると考えられてきた。しかし伝導帯中に注入された電子がDPP中のフォノンと運動量を授受し、帯間遷移・発光する。この素子の製造には上記(a)、(b-2)を利用しDPP援用のジュール熱アニールを用いる。製造された素子からの電流注

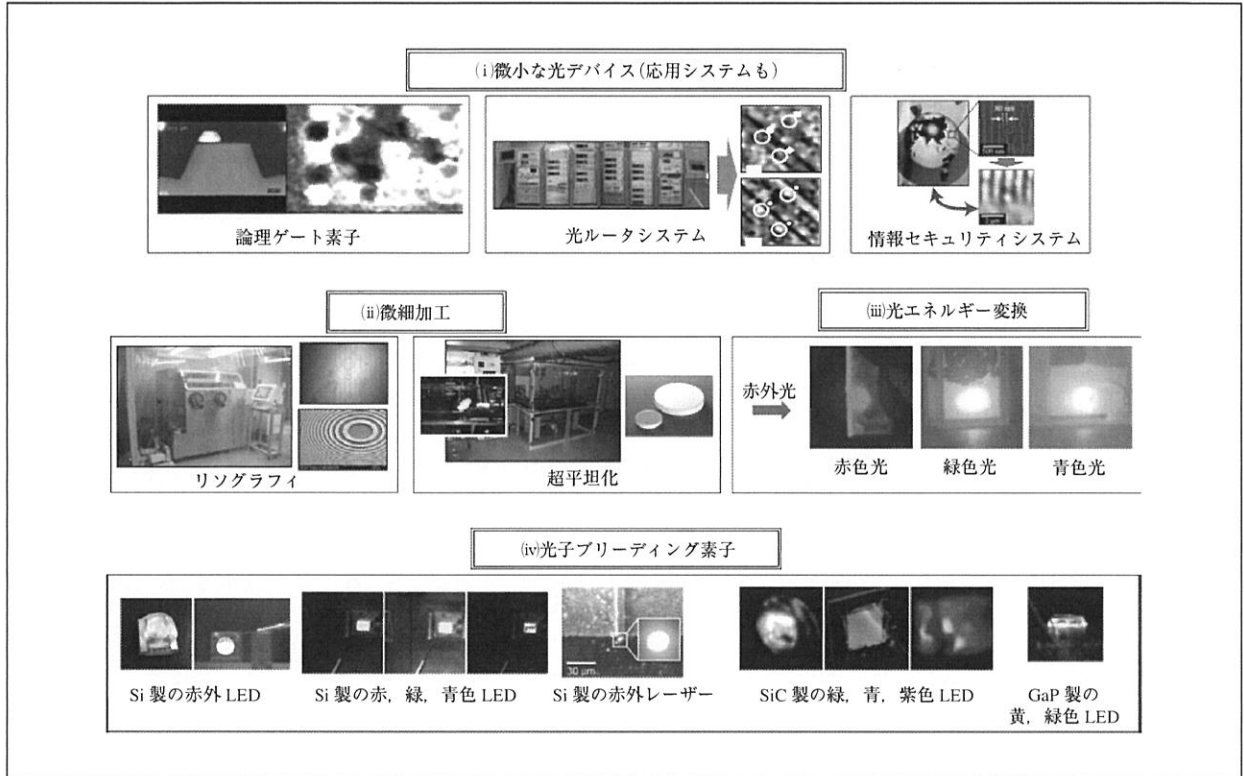


図2 応用技術の例

入発光の光子エネルギーは素子製造の際に照射する光の光子エネルギーと同等である。この特性は光子ブリーディング (photon breeding) と呼ばれ、この素子が上記(iv)

のように光子ブリーディング素子と呼ばれる所以である。特に赤外発光の場合、Siは発光した赤外線を吸収しないため、高効率・高パワーの発光素子となる。

DPの応用技術は光が関わる多くの分野をカバーし包括技術として発展している。そのため知財の状況も独特であることから、【第4回】では特許戦略の動向の調査分析結果を紹介する。

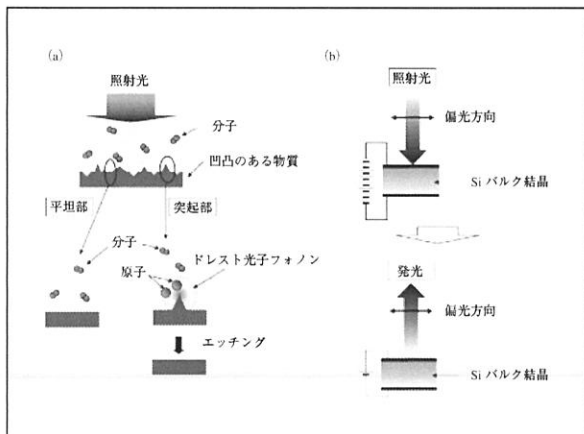


図3 本シリーズで取り上げる応用例の原理
(a) 物質表面の超平坦化研磨。(b) 発光素子の製造と使用。

3 将来展望

DPの関わる現象は光関連分野にとどまらず、自然界の多くの現象との類似点が見出されている⁹⁾。それらはナノ系、マクロ系、無機物、有機物など多岐にわたる(図4)。たとえば、ハドロン族(特に中間子)、光活性の磁気センサータンパク質、光合成細菌の光捕獲システム、粘菌コンピューティング、岩石の風化、宇宙空間の相対論的ジェット中に見られる放射エネルギー上

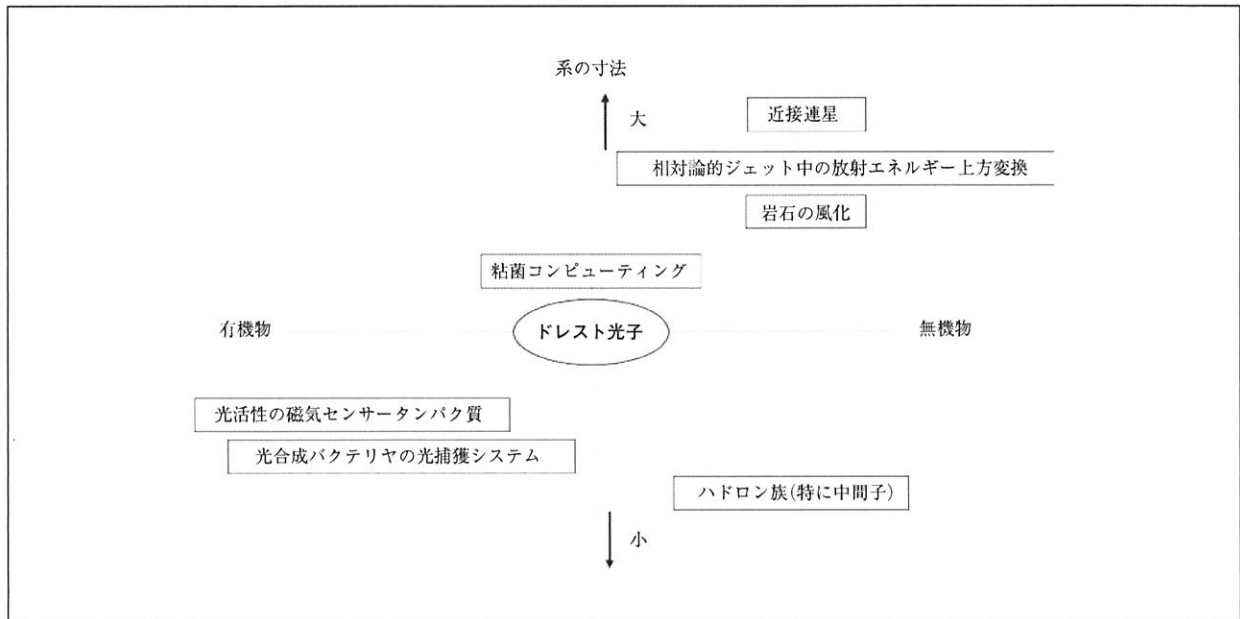


図4 ドレスト光子と類似の現象

方変換, 近接連星などである。これらの現象との共通点, 差異を明らかにするには

- (ア) DPが発生するナノ系から, それを取り囲むマクロ系へのエネルギー移動と散逸
- (イ) ナノ系とマクロ系とのエネルギー移動および階層性

などの特性を明らかにする必要がある。(ア)の場合, ナノ系はマクロ系と接続し外部に向けて開放されているので, DPの観測は量子力学が取り扱う閉じた系の中の現象の範囲を超えている。さらに(イ)の解析のためには量子場におけるマイクロ・マクロ双対性¹⁰⁾に関する考え方と理論の導入が必要である。もちろんDPはオフシユールの量子場を表す準粒子なので, マクスウェル方程式による解析, FDTD法による数値シミュレーションで議論できるものではない。【第5回】ではこれらに取り組む理論的方法について紹介する。

参考文献

- 1) D. Pines, *Elementary Excitation in Solids* (Perseus Books, Reading, Massachusetts, 1999).
- 2) R. P. Feynman: *The Theory of Fundamental Processes* (W. A. Benjamin, New York, 1962) pp. 95-100.
- 3) 大津元一, 「ドレスト光子」(朝倉書店, 東京, 2013) pp. 10-32.
- 4) M. Ohtsu, *Dressed Photons* (Springer, Berlin, 2013) pp. 11-36.
- 5) M. Ohtsu, *Opt. Rev.* vol. 21, no. 6 (2014) pp. 905-910.
- 6) 八井崇, 大津元一, レーザー加工学会誌, 第20巻, 第2号, 2013, pp. 130-132.
- 7) 大津元一, 川添忠, 光学, 第43巻, 第8号, 2014, pp. 366-370.
- 8) T. Kawazoe, K. Nishioka, and M. Ohtsu, *Appl. Phys. A*, vol. 121, issue 4, (2015) pp. 1409-1415.
- 9) 大津元一, 光技術コンタクト, 第53巻, 第6号, 2015, pp. 3-13.
- 10) 小嶋泉「量子場とマイクロ・マクロ双対性」(丸善, 東京) 2013.

■Introduction: Dressed photon and future of its application technology

■Motoichi Ohtsu
 ■The University of Tokyo

オオツ モトイチ
 所属：東京大学

International Center for Nano Electron and Photon Technology: At the Forefront for Global R&D and International Collaboration

MOTOICHI OHTSU
DIRECTOR

INTERNATIONAL CENTER FOR NANO ELECTRON AND PHOTON TECHNOLOGY, THE UNIVERSITY OF TOKYO

HISTORY

The International Center for Nano Electron and Photon Technology (InCEPT) is the successor to the Nanophotonics Research Center (NPC), which was established in 2008 at the Institute of Engineering Innovation, which is affiliated with the School of Engineering at the University of Tokyo.

Nanophotonics, which involves the study of novel optical devices, fabrication technologies, and security systems by utilizing light-matter interactions on the nanometer scale via optical near-fields, was proposed by Professor Motoichi Ohtsu [1], the director of the NPC and InCEPT. A number of novel aspects of nanophotonics, called “qualitative innovations”, were revealed by exploring and exploiting the unique behavior that is exhibited by light-matter interactions on the nanometer scale. Nanophotonics has opened up a variety of research topics, ranging from the study of very basic physical mechanisms to practical applications. For example, nanophotonics is revealing unique connections with electron-spin while also enabling innovative system applications.

The NPC explored cutting-edge research in nanophotonics, promoted collaborations with industry and provided outreach activities such as seminars, workshops, and international collaborations. The NPC endeavored to be an inspiring, excellent, internationally-renowned research organization for nanophotonics.

The remarkable achievements of the NPC have triggered strategic discussions for expanding research areas and for further promoting international collaborations. To reflect these new directions, the NPC was dissolved and

InCEPT, a new center for global R&D completion and international collaboration, was launched in 2014.

MISSION

A wide range of new technologies were developed at the NPC, which included technologies for sensing, devices, information processing, and biotechnology. These technologies were based not only on nanophotonics but also on the science of nanoscale electron-photon interactions. In order to achieve even more robust progress in the ever-widening and developing field of nanoscale electron-photon science and technology, more systematically organized frameworks will be important. One mission of InCEPT is to engage in activities aimed at enriching and developing the science and technology of nanoscale electron-photon interactions even further.

In addition to setting up a more systematic framework to allow high-level academic study in this area, some other important missions of InCEPT are to promote collaboration with industry and academia, to provide outreach activities and to develop the field internationally.

RESEARCH ACTIVITIES

InCEPT is directed by Prof. M. Ohtsu, and its core members are five professors who are leading researchers in their respective fields. Five associate professors, one assistant professor, and two research associates support them. About 80 graduate students, originating not only from Japan but also from the Asia-Pacific region, and from American and European countries, are also mem-

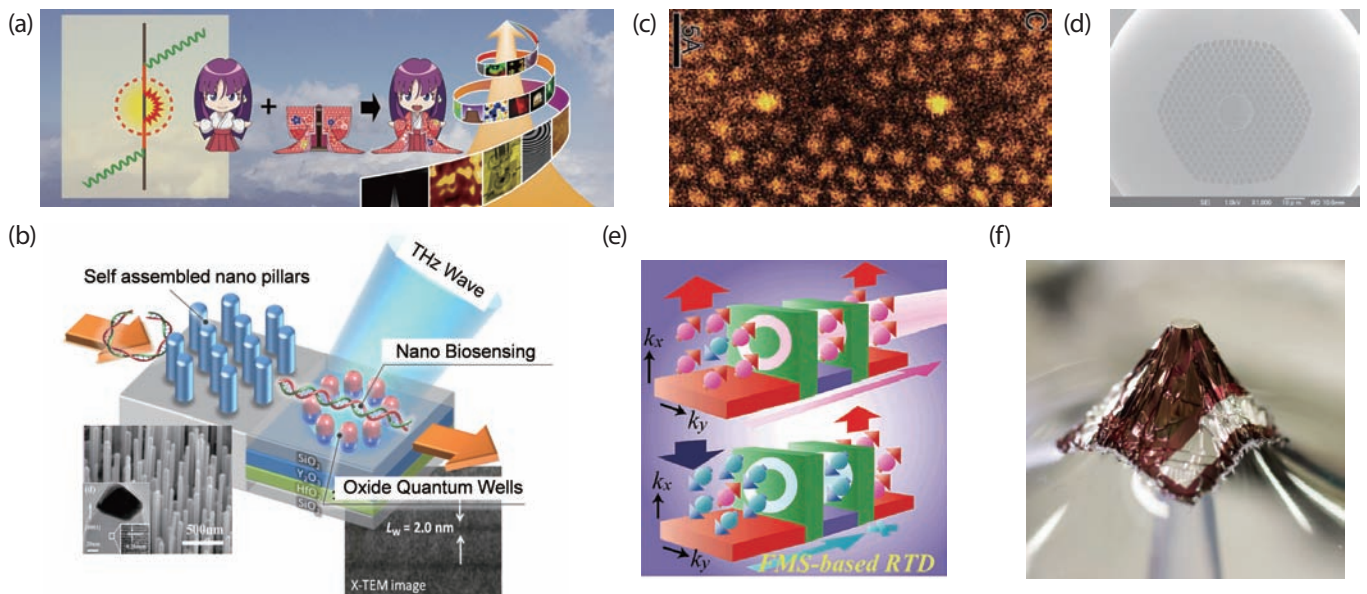


Fig. 1: Schematic diagram of research topics. (a) Dressed photon technology. (b) Bio & oxide electronics and photonics. (c) Crystal interfaces. (d) Photonics and related areas. (e) Spintronics and related areas. (f) Flexible photonics and electronics.

bers of their laboratories.

InCEPT promotes theoretical and experimental research from diverse viewpoints and approaches regarding various topics, such as materials, devices, fabrication, information processing, and biotechnology, in order to gain more profound and fundamental knowledge on the novel science and technology involving nanoscale electron-photon interactions. Furthermore, InCEPT is also committed to promoting international collaboration and providing value to society. Research activities of the core members are:

**[Dressed photon technology
(Director, Prof. M. Ohtsu)] (Fig. 1(a))**

- (1) Principles of dressed photons: light-matter interactions in nanometric space, photon-electron-phonon interactions
- (2) Applications of dressed-photon devices: novel functional nano-scale optical devices; nano-fabrication, including smoothing material surfaces; energy conversion, including silicon light emitting diodes and lasers; and information processing, including non-Von Neumann computing

**[Bio & oxide electronics and photonics
(Prof. H. Tabata)] (Fig. 1(b))**

- (1) Oxide spintronics
- (2) Oxide plasmonics
- (3) Ferrite engineering for solar energy harvesting systems
- (4) Terahertz spectroscopy and imaging for nano-bio sensing devices
- (5) The “Yuragi” system based on spin-glass and/or relaxor materials for brain mimetic devices

[Crystal interfaces (Prof. Y. Ikuhara)] (Fig. 1(c))

- (1) Electron microscopy
- (2) Interface and grain boundary structures

**[Photonics and related areas (Prof. K. Hotate)]
(Fig. 1(d))**

- (1) Optical sensing, optical information processing, optical communications and related areas

**[Spintronics and related areas (Prof. M. Tanaka)]
(Fig. 1(e))**

- (1) Spintronics, from synthesis of materials to development of devices

**[Flexible photonics and electronics (Prof. T. Someya)]
(Fig. 1(f))**

- (1) Organic electronic devices, such as organic thin-film transistors, organic photovoltaic cells, organic photode-

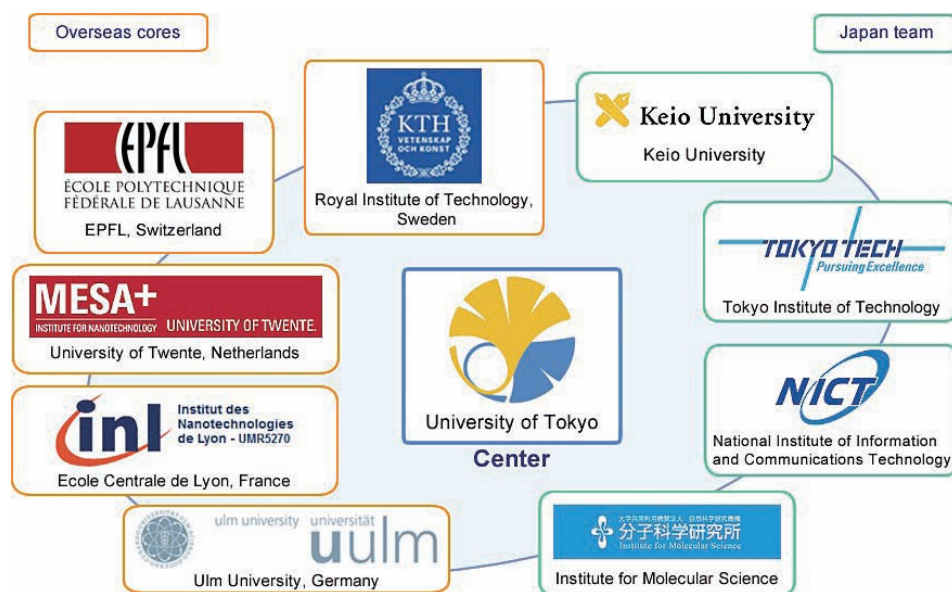


Fig. 2: Formation of the Core-to-Core Program entitled “Nanoscale electron photon interactions via energy dissipation and fluctuation.” (Program leader: Prof. H. Tabata).

tectors, organic light emitters, and their integration on plastic and elastomeric substrates in order to develop flexible photonic and electronic systems

ACADEMIA-INDUSTRY COLLABORATION

InCEPT has pursued collaborations between academia and industry. The science and technology of nanoscale electron-photon interactions have already impacted a number of practical technologies, such as metrology, devices, fabrication, information processing, and biotechnology, and are expected to open up a broad range of novel applications. More than 30 companies are involved.

INTERNATIONAL COLLABORATION

To promote international collaboration, the Core-to-Core Program of the Japan Society for the Promotion of Science (JSPS) entitled “Nanoscale electron photon interactions via energy dissipation and fluctuation” started in 2014. The mission of InCEPT is to support this program, as a secretariat to foster international collaborations. Prof. H. Tabata, a core member of InCEPT, serves as the leader of this program. Other members of InCEPT participate in this program, and active scientists from other universities and research institutes are also involved.

The aim of this program is the establishment and comprehensive operation of a global co-operative research hub that uses cutting-edge technology to enable energy savings using nano-electric photonics with a focus on dissipative yuragi (noise) as a new guiding-principle alternative to the scaling rule. By constructively utilizing yuragi, this program aims to develop an innovative technology for energy saving and to elucidate new fundamental concepts of nano-electronic photonics through active international collaboration with leading scientists from France, Germany, the Netherlands, Sweden, and Switzerland. Fig. 2 schematically explains the formation of this program.

This program is actively promoting international collaborations, organizing bilateral seminars, workshops, exchanges of scientists and students, and collaborative research projects, in order to globally expand the achievements of the science and technology of nanoscale electron-photon interactions, as well as pursuing other frontiers from a variety of diverse international views (Fig. 3).

Finally, regarding collaboration with countries in the Asia-Pacific region, InCEPT, and the NPC before it, have supported the organization of the Asia-Pacific Near-Field Optics Conference for the last two decades. The scope of this conference is to explore the potential for creating



Fig. 3: Scientific exchanges and workshops.

the new sciences and technologies of near-field optics, nano-optics, and nanophotonics. To provide opportunities for information exchange and interaction and to enable effective personal contact, the size of the conference was kept as compact as possible. This year, a memorable 10th annual conference was held in Hakodate, Japan. 138 presentations were given by researchers from Australia, Belgium, China, India, Japan, Korea, Singapore, Sweden, Taiwan, Thailand, and the USA (Fig. 4).

Acknowledgements: The author is deeply grateful to Prof. H. Tabata and Prof. T. Yatsui for their help in preparing the manuscript of this article.

References

- [1] M. Ohsu (ed.), *Progress in Nano-Electro-Optics V*, Springer, Berlin, pp. VII-VIII (2006).

FURTHER READING

InCEPT: <http://www.incept.t.u-tokyo.ac.jp>

Dressed photon technology: <http://uuu.t.u-tokyo.ac.jp/>

Bio & oxide electronics and photonics: <http://www.bioxide.t.u-tokyo.ac.jp/>



Fig. 4: Group photograph taken at the 10th Asia-Pacific Near-Field Optics Conference, held in Hakodate, Japan (July 2015).

Crystal interface: <http://interface.t.u-tokyo.ac.jp/english/>
Photonics and related areas: <http://www.sagnac.t.u-tokyo.ac.jp>

Spintronics and related areas: <http://www.cryst.t.u-tokyo.ac.jp/>

Flexible photonics and electronics: <http://www.ntech.t.u-tokyo.ac.jp/>

Our Core-to-Core Program: <http://www.bioxide.t.u-tokyo.ac.jp/core>

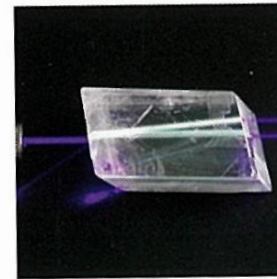
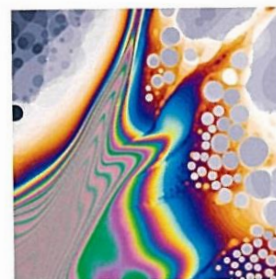
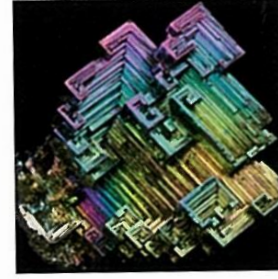
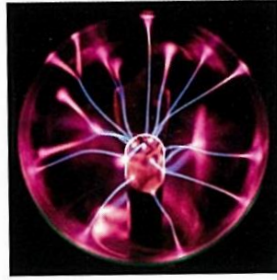
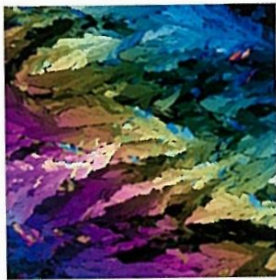


Motoichi Ohtsu is currently a director of InCEPT and a professor of the Department of Electrical Engineering and Information Systems at the Graduate School of Engineering of the University of Tokyo. He received a doctorate degree in electronics engineering from the Tokyo Institute of Technology, Tokyo in 1978. He was appointed as a research associate, an associate professor, and as a professor at the Tokyo Institute of Technology. From 1986 to 1987, while on leave from the Tokyo Institute of Technology, he joined the Crawford Hill Laboratory, AT&T Bell Laboratories, in Holmdel, NJ. In 2004, he moved to the University of Tokyo as a professor. His main research activities have been in near-field optics, nanophotonics, and dressed-photon technology.

[IV] PUBLISHED BOOKS



イラストレイテッド
光の実験
大津元一[監修] 田所利康[著]



朝倉書店

目次

1 「光」の撮影を楽しもう	2
1.1 マニュアル撮影のすすめ	2
1.2 絞り, シャッター速度, ISO 感度の関係	5
1.3 微弱光撮影ならではの注意点	7
2 見える「光」を楽しもう	8
2.1 散乱で光線を可視化する	8
2.2 蛍光で光線を可視化する	12
2.3 LED ライン光源を使って光線を可視化する	18
3 色の変化を楽しもう	20
3.1 鉱物の美しい蛍光色	20
3.2 偏光がなければ見えない色彩	28
3.3 砂糖水をカラフルにする	34
4 光の不思議を楽しもう	42
4.1 虹の出射を再現する	42
4.2 逃げ水を撮影しよう	44
4.3 曲がる光	48
4.4 水で光ファイバーを作る	51
5 スペクトルを楽しもう	54
5.1 光を分ける	54
5.2 分光器	55
5.3 CD-R 分光器でスペクトル像を撮影する	56
5.4 プラズマボールの色の謎を探る	62
5.5 プリズムが作るスペクトル	65
5.6 温度で変わるスペクトルと色	68
6 色彩を楽しもう	74
6.1 微細構造が「色」を作り出す	74
6.2 干渉から生まれる色彩	75
6.3 イリスアゲートの怪しい輝き	80
6.4 コガネムシの円偏光選択反射	84
7 ミクロを楽しもう	86
7.1 顕微鏡の像拡大	86
7.2 照明方法による見え方の違い	87
7.3 1層ずつ割れるシャボン膜	90
7.4 色彩あふれるミクロの世界	92
8 物作りを楽しもう	98
8.1 LED ライン光源を作る	98
8.2 CD-R 分光器を作る	103
8.3 二重スリットカメラを作る	110

Motoichi Ohtsu

Silicon Light-Emitting Diodes and Lasers

Photon Breeding Devices using
Dressed Photons

 Springer

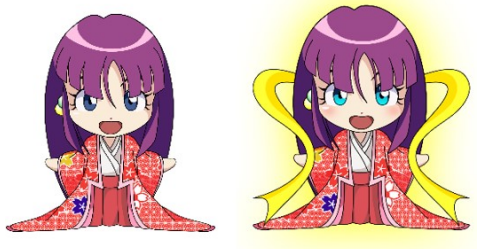
Contents

1 Problems with Light Emitting Devices and Their Solutions	1
1.1 Introduction	1
1.2 Dressed Photons and Dressed-Photon–Phonons	2
1.3 Principles of Photon Emission.	6
1.3.1 Single-Step De-Excitation.	6
1.3.2 Two-Step De-Excitation.	7
1.4 Photon Breeding	8
1.5 Fabrication and Performance of Photon Breeding Devices	10
1.5.1 Fabrication.	10
1.5.2 Spatial Distribution of the Dopant Atoms.	11
1.5.3 Performance.	11
1.5.4 Family of Photon Breeding Devices	12
References	12
2 Visible Light Emitting Diodes Using Silicon Crystal	15
2.1 Introduction	15
2.2 Device Fabrication.	16
2.3 Device Operation.	19
2.4 Increasing the Light Extraction Efficiency.	22
References	27
3 Infrared Light Emitting Diodes Using Silicon Crystal	29
3.1 Device Fabrication.	29
3.2 Device Operation.	31
3.3 Spatial Distribution of Boron	35
3.4 Polarization Control.	39
References	42

4 Contribution and Control of Coherent Phonons	43
4.1 Strength of Phonon Coupling	43
4.2 Contribution of the Multimode Coherent Phonons	47
4.3 Control of Light Emission Spectral Profile	51
4.3.1 Principle of Control	51
4.3.2 Evaluation of Light Emission Spectrum	56
4.3.3 Control of Spatial Distribution of Boron	61
References	62
5 Infrared Lasers Using Silicon Crystal	65
5.1 Basic Devices	65
5.2 Decreasing the Threshold Current Density	70
5.3 Evaluation of Optical Amplification Quantities	74
5.4 Novel Devices with High Output Optical Power	77
References	81
6 Light Emitting Diodes Using Silicon Carbide Crystal	83
6.1 Basic Light Emitting Diodes	83
6.2 Green Light Emitting Diodes	87
6.3 Ultraviolet Light Emitting Diodes	91
6.4 Broad-Spectral-Width Light Emitting Diodes	97
References	101
7 Light Emitting Diodes Fabricated Using Other Crystals	103
7.1 Using a Gallium Phosphor Crystal	103
7.1.1 Fabrication and Operation	104
7.1.2 Changing the Barrier Height with an Applied External Field	108
7.1.3 Optimum Condition for DPP-Assisted Annealing	111
7.2 Using a Zinc Oxide Crystal	113
References	118
8 Other Devices	121
8.1 Optical and Electrical Relaxation Oscillator	121
8.2 Infrared Photodetector with Optical Amplification	126
8.3 Polarization Rotator	132
8.3.1 Devices Using ZnO Crystal	132
8.3.2 Devices Using SiC Crystal	135
References	137
Appendix A: Physical Picture of Dressed Photons	139
Appendix B: Range of Interaction Mediated by Dressed Photons	147
Appendix C: Coupling Dressed Photons and Phonons	163

Appendix D: Photon Absorption and Emission Via Dressed Photon–Phonons	179
Appendix E: Two-Level System Model	183
Index	187

[VI] APPENDIX



**03: High-power current-injection
type Silicon laser using
nanophotonics**

Tadashi Kawazoe^{1,2}, Kazunobu
Hasimoto^{1,2}, Satoshi Sugiura^{1,2}

¹*Department of Electrical Engineering and Information Systems, Graduate School of Engineering, The University of Tokyo, Bunkyo-ku, Tokyo, Japan*

²*Specified Nonprofit Corporation Nanophotonics Engineering Organization, Tokyo, Japan*

Email: kawazoe@npeo.or.jp,

We have demonstrated several near-infrared Silicon (Si) laser devices at room temperature fabricated using a phonon-assisted process [1-3]. Their operation principle and fabrication method are based on the photon-phonon interaction via dressed photons [4,5]. The optical properties of the fabricated Si laser medium showed a low optical gain and a small absorption coefficient [3]. These features come from the Si which is the indirect transition type semiconductor. So, the optical properties of Si laser medium are much different from those of the conventional semiconductor laser medium with a high gain and a large absorption coefficient. Therefore, a new design as a semiconductor laser is necessary for the Si laser.

In this presentation, we demonstrate current injection type Si laser with a unique design. Its lasing threshold current density decreased to $60\text{A}/\text{cm}^2$ and the output power of the laser increased to 13W at the wavelength of $1.34\mu\text{m}$ for the current density of $100\text{A}/\text{cm}^2$. The obtained threshold

current density is very low comparing with the conventional semiconductor lasers and the output power was more than 10^5 times larger than previous Si lasers that we fabricated.

Figure 1(a) shows the photograph of the front view of the Si laser device in operation taken by the infrared camera. Figure 1(b) shows a injection current dependence of the laser output power. The lasing spectral line width was more than 100 nm, because the device was a multimode broad area laser. The external power efficiency was about 20 %, and the external quantum efficiency was 80 %. We consider the high quantum efficiency comes from the multi-step transition via dressed-photon state.

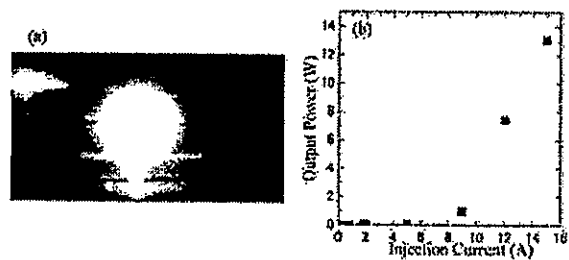


Fig1. (a) infrared photograph of the operating Si laser. (b) The injection current dependence of the laser output power

1. T. Kawazoe, M. Ohtsu, K. Akahane, and N. Yamamoto, *Appl. Phys. B* **107**, 659 (2012).
2. H. Tanaka, T. Kawazoe, M. Ohtsu, K. Akahane, and N. Yamamoto, *Appl. Phys. A* **121**, 1377 (2015).

3. H. Tanaka, T. Kawazoe, M. Ohtsu, and K. Akahane, *Fluoresc. Mater.* **1**, 1 (2015).
4. T. Kawazoe, M.A. Mueed, and M. Ohtsu, *Appl. Phys. B* **104**, 747 (2011).
5. T. Kawazoe, and M. Ohtsu, *Appl. Phys. A* **115**, 127 (2014).

ドレスト光子発光デバイス

特定非営利活動法人ナノフォトニクス工学推進機構
川添 忠

1 はじめに (ドレスト光子と発光デバイス)

ドレスト光子とは伝搬光が微小粒子等に照射されることでその表面近傍に局在した電磁場を量子化したものである。つまり、ドレスト光子には伝搬光の存在が必要不可欠になっている。伝搬光を必要としないドレスト光子はあるだろうか。答えは「Yes」である。Si (シリコン) など間接遷移型半導体のpn接合構造に順方向に電流を注入した場合が例として挙げられる。この時pn接合部には外部より注入された電子と正孔の対が形成される。そして間接遷移型半導体であるため伝搬光 (通常の光子) が発生するための条件の一つである波数保存則を満たさないため、光子が発生せず非輻射緩和が起こり、電子正孔対は再結合消滅する。この過程において、電子正孔対の周囲にはその電荷の大きさとエネルギーに見合った振動電磁場が形成されているが、伝搬光は発生しない。このような非輻射状態の電磁場でもその電場の2乗と磁場の2乗の和で与えられるエネルギーを持つ。すなわち、なんらかの量子で記述することか可能である。この量子こそが電子系と結びついた非伝播の光子であるドレスト光子である。

本稿ではpn接合構造をもつ間接遷移型半導体を用いた新しい光源 (発光ダイオード (LED) やレーザーダイオード (LD)) を紹介する。その動作は電流注入により発生したドレスト光子を効率よくフォノン散乱させることで光子 (伝搬光) に変換するという新しい原理に基づ

いている。

2 間接遷移型半導体LEDの発光原理と作製法

これまで幾つかの間接遷移型半導体を用いたLEDやLDを報告している¹⁻⁶⁾。その発光過程は通常の直接遷移過程とは異なり、ドレスト光子フォノンと呼ばれる中間状態を介して起こる。また、アトムプローブ法によるドーパント分布の解析から、その詳細が明らかになっている⁷⁾。

2.1 間接遷移型半導体LEDの発光原理

図1にSiのバンド構造を示す。伝導帯の底はX点近傍にあり、価電子帯の頂上は Γ 点にある。伝導帯の底と価電子帯の頂上にある電子正孔対が光放射を伴って発光する場合、 $k=\Gamma-X=\pi/a\{100\}$ (a はSiの格子定数、 $\{100\}$ は方位) に相当する波数がフォノンの散乱などによって電子正孔対に供給される必要がある。図中には、波数 $k=\pi/3 a\{100\}$ のフォノンを3個放出して電子正孔対が再結合発光する過程を記述してある。前述したように間接遷移型半導体中の電子正孔対は放出できない光子すなわちドレスト光子をまとっている。加えて、この遷移過程にはフォノンによる散乱も必要である。言い換えるとドレスト光子フォノンと呼ばれる3つの状態 (光子・電子正孔対・フォノン) が混ざり合った状態であれば、光子の放出が可能である。すなわち、図1で示したようなドレスト光子フォノンを高い確率で生じるような構造を作

板と呼ぶ。このデバイスを透過させることにより、直線偏光の振動面の角度を90度変化させたり、円偏光の回転方向を変えたりすることができる。1/4波長板と同様、直線偏光を入射させる場合は、光学軸に対して45度ずらさなければならない。また、1/4波長板を2枚重ねると1/2波長板にすることができるが、この時も2枚の1/4波長板の光学軸を揃えなければならない。例えば、それらの光学軸を直交させて重ねると、変化した光の位相が元に戻ってしまい、何もしないことと同じになる。

3.3 旋光子

図6.26のように、直線偏光の方向を回転させるデバイスを旋光子と呼ぶ。ファラデー回転子と呼ばれる、磁気光学効果を用いたものがある。磁気光学効果は、元々、フリントガラスでその現象が発見されたように、珍しい現象ではないが、実際の素子では、ガーネットのように、その効果が大きい材料が用いられている。

1/2波長板も一種の旋光子であるが、ファラデー回転子では、素子の長さLと磁場の強さHによって、回転する角度 α を自由に制御することができる。物質の種類、光の波長、温度に依存するベルデ定数をVとすると、この角度は、次式で表される。

$$\alpha = VHL \quad (6.14)$$

ファラデー回転子を2枚の偏光子でサンドイッチしたデバイスを光アイソレータと呼ぶ。図6.27において、左側から入射した光は、偏光子に入射して図の縦方向に振動する直線偏光となる。次にファラデー回転子に入射すると、ここで、偏光の方向が45度回転する。2枚目の偏光子は、回転した直線偏光がそのまま透過するように配置されている。一方、図の右側から入射した光は、右側の偏光子によって45度回転した直線偏光となる。この光がファラデー回転子に入射すると、振動方向がさらに45度変化し、左側の偏光子を透過できなくなる。したがって、電気アイソレータと同様に、信号が一方通行のデバイスとなることから、光アイソレータと呼ばれている。半導体レーザーは、外から光が入射すると状態が不安定になることから、光アイソレータの左側に半導体レーザーを置き、外からの光が入らないような用途に使われている。

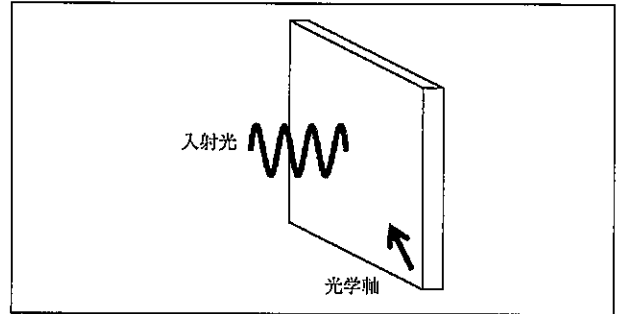


図6.25 1/4波長板

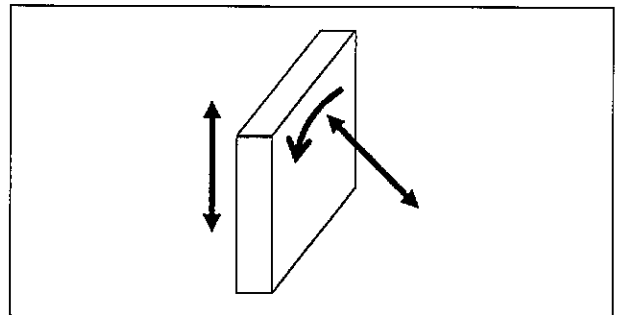


図6.26 ファラデー回転子

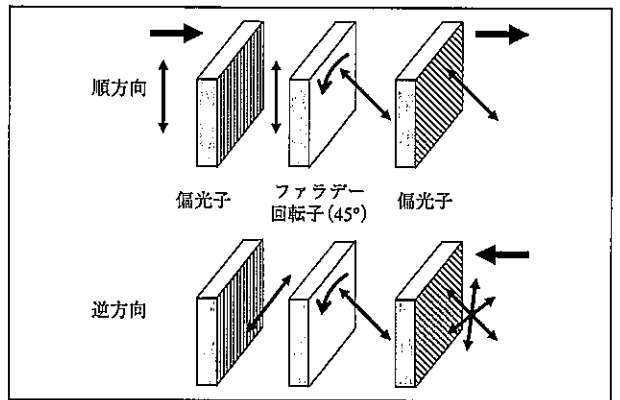


図6.27 光アイソレータ

OPTO.TV (<http://opto.tv/>) では、「ひかり発見」の連載に合わせて実験の様子をビデオ撮影し、その内容を動画で解説したシリーズを連載しています。本連載と合わせてご覧ください。

- Optics Discovery
- Shigeru Kawai
- Opto-eCollege Corporation

カワイ シゲル
所属：(株)オプト・イーカレッジ 代表取締役

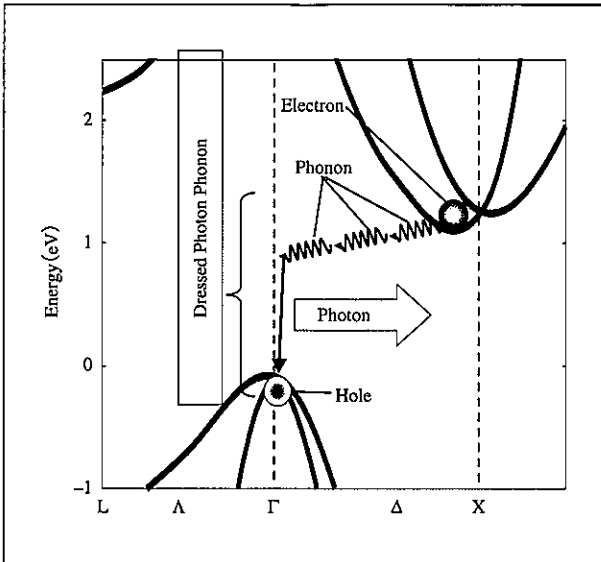


図1 Siのバンド構造

り出せば、たとえSiのような間節遷移型半導体であっても効率よく発光するのである。

次にドレスト光子フォノンを効率よく発生するするために必要なSi-pn接合部の結晶状態について説明する。Si結晶にはp、n型化するためにドーパントが $10^{15}\sim 10^{19}/\text{cm}^3$ ほどの密度で導入されている。p型ドーパント種としてボロン(B)やn型ドーパント種として砒素(As)、アンチモン(Sb)を使った場合、原子の質量がSiと大きく異なるので(Bは軽く、AsやSbは重い)、これらの原子は格子振動であるフォノン閉じ込めのための反射境界として働くのである。図1の発光過程が起こるためのフォノン閉じ込めの様子を図2(a)に示す。Si結晶はダイヤモンド構造を持つ多重立方格子なので、ドーパント原子を持つ単位胞を黒丸でドーパント原子を持たない単位胞を白丸で記述し、2つの隣接するドーパント原子に閉じ込められたフォノンの様子を記述してある。ドーパント原子がSi原子より重い場合、固定端反射によるフォノン閉じ込めになり、ドーパント原子が軽い場合は開放端反射によるフォノン閉じ込めになる。いずれの場合も閉じ込められるフォノンの半波長がドーパント間距離と一致する。パネモデルを用いた計算によると孤立した1つのドーパントの場合と比較してドーパント対におけるフォノンの振幅は2桁以上大きくなる⁹⁾。この結果、ドーパント

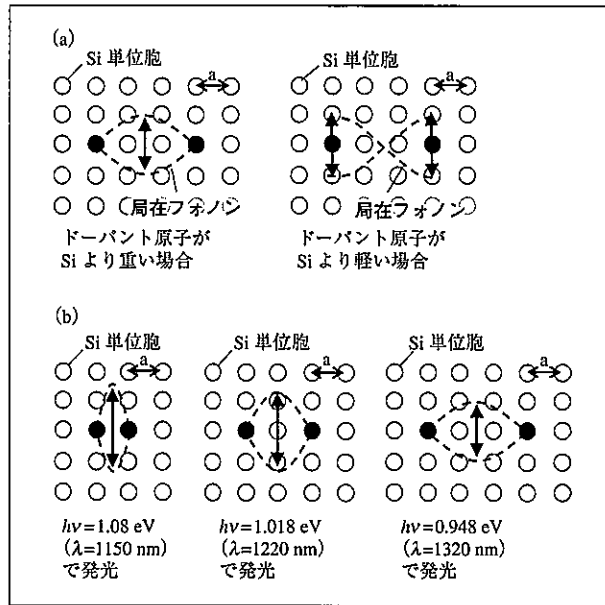


図2 ドーパント対に閉じ込められたフォノン

ト対によってドレスト光子フォノンの生成確率は4桁以上大きくなるのである。これは発光確率が4桁以上大きくなることを意味する。また、閉じ込められるフォノンの波数により、発光波長が変化する(図2(b)参照)。最隣接ドーパントが隣の格子にある場合、閉じ込められるフォノンの波数は $k=\pi/a\{100\}$ となり、1個のフォノンでX点近傍の電子はΓ点まで散乱され再結合発光が起きる。Si中のフォノンの分散曲線から、波数 $k=\pi/a\{100\}$ のフォノンのエネルギーは0.06 eVであるので、バンドギャップエネルギー $E_g(1.14\text{ eV})-0.06\text{ eV}=1.08\text{ eV}$ (波長 $\lambda=1150\text{ nm}$)のエネルギーを持つ光子が放出される。以下同様に最隣接ドーパントが $2a$ の距離の位置にある場合は波数 $k=\pi/2 a\{100\}$ を持つ閉じ込めフォノンが最低次モードになり、2個のフォノンが必要になるので、 $E_g(1.14\text{ eV})-2\times 0.061\text{ eV}=1.018\text{ eV}$ ($\lambda=1220\text{ nm}$)のエネルギーの光子が放出される。そして図1に示した過程、すなわち波数 $k=\pi/3 a\{100\}$ のフォノン3個による発光過程是最隣接ドーパントが $3a$ の距離の位置にある場合に起こり、放出される光子エネルギーは $E_g(1.14\text{ eV})-3\times 0.064\text{ eV}=0.948\text{ eV}$ ($\lambda=1320\text{ nm}$)になる。ここで用いたフォノンのエネルギーはSi中の光学フォノンの分散に従って、その波数に対応した値を使っている事に注意して欲し

い。なお、最低次のモードのみを考慮している理由は光とフォノンの結合の大きさはラマン散乱に見られるように波数の小さい（モード次数の小さい）フォノンがより強い光学応答性を持つからである。

2.2 間接遷移型半導体LEDの作製

最隣接ドーパント間の位置関係を決定できれば自由に発光波長が選べるSi-LEDを作製することが可能である。しかしながら、ドーパント位置を正確に並べる事は通常は困難であり、ドレスト光子援用（DPP）アニール法が必要である。DPPアニール法は間接遷移型半導体では電子が反転分布になりやすいことを利用し、発光させたい波長を持つ光源の光をpn接合部に照射しつつ、順方向電流を印加することで生じるジュール発熱で素子アニールを行う方法である。順方向電流による発熱でドーパントは熱拡散し移動する。拡散移動の途中で照射している光源の波長に対しドレスト光子フォノンを通じて誘導放出が起こりやすい、すなわちフォノン放出が起こりやすいドーパント対の配置になると、図1の様な発光過程を経て誘導放出が起こり、光としてエネルギーを放出し、ドーパント対周辺の温度が下がる。この結果、拡散が停止し、ドーパント対の位置関係が固定される。誘導放出と自然放出の確率は比例関係にあるため、ドレスト光子援用アニールされた素子は自然放出確率も大きくなっており、間接遷移型半導体でありながらLEDとして機能する素子が完成する。

図3に波長1320 nmのレーザーを照射しながら順方向電流を印加するドレスト光子援用アニールを行って作製したLED素子のEL発光スペクトルを示す。図3に (a), (b), (c), (d) はそれぞれDPPアニール前、1分後、7分後、30分後の素子のELスペクトルである。図3 (d) に示すように30分間のDPPアニールによって、アニール光源波長である1320 nm ($h\nu=0.948$ eV) ~ 1600 nmに複数の発光ピークを持つSi-LEDが完成する。

2.1節で述べた発光機構とドーパント原子の配置の関係を調べるため、DPPアニール前、後のドーパントの空間分布をアトムプローブ法によって計測した。この方法により図4 (a) に示すように各ドーパント原子の3次元位置座標が0.1~0.2 nmの分解能で明らかになる。アト

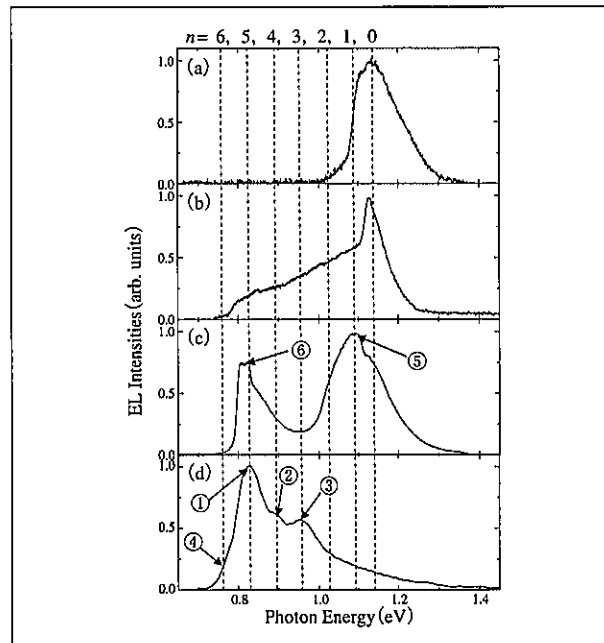


図3 Si-LEDの発光スペクトル

ムプローブ法による結果からランダムに分布しているドーパントはDPPアニールにより拡散移動しても、その空間濃度分布には変化が生じなかった。しかし、2つの最隣接ドーパントの位置関係を調査するとDPPアニールによってドーパント原子の配置に規則性が現れることが分かった。図4 (b) にDPPアニール前と後の最隣接ドーパント間距離の分布を示す。図中の実線は無秩序にドーパントが分布したときの場合を示しており、ワイブル分布と呼ばれる。この結果によると最隣接ドーパント間距離は格子定数aの整数倍の位置に配置しやすいということが分かった。すなわち、最隣接ドーパントは斜めの方向例えば {110} や {111} 方向には並ばずにSiの格子定数aが定義される方向 {100} にそって並ぶのである。この方向に並んだ最隣接ドーパント対に閉じ込められるフォノンの波数は $k=\pi/n \cdot a\{100\}$ となり、その波数ベクトルは2-1節で説明した発光機構に必要なフォノンとまさに一致する。

この実験に用いた素子ではそのドーパント濃度のため、格子定数の5倍 ($n=5$) の位置に並んだドーパント対が最も多く見られた。このドーパント対に閉じ込められたフォノンによって散乱放出される光子のエネルギー

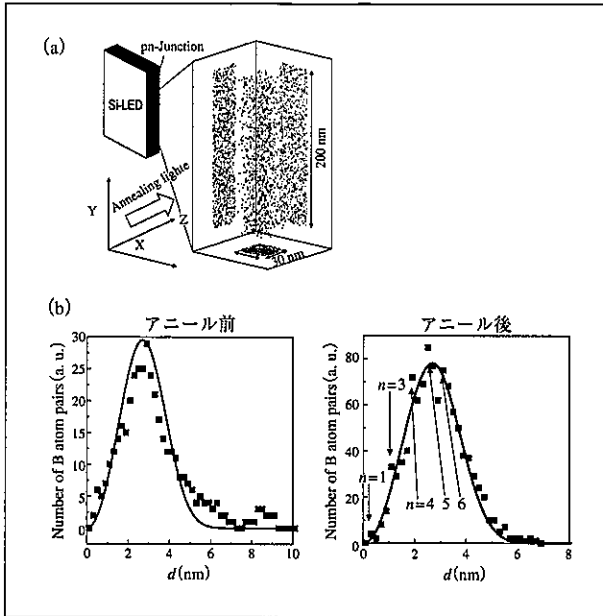


図4 アトムプローブ法により計測されたドーパント分布と最隣接ドーパント距離の分布

は $E_g(1.14 \text{ eV}) - 5 \times 0.065 \text{ eV} = 0.815 \text{ eV} (\lambda = 1520 \text{ nm})$ であり、図3 (d) の発光ピーク的光子エネルギーと一致する (図中①)。同様に格子定数の4倍 ($n=4$) の位置に並んだドーパント対を起源とする発光も見えている (図中②)。ワイブル分布からのズレの比率は格子定数の3倍 ($n=3$) の位置に並んだドーパント対が最も大きかった。これはDPPアニールの際に用いた光源が1320 nmであり、フォノン3個が必要な光子放出過程で起こる発光波長と一致している (図中③)。一方、格子定数の6倍の位置に並んだドーパント対の発光に関しては発光波長が計測装置の計測可能範囲外になっているが、僅かに肩が見えている (図中④)。格子定数の2倍 ($n=2$) の位置に並ぶドーパント対はアトムプローブ法ではほとんど無かった。これに対応してEL発光スペクトルにも格子定数の2倍の位置に並んだドーパント対からの明瞭な発光ピークは計測されていない。

DPPアニールの進行により変化するEL発光スペクトルを使ってドーパント配列の変化により説明する。①アニール前は特定のフォノンが多いわけではないので、僅かに起こるバンド間遷移の発光が計測されている (図4 (a))。②次にドーパントの配列が進むに従い広い

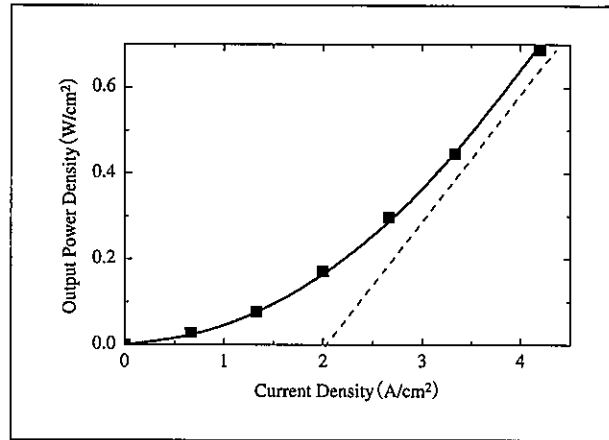


図5 作製したSi-LEDの光出力の電流密度依存性

範囲で発光が起こり始める (図4 (b))。ただし、まだ、特定の波数のフォノンが強くないのでフォノン散乱による明瞭な発光ピークは現れていない。③ドーパント対の間隔よりも先に配列方位が定まり、1個のフォノン散乱で良いので高い頻度で起こる $n=1$ の発光 (図中⑤) とドーパント密度のため、最もドーパント対の数が増える $n=5$ に相当する発光ピーク (図中⑥) が支配的になる。④最期にドーパント間隔がそろい始め、 $n=3$ の位置に明確なEL発光ピークが出現するのである。

図5に作製されたSi-LEDの電流に対するEL発光強度依存性を示す。近赤外域 ($0.73 \text{ eV} < h\nu < 1.5 \text{ eV}$) の発光強度は注入電流の2乗に比例し、外部微分子量子効率40%に達する。2乗に比例するのは発光のための散乱体であるドーパント対の位置に電子と正孔が同時に入る確率が注入電流密度の2乗に比例するからである。

3 DPPアニールを用いたその他の発光素子

Si-LEDの特性を発展させた素子としてSi-レーザーの発振にも成功している。100 mW - 1 W級のレーザーとして作製された波長1.3 μm 帯Si-レーザーの電流-光出力特性を図6示す。図6の挿入図は20 cmの距離に置いた投影板に出力光を照射し、赤外線カメラで撮影したものである。レーザー光の可干渉性から、スペックルと呼ばれる斑点模様が現れている。また、発振波長がSiの透明帯であるため閾値電流密度が小さく、15 A/cm^2 であった。

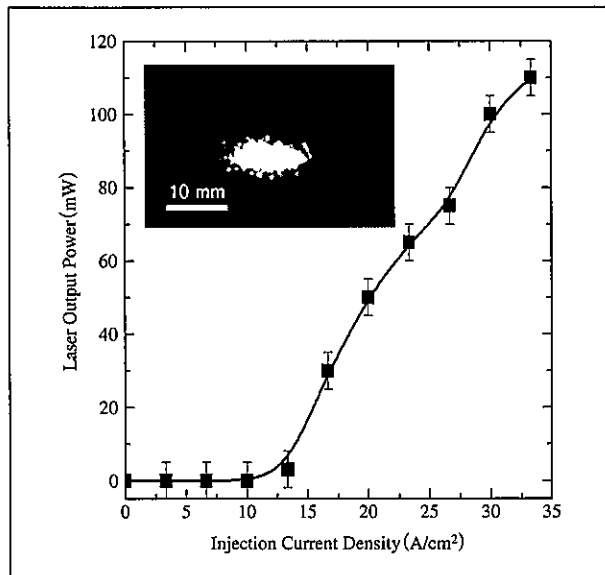


図6 Si-Laserの出力光の空間パターンと出力光強度の注入電流密度依存性

DPPアニーリング法による間接遷移型半導体LEDはSi以外にもSiC、GaP⁹⁾などを用いても実現されている。また、この方法は発光波長を材料組成ではなくDPPアニーリングの際用いる光源の波長で制御可能であるという特徴有する。最近では発光波長のみならず、偏光も制御が可能となりつつある。

4 最期に

本稿ではドレスト光子を利用した関節遷移型半導体によるEL発光デバイスについて紹介した。特に発光機構に関して従来の方法と全く異なるため紙面を多く割いた。ドーパント対の配列方位と間隔が発光機構と密接に関係しており、この関係を利用した偏光LEDや最期に紹介したSi-LED、Si-レーザー、SiC-LED等に関しては参考文献を参照していただきたい。

参考文献

- 1) T. Kawazoe, M. A. Mueed, M. Ohtsu, *Appl. Phys. B* **104**, 747 (2011).
- 2) M. A. Tran, T. Kawazoe, M. Ohtsu, *Appl. Phys. A* **115**, 105 (2014).
- 3) T. Kawazoe, M. Ohtsu, K. Akahane, N. Yamamoto, *Appl. Phys. B* **107**, 659 (2012).
- 4) H. Tanaka, T. Kawazoe, M. Ohtsu, K. Akahane, *Fluoresc. Mater.* **1**, 1 (2015).
- 5) H. Tanaka, T. Kawazoe, M. Ohtsu, *Appl. Phys. B* **108**, 51 (2012).
- 6) T. Kawazoe, M. Ohtsu, *Appl. Phys. A* **115**, 127 (2014).
- 7) T. Kawazoe, K. Nishioka, M. Ohtsu, *Appl. Phys. A* **121**, 1409 (2015).
- 8) Y. Tanaka, K. Kobayashi, *Phys. E* **40**, 297 (2007).
- 9) JH Kim, T. Kawazoe, M. Ohtsu, *Appl. Phys. A* **121**, 1395 (2015).

■ Light emitting devices using dressed photon

■ Tadashi Kawazoe

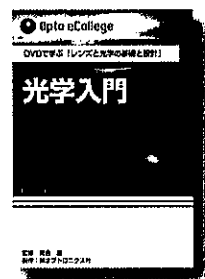
■ Specified Nonprofit Corporation Nanophotonics Engineering Organization

カワゾエ タダシ

所属：特定非営利活動法人 ナノフォトンクス工学推進機構

Opto eCollege

図と文字とナレーションで「分かりやすく」かつ「楽しく」学習



DVDで学ぶレンズと光学の基礎と設計

1. 光学入門 3枚組(8時間40分) 定価：20,000円+税

- ・光の基礎
- ・幾何光学の基礎
- ・マイクロレンズ
- ・波動光学の基礎
- ・光波伝搬の基礎
- ・光学機器の基礎
- ・光学設計の基礎

※本商品は直販限定です。
一般の書店などではお取り扱いできません。